



Investigation on gravitational star-disk encounters producing ‘Oumuamua and Borisov-like Interstellar Objects

Masterarbeit in Astrophysik

von
Luis Lauro Aizpuru Vargas

angefertigt am

Jülich Supercomputing Center im Forschungszentrum Jülich GmbH

vorgelegt der

Mathematisch-Naturwissenschaftlichen Fakultät

der

Rheinische Friedrich-Wilhelms-Universität Bonn

August 2020

Matrikel Nr. 3114258

Supervisors

Gutachterin 1: Prof.Dr.Susanne Pfalzner

Gutachter 2: Prof.Dr.Pavel Kroupa

Declaration of Authorship

I, Luis Lauro Aizpuru Vargas, hereby declare that this thesis titled, “Investigation on gravitational star-disk encounters producing ‘Oumuamua and Borisov-like Interstellar Objects” was formulated by myself and the work presented in it is my own. I confirm that:

- This work was done while in candidature for a Masters degree at the University of Bonn.
- Where I have consulted the published work of others, this is always clearly attributed.
- Where I have quoted from the work of others, the source is always given. With the exception of such quotations, this thesis is entirely my own work.
- I have acknowledged all main sources of help.

Signed: _____

Date: _____

Acknowledgements

The past two and a half years have been both an intellectual and a personal challenge. I have certainly been pushed to my limits, and as a result I have grown as an individual. The knowledge, lessons and friendships that I have cultivated during my time in Bonn will stay with me forever.

First and foremost, I would like to express my gratitude to my supervisor Prof.Dr.Susanne Pfalzner. Her patience and guidance throughout my thesis work has been paramount for its development and completion. The lessons, scientific and otherwise, that I have learned throughout the past 12 months have had an enormous impact on me. I am sure that I will be able to apply them in whichever career path I pursue in the future. Moreover, I would like to especially thank Prof.Dr.Susanne Pfalzner and Forschungszentrum Jülich for providing me with a very generous stipend for the past year. The current economical circumstances due to the pandemic have not been easy for many people. Having a stable source of income allowed me to have the peace of mind to fully concentrate on my studies. Furthermore, I would also like to thank my secondary supervisor Prof.Dr.Pavel Kroupa. His punctual feedback on my work enriched the final version of this thesis. In case he reads this, I would like to tell him that he was the professor that had the most impact on me during my Masters. His courage and defiant spirit against the status quo is remarkable. The world needs more brave people that are able to think outside the box and defend their beliefs even if they are alone in doing so. I will certainly look up to these ideals, both in my personal and professional life.

I would also like to thank Asmita Bhandare for her always courteous and helpful advice. Her guidance during the initial phases of my thesis was essential. In particular, in the initial numerical setup for this project. Her continuous advice whenever I had questions regarding any computational roadblocks was greatly appreciated. Also, I want to thank my group colleague Amith Govind for the discussions we had regarding science, politics and life. The environment of respect and camaraderie we created made this whole process more enjoyable. I would like to extend my gratitude to both Annika Hagemeier from Forschungszentrum Jülich and Dirk Müders from MPIfR for their scientific and technical support.

I would like to extend my appreciation to all the friends I made while living here in Bonn. I was so fortunate to meet people from all the corners of the world. It was truly an international experience! This list is by no means exhaustive but here are some people I would like to personally thank: Çağrı Erciyes, Melih Kara, Ji Woong Jang, Evgenii Chaikin, Heba Elkilany, Lavanya Nemani, Nyan Nguyen, Ashly Sebastine, Annabel Rolofs and Marielle Adams.

Finally, I would like to thank my parents and brother for their unconditional love and support. All of this would have been impossible without you.

Abstract

The recent discovery of two Inter-Stellar Objects (ISO) in our own Solar System has prompted astronomers to come up with theoretical explanations on how they are produced. Most newly formed stars are initially surrounded by a protoplanetary disk. The main hypothesis is that these ISOs were planetesimals in such disks and that through one mechanism or another became unbounded from their host stellar system. These same stars and their disks are preferentially formed in stellar clusters. The gravitational effects that result from the interaction between disks and stars are thus common and relevant for the understanding of the fate of such disks. Amongst these mechanisms there is the gravitational stellar fly-by encounter. The partial destruction of the disk by the perturber star produces a varying number of unbounded planetesimals. Several studies have looked into the effects of stellar fly-bys on disks both for the co-planar prograde case and for inclined retrograde cases. They investigated properties such as final disk size or final fate of the test particles. However, the particles that become unbound have attracted little attention so far. This work focuses on the particles that become unbound during such fly-bys, contributing to the ISO population. We perform numerical simulations of a range of parabolic inclined encounters with varying perturber star masses and periastron distances for the encounters. The parameter space explored in this work is relevant for a typical young open stellar cluster environment. Here we focus on the relative amount and the velocities of ISOs produced during such fly-bys. We found that the velocity distribution of unbounded test particles varies according to the different possible combination of parameters. Nonetheless, the final ejection velocities were found to be in the range between 0.3 km/s and 3.0 km/s. Using the results of this particular work along with the available literature on the velocities of ISOs produced by other sources, we can make a quantitative distinction between the different types of ISOs. As a follow up study, more precise cluster simulations accounting for the IMF function, binary populations and viscous disks would provide a more realistic and comprehensive study of the production of ISOs in clusters.

Contents

1 Overview and Background	11
1.1 Origin of ISO	11
1.2 Protoplanetary Disk Physics	14
1.3 Cluster Environments	18
1.4 Stellar Encounters	22
1.5 Aim and Motivation	28
2 Method	29
2.1 Numerical Method for Gravitational Stellar Encounters	30
2.2 Initial Conditions	32
2.3 Dynamics	32
2.4 Diagnostics	33
3 Results	35
3.1 Varying Mass and Periastron Distance	36
3.2 Varying Inclination	48
4 Discussion	53
4.1 Limitations of our Model	53
4.2 Comparison with Previous Work	54
5 Summary and Conclusions	58
6 Appendices	60
6.1 Numerical Tables	60
6.2 Complementary Figures	62
7 Bibliography	82

List of Figures

Fig.1 Schematic Structure of an AGB star.....	12
Fig.2 Relative Velocities of Planetesimals for Distinct Chemical Processes to Occur.....	13
Fig.3 Potential formation Scenarios for Interstellar Objects.....	14
Fig.4 Hierarchical Collapse Model.....	15
Fig.5 Herbig Haro Object.....	16
Fig.6 Delta variance of a Self-Gravitating Cloud.....	17
Fig.7 IMF Functions.....	19
Fig.8 Gas Density Simulation for distinct Mean Number Densities	21
Fig.9 Summary of Dynamical Encounters in Clusters.....	24
Fig.10 Particles Mapped to Initial Disk Location for Different Properties.....	25
Fig.11 Sketch of Disk and Pertuber Star Orbit.....	26
Fig.12 Disk Size Schematic Determination.....	27
Fig.13 Final Disk Sizes as a Function of Inclination.....	28
Fig.14 Visualization of Star-Disk Interactions.....	31
Fig.15 DESTINY database structure tree.....	34
Fig.16 Fly-By visualization as a Function of Time.....	35
Fig.17 Percentage of Test Particles by Type for Different Periastron Distances M=1	37
Fig.18 Percentage of Test Particles by Type for Different Periastron Distances M=10	38
Fig.19 Percentage of Unbounded Particles vs Periastron Distance.....	39
Fig.20 Percentage of Particles by Type vs Perturber Mass.....	40

Fig.21 Percentage of Captured Particles vs Perturber Mass.....	41
Fig.22 Percentage of Unbounded Particles vs Perturber Mass.....	42
Fig.23 Velocity Distribution for Unbounded Particles M=1.....	43
Fig.24 Velocity Distribution for Unbounded Particles M=10.....	44
Fig.25 Mean Velocity of Unbounded Particles vs Perturber Mass.....	45
Fig.26 Average Velocity of Unbounded Particles vs Perturber Mass.....	45
Fig.27 Initial Mass Distribution of Disk's Rings.....	46
Fig.28 Cumulative Mass of Unbounded Particles vs Periastron Distance.....	47
Fig.29 Cumulative Mass of Unbounded Particles vs Perturber Mass.....	48
Fig.30 Percentage of Test Particles by Type for Different Inclinations M=1.....	49
Fig.31 Velocity Distribution for Unbounded Particles M=1 (Inclination).....	50
Fig.32 Percentage of Unbounded Particles vs Inclination.....	51
Fig.33 Mean Velocities of Unbounded Particles vs Inclination.....	51
Fig.34 Mean Velocities vs Angle of Periastron.....	52
Fig.35 N-body cluster evolution simulation for planetesimal velocities.....	55
Fig.36 Velocity Histogram of Planetesimals interacting with Giant Planets	56
Fig.37 Velocity Histogram of Planetesimals due to AGB stellar winds.....	57
Fig.38 Percentage of Test Particles by Type for Different Periastron Distances M=0.3.....	62
Fig.39 Percentage of Test Particles by Type for Different Periastron Distances M=0.5.....	63
Fig.40 Percentage of Test Particles by Type for Different Periastron Distances M=0.75.....	64
Fig.41 Percentage of Test Particles by Type for Different Periastron Distances M=1.5.....	65

Fig.42 Percentage of Test Particles by Type for Different Periastron Distances M=2.....	66
Fig.43 Percentage of Test Particles by Type for Different Periastron Distances M=5.....	67
Fig.44 Percentage of Test Particles by Type for Different Periastron Distances M=20	68
Fig.45 Percentage of Test Particles by Type for Different Periastron Distances M=50.....	69
Fig.46 Velocity Distribution for Unbounded Particles M=0.3.....	70
Fig.47 Velocity Distribution for Unbounded Particles M=0.5.....	71
Fig.48 Velocity Distribution for Unbounded Particles M=0.75.....	72
Fig.49 Velocity Distribution for Unbounded Particles M=1.5.....	73
Fig.50 Velocity Distribution for Unbounded Particles M=2.....	74
Fig.51 Velocity Distribution for Unbounded Particles M=5.....	75
Fig.52 Velocity Distribution for Unbounded Particles M=20.....	76
Fig.53 Velocity Distribution for Unbounded Particles M=50.....	77
Fig.54 Percentage of Test Particles by Type for Different Inclinations M=10.....	78
Fig.55 Velocity Distribution for Unbounded Particles M=10 (Inclination).....	79
Fig.56 Velocity Distribution for Unbounded Particles M=1 (Angle of Periastron).....	80
Fig.57 Cumulative Mass for Unbounded Particles (Inclination).....	81
Fig.58 Distribution of Particles as a function of Radius.....	81

List of Tables

Table.1 Percentage of Unbound Particles vs Periastron Distance.....	60
Table.2 Percentage of Unbound Particles vs Perturber Mass.....	60
Table.3 Percentage of Particles Bounded to Star 2 vs Perturber Mass.....	60
Table.4 Mean Velocity of Unbounded Particles vs Periastron Distance.....	61
Table.5 Cumulative Mass of Unbounded Particles vs Periastron Distance.....	61
Table.6 Cumulative Mass of Unbounded Particles vs Perturber Mass.....	61

Introduction

The recent discovery of two interstellar objects of extrasolar origin have spurred an interest within the astronomical community to understand their properties. The way it is determined that such objects are indeed from an extrasolar origin is by carefully measuring their orbits. Through astrometrical measurements of their movement across the night-sky their eccentricity is determined. From our knowledge of classical mechanics we know that if the value of such eccentricity is bigger or equal than 1 and that if it can be excluded that they interacted with one of the planets of our own solar system such objects are of interstellar origin and thus not bounded to the solar system. In the past three years, two objects with a large eccentricity have been found to travel close enough to the Earth as to be detected. This was the case for 'Oumuamua [ISSI Team, 2019] in 2017 and Borisov [Guzik et al., 2019] in 2019. These objects are interesting because they have the potential of revealing information about the mechanisms which give rise to them. This is especially the case for close encounters of stars and disks. Such disks can contain a large reservoir of planetesimals that can be released during such a fly-by.

In order to investigate the aforementioned dynamical process of these encounters, computational simulations are performed. This is done through a numerical method that primarily takes into account the gravitational interactions between the disk and the perturbing star. In this way we can try to see how the fly-by parameters affect how the system evolves. For instance, the code allows us to understand how the interaction changes with varying mass of the perturbing star, its distance from the disk, the angle of inclination or angle of periastron. It is by understanding how the particles conforming the disk evolve with time that we can gain an insight into how objects such as Oumuamua and Borisov are launched into interstellar space. The main goal of the analysis is to understand the properties of unbound disk particles that result from such perturbation events.

1 Overview and Background

1.1 Origin of ISO

There are several processes that could lead to the production of interstellar objects. These potential formation scenarios each propose a different physical mechanism. In this thesis we will focus only on the process that strips material from the protoplanetary disk during close stellar encounters in cluster environments. Most mechanisms assume that interstellar objects are planetesimals that were created as a by-product of planet formation in disks. These planetesimals were not incorporated into the planets themselves but became part of the debris disk that remained after planet formation. Such planetesimals can be ejected by a variety of processes from their parent/host system and become interstellar objects thereafter. The main four mechanisms will be shortly summarized in the next paragraphs.

Firstly, the expulsion of material from their stable orbits due to stellar winds coming from an

asymptotic giant branch (AGB) stellar phase. In this scenario we can imagine how ISOs could be accelerated due to the transfer of momentum from the photons and protons ejected during this period of expansion of the star's outer layers. The simulations have shown that there is a significant portion of loosely bound planetesimal material that gets ejected during this process [Veras,2020]. This mechanism is unique in that it creates ISOs not at the beginning of the evolutionary lifetime of the planetary system but rather during the end of it. Agúndez et al. [2007] looked into the chemical complexity of circumstellar envelopes of carbon-rich AGB stars. They found out new molecular species for the first time around an AGB star previously only known to exist in the interstellar medium. This could potentially indicate that the chemical composition of ISOs could be more complex than previously thought.

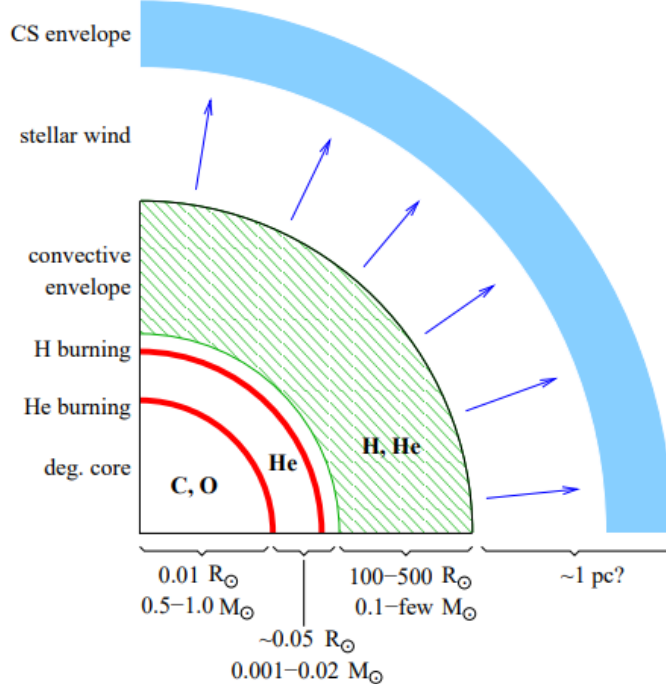


Figure 1: Schematic structure of an AGB star during its thermally pulsating phase [Pols, 2011]

Second, gravitational interactions between the orbiting material and the giant planets of that stellar system [Adams and Spergel, 2005]. These planets are able to affect the dynamics of the objects in such a way that their orbits become hyperbolic and thus become unbounded. In particular, it has been investigated that orbits that approach too close to a massive planet become chaotic. Planetesimals on such special orbits either collide with the planet or instead get ejected from the planetary system into interstellar space. An outer massive planet interacting with the disk directly ejects planetesimals and migrates inward, compressing the system and leading to instability or resonant capture [Raymond, Armitage, Gorelick, 2009]. Excitations of planetesimals caused by the resonances of a giant planet in a protoplanetary disk also

change the chemical composition of planetesimals. Nagasawa et al. [2018] found that the highly excited planetesimals generate bow shocks leading to chondrule formation, crystallization of silicate dust and evaporation of icy planetesimals. This research might help constraint models by looking at the spectroscopic signature of unbounded planetesimals. Also, as reflected in Fig. 2 the maximum relative velocities achieved in this kind of interaction lie between 5 and 20 km/s, velocities outside the range of stellar gravitational interactions (see Hands, 2019).

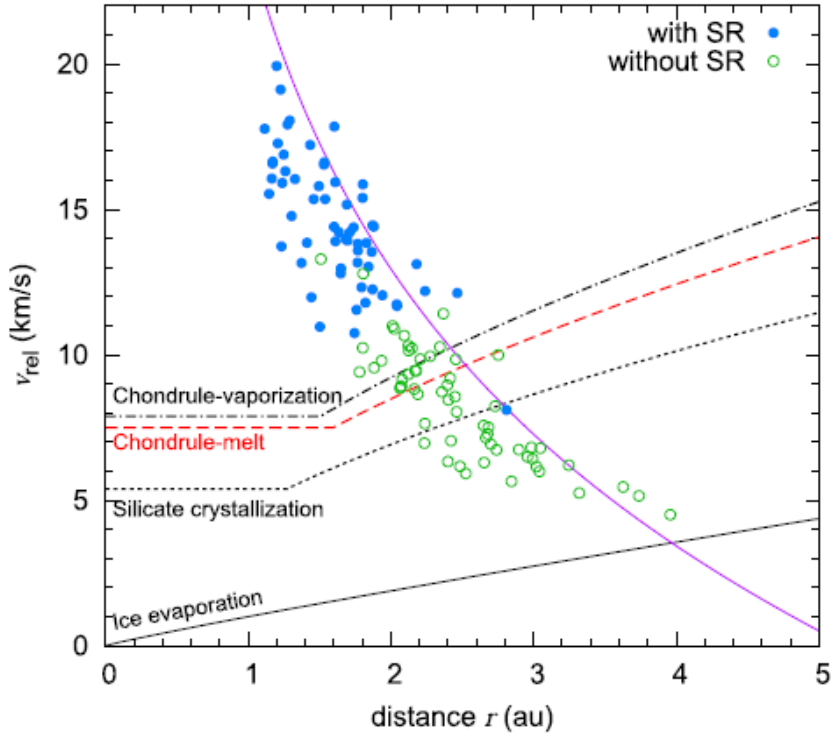


Figure 2: Required relative velocities of planetesimals for specific chemical processes to take place [Nagasawa et al. 2018].

Third, tidal disruption by a white dwarf or a binary stellar system. In this scenario, the gravitational interaction from these objects perturbs the orbit from planetesimals. Jackson et al. [2017] argued that the galactic budget of interstellar objects like ‘Oumuamua should be dominated by planetesimal material ejected during planet formation in circumbinary systems, rather than in single star systems or widely separated binaries. Mathematical analysis show that in order to produce the ejection of such small bodies it is required that the companion star exceeds the Keplerian orbital velocity at its semi-major axis [Wyatt et al., 2017 as cited in Jackson et al., 2017]. The relative abundances of binaries is around 50 percent while for gas giants is around 5 to 10 percent. This would imply that around 3/4 of interstellar objects originate from tight binaries [Jackson et al., 2017].

Fourth, the stripping of materials from the protoplanetary disk during stellar encounters. In this scenario there is a whole range of possibilities for these type of encounters spanning a full range of mass ratios, inclination, angle of periastron and periastron distance. As it is well known, stars are born not in isolation but instead they form in clusters [Lada Lada, 2003]. This means that this environment is extremely important in determining how the stellar disk evolves given the high density of stars. Vincke & Pfalzner [2016] did a comprehensive study of cluster dynamics. They performed an N-body simulation that recorded the fly-by history of each of the stars in the cluster. Then through the use of the results from related parameter studies the effect on the disks was studied [Scally & Clarke 2001; Olczak et al. 2006; Pfalzner et al. 2006; Olczak et al. 2010; Steinhausen & Pfalzner 2014 as cited in Vince & Pfalzner, 2016]. These simulations took more features of the cluster dynamics and the fly-bys characteristics into account. They showed that in dense cluster environments close fly-bys can become relatively common. The unique feature of this study is that the early stages of the cluster development were considered, namely its evolution from the embedded throughout the expansion stage.

In this thesis work the main focus of the analysis is on the velocity distributions of the ejected particles assuming the mechanism of the fourth scenario.

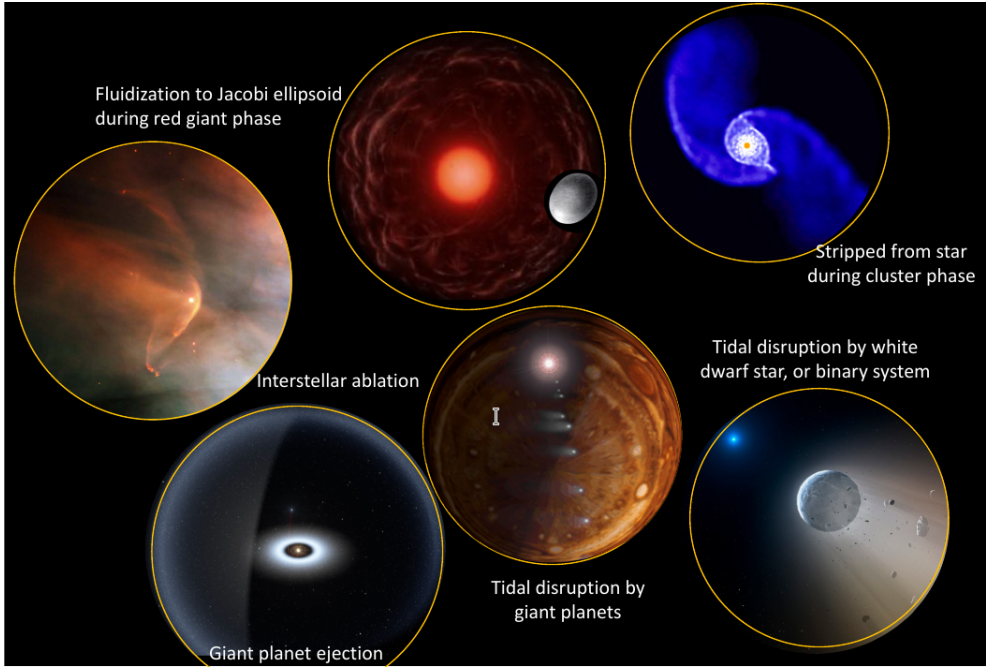


Figure 3: Potential Formation Scenarios for Interstellar Objects [‘Oumuamua ISSI Team, 2019]

1.2 Protoplanetary Disk Physics

Protoplanetary disks are by-product of star formation and their evolution and development is an active area of research. There has been plentiful of interest in the specific dynamics and

mechanisms that lead to the collapse of Giant Molecular Clouds (GMC) into such disks. Inside GMCs turbulent processes happen in such a way that the cloud collapses in a multi-scale and multi-epoch fashion. It has been suggested that clouds develop multi-scale gravitational contractions while seeded with density fluctuations produced by the turbulence [Vazquez-Semadeni et al., 2019]. It is worth noticing that this process is extremely nonlinear. This means that the process is relatively slow during most of its initial time but later the collapse is extremely rapid towards the end [Girichidis et al., 2014 as cited in Vazquez-Semadeni et al., 2019]

The definition of Jean's Mass is a very useful tool to conceptualize the conditions under which spheres of mass collapse. In a study by Gómez and Vazquez-Semadeni [2014] the authors observed the formation of filaments in numerical simulations of contracting clouds. In a sense, this process can be conceptualized as filaments being akin to rivers that transport the gas from the cloud to the dense cores where star formation occurs.

$$M_J = \frac{\pi^{\frac{5}{2}}}{6} \frac{C s^3}{G^{\frac{3}{2}} \rho^{\frac{1}{2}}} \quad (1)$$

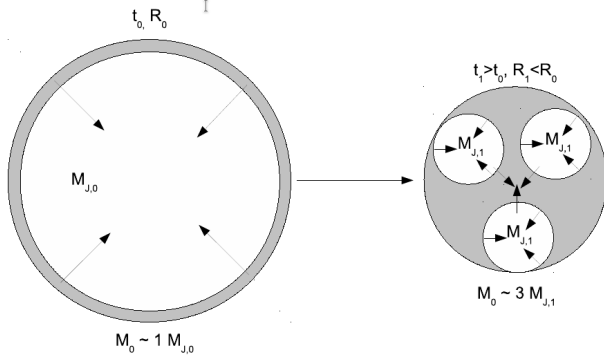


Figure 4: Hierarchical Collapse Model [Vazquez-Semadeni et al., 2019]

Studies have suggested that star formation is characterized by short but intense bursts of activity. These bursts in turn destroy their parent clouds before most of their mass can be converted to stars. The stellar-particle mass distribution evolves towards increasingly bigger high-mass particles as time progresses. The feedback from these massive stars in turn erode the structure of the cloud decreasing the star formation rate (SFR). From numerical simulations it has been suggested that if turbulence dominates, the mass distribution becomes more top-heavy [Clark et al. 2008; Bertelli Motta et al. 2016 as cited in Vazquez-Semadeni et al., 2019]. This period of SFR activity has been conceptualized as a non-homologously-collapsing spherical core, which in turn can be thought as independently collapsing concentric spheres. This means that an atom has to travel from low-density regions to high-density regions before it is in a position to

give birth to a star.

Another relevant phenomena that affects the formation and dynamics of protoplanetary disks is the presence of magnetic fields. For instance, 2D asymmetrical numerical simulations of the collapse of magnetized rotating cores show that angular momentum is almost completely removed from the collapsing material through magnetic breaking [Tomisaka 2000; Allen et al. 2003 as cited in Lam et al., 2019] . Non-ideal MHD (Magneto Hydro-Dynamic) scenarios have been studied as well, and they have shown that smaller disks result in the presence of Ohmic dissipation and ambipolar diffusion. As it has been pointed out in the previous paragraphs, turbulence enabled the formation of disks at the earliest stages of its evolution but it was ambipolar diffusion that allowed the disks to persist at later times. In order for disks to remain stable and avoid disintegration there needs to be a mechanism that allows for the dissipation of extra angular momentum. The existence of Herbig-Haro objects is an example of this underlying physical mechanism in action. There are several ways in which magnetic related mechanism support disk formation via turbulence. For instance, it has been found that magnetic diffusion [Santos-Lima et al., 2012 as cited in Lam et al., 2019], tangling of magnetic field lines [Seifried et al., 2013 as cited in Lam et al., 2019], field-rotation misalignment [Seifried et al. 2013, as cited in Lam et al., 2019], and pseudodisk warping [Li et al., 2014 as cited in Lam et al., 2019] support magnetic induced turbulence. Nonetheless, it is not guaranteed that the disk will survive the whole process and thus it depends on many factors, amongst them: degree of magnetization, level of turbulence, the initial density distribution of the core, the rate of core rotation and the degree of coupling of the magnetic field and the bulk neutral cloud material.



Figure 5: Herbig Haro Object [ESO/M. McCaughrean,2015]

The evolution of the structural properties of the clouds is another aspect that sheds some light over how the protoplanetary disks might form and evolve. There has been studies that looked into how structures at different scales form as a function of time using state of the art simulation magneto-hydrodynamic codes. In particular, Ossenkopf et al. [2001] analyzed this aspect of

GMCs and derived some interesting statistical facts. In their paper they utilized the Δ -variance tool [Stutzki, 1998 as cited in Ossenkopf et al., 2001] to measure the amount of structure present at different scales in an N-dimensional data set. This value is computed by doing a convolution of the N-dimensional structure with a normalized spherically symmetric function and measuring the remaining variance. In order to make a comparison between the simulations and the observational data the authors always used the two-dimensional representation of the Δ -variance. In the following plot it is clearly illustrated how the strength of temporal density fluctuations in a self-gravitating cloud changes as a function of scale. As it can be appreciated the Delta variance decreases with smaller scales and asymptotically converges to distinct values as time progresses.

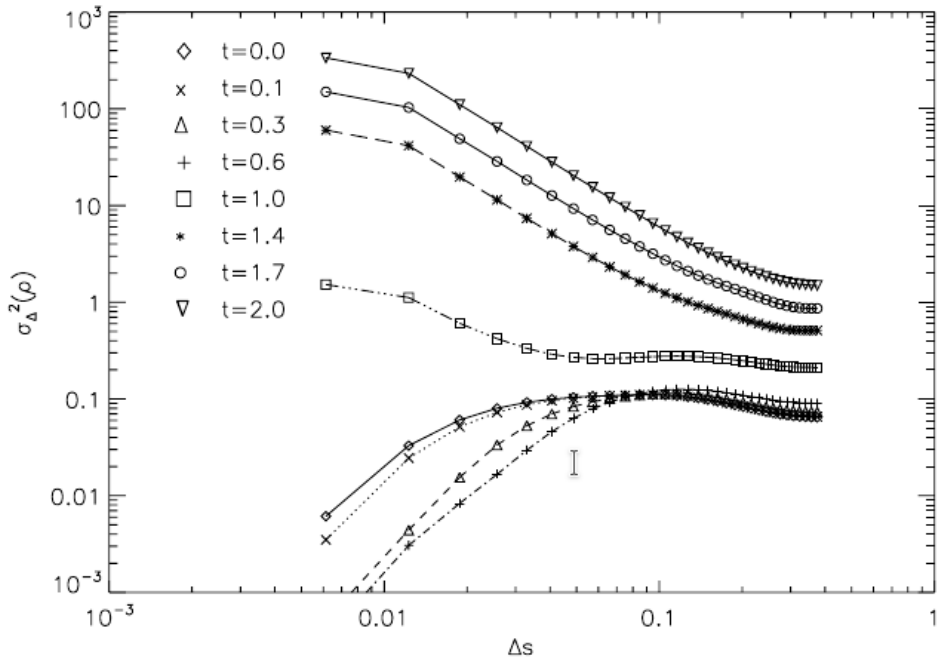


Figure 6: Δ -variance of a self-gravitating cloud [Ossenkopf et al., 2001]

By understanding the chemical complexity of protoplanetary disks we can complement our knowledge of how planets and planetesimals are formed. This in turn can allow us to understand the physical composition of the ejected planetesimals. It is thought that the chemistry of the planetary system is either 1) the inherited material from the cloud, 2) processed material within the disk or 3) a combination of both [Pontoppidan et al., 2014; Drozdovskaya et al., 2018 as cited in de la Villarmois et al., 2019]. The physical processes at small scales is still not well understood and thus is an active area of current research. One very effective way to study these processes is through the conspicuous spectroscopic signatures of molecules due to the large variation in densities and temperatures of the protoplanetary disk environment. The determination of how the mass of the system evolves depends on the rate of mass gain as well as the mass loss through outflows mechanisms. In de la Villarmois et al. [2019], the authors

performed a comparative study on the chemistry and physical properties of class I protostellar sources. By utilizing the ALMA (Atacama Large Millimeter/Submillimeter Array) they studied a representative sample of 12 protostars from the Ophiuchus molecular cloud. They found an inverse relationship between stellar mass and envelope mass. Furthermore, a power law relation between the stellar mass and the bolometric luminosity was found. By looking at the $C^{17}O$ line they traced the densest and colder regions of the disk-envelope system while SO_2 traced the higher temperature regions such as the accretion shocks. These observations helped shed a light on the formation and evolution of protoplanetary disks based on the diverse molecular signatures they emit.

1.3 Cluster Environments

One of the main characteristics of star formation is that stars rarely form in isolated environments [Lada & Lada, 2003]. In young open clusters they naturally associate themselves in groups of a few tens up to thousands. For this reason, it is important to understand how this environment has an impact on the formation and evolution of disks. Here, the most relevant aspects are summarized.

One of the central themes of any investigation of clusters is the study of what is the distribution of the types of stars born within it. In other words, what is the stellar mass distribution resulting from a single star formation event. The IMF (Initial Mass Function) is mathematically expressed in the form of a multipower law. Astronomers have developed a canonical mass function that is used as the standard mass distribution. From this mathematical description there is a known percentage of stars for every mass range. One common IMF was developed by Salpeter in 1955 [as cited in Offner et al., 2013] where the value of alpha was fine tuned to 2.35 to match the observational data.

$$NdM \propto N^{-\alpha} dM$$

Other proposed forms have a truncated exponential in the form [de Marchi and Paresce, 2001; Parravano et al., 2011 as cited in Offner et al., 2013]:

$$dN \propto M^{-\alpha} (1 - \exp[(\frac{-M}{M_p})^{-\beta}]) dM$$

Young clusters are characterized by their loose appearance and the number of stars they contain. This number lies within the range from 100 to a 1,000 members [Schombert, 2020]. A study by Zwart et al. [1998] demonstrated through an N-body simulation for the initial conditions of R136, a young compact cluster that physical collisions between stars are frequent and that “*the most massive stars and the dynamical evolution of the cluster are closely coupled. In all cases, a single star grows steadily in mass through mergers with other stars, forming a very massive star in less than 3–4 Myr*” . The influence of the cluster environment on the disks remains an active area of research. The collisions between stars in the cluster is one natural candidate of a mechanism that might impact the development of the disk, for instance, in the size of the

post-encounter disk [Bhandare, 2015]. Oliveira et al. [2003] observed individual members of the sigma Orionis young cluster whose estimated age is 4 Myr. By looking into the LiI and NaI spectral lines it was found that at least 30% of the low-mass members had disks. When compared to other young clusters of similar ages it fitted nicely between these clusters (NGC 2264 at (52%) \sim 3.2 Myr and NGC 2362 (12%) at \sim 5 Myr). This result reveals that the protoplanetary disks are highly susceptible to conditions within the cluster. These include the influence of massive stars, the cluster's gas expulsion and the gravitational interactions amongst the members.

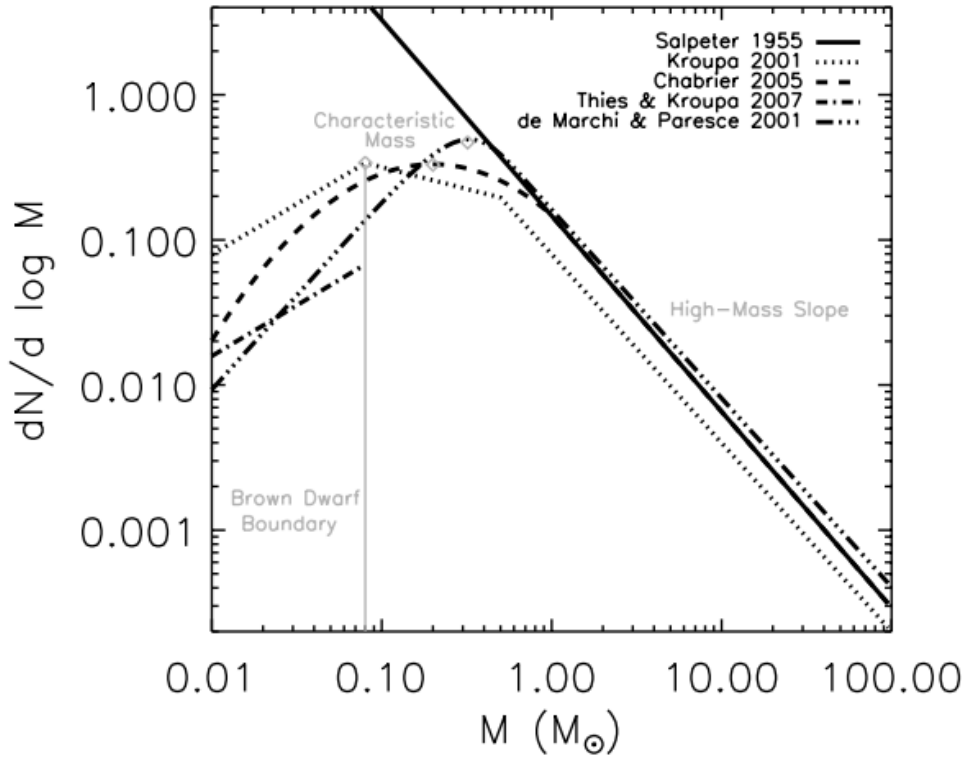


Figure 7: IMF functional forms proposed by various authors from fits to Galactic stellar data. All the recent IMFs are normalized to unity [Offner et al., 2013].

When there is an excess of stars in the lower end of the distribution this is called a bottom-heavy IMF, on the other hand, if there is a deficit of stars in the lower end of the distribution this is called a bottom-light IMF. The same thing applies for the upper end of the distribution. Studies of globular clusters, ultra compact dwarf galaxies and young massive clusters point to the direction that low metallicity and high gas density make the stellar IMF to become top-heavy [Dabringhausen et al., 2009; Dabringhausen et al., 2012; Marks et al., 2012; Zonoozi et al., 2016; Haggi et al., 2017; Kalari et al., 2018; Schneider et al., 2018 as cited in Dabringhausen et al., 2018]. Metal rich environments on the other hand produce bottom heavy IMF [Kroupa

2002; Marks & Kroupa 2012 as cited in Dabringhausen et al., 2018]. The IMF of two different star forming events (A and B) will not be the same as a bigger event containing the same number of stars given that there are many factors that affect how such distribution behaves. For this it is necessary to take into account the specific conditions of each star forming region to accurately describe the galaxy wide IMF.

One useful descriptor of a cluster's physics is the kinematics of the stellar bodies within it. Through precise astrometric techniques it is possible to measure the kinematic properties and spatial distribution of individual stars that in turn allow for the study of the cluster as a whole. Rao et al. [2019] published a paper of the kinematic properties of O and B stars in the Cyg OB3 region located at distance of about 2 kpc away. Using astrometric data from Gaia DR2 they observed 45 stars and found they were moving at a peculiar velocity of 20 km per second. The small dispersion in this quantity reinforces the current idea that the cluster forms a coherent structure in velocity space [Brown et al. 1999; Tian et al. 1996; Mathieu 1986 as cited in Rao et al., 2019]. They calculated the relative velocities of the individual stars relative to the association, in other words, the drift. The low velocities indicate that Cyg OB3 is a slowly expanding association. There were some particular stars that showed some interesting kinematic behaviour attributed to past encounters in a denser environment. The density in cluster environments is highest during the formation process, before gas expulsion leads to the expansion of the cluster.

State-of-the-art simulations of the star formation rate, the IMF, as well as total star formation efficiency in molecular clouds have been for long regarded as the highest standard of research in this field. A paper by He, Ricotti & Geen [2019] explored exactly this theme by performing a large set of radiation-magneto-hydrodynamic simulations of star formation in self-gravitating, turbulent molecular clouds, modelling individual massive stars and their UV feedback to the cloud. The parameters used to calibrate their simulations were obtained from independent astronomical observations. They found that the Kroupa stellar IMF can be reproduced with the assumption that each stellar-forming gas clump fragments into stars with a power law mass function Γ of about 0.8. It was found that low and intermediate mass stars form first, to then be followed by their more massive counterparts. By recreating a large set of possibilities for the molecular clouds the authors were able to compare them to the observational results and further constraint their models. Amongst the properties that were considered for the different simulations were: cloud mass, density, metallicity, star formation efficiency, star formation rate and IMF slope. The following figure (see Fig. 8). summarizes these findings for three distinct molecular clouds. Their assigned names refer to a specific set of parameter values.

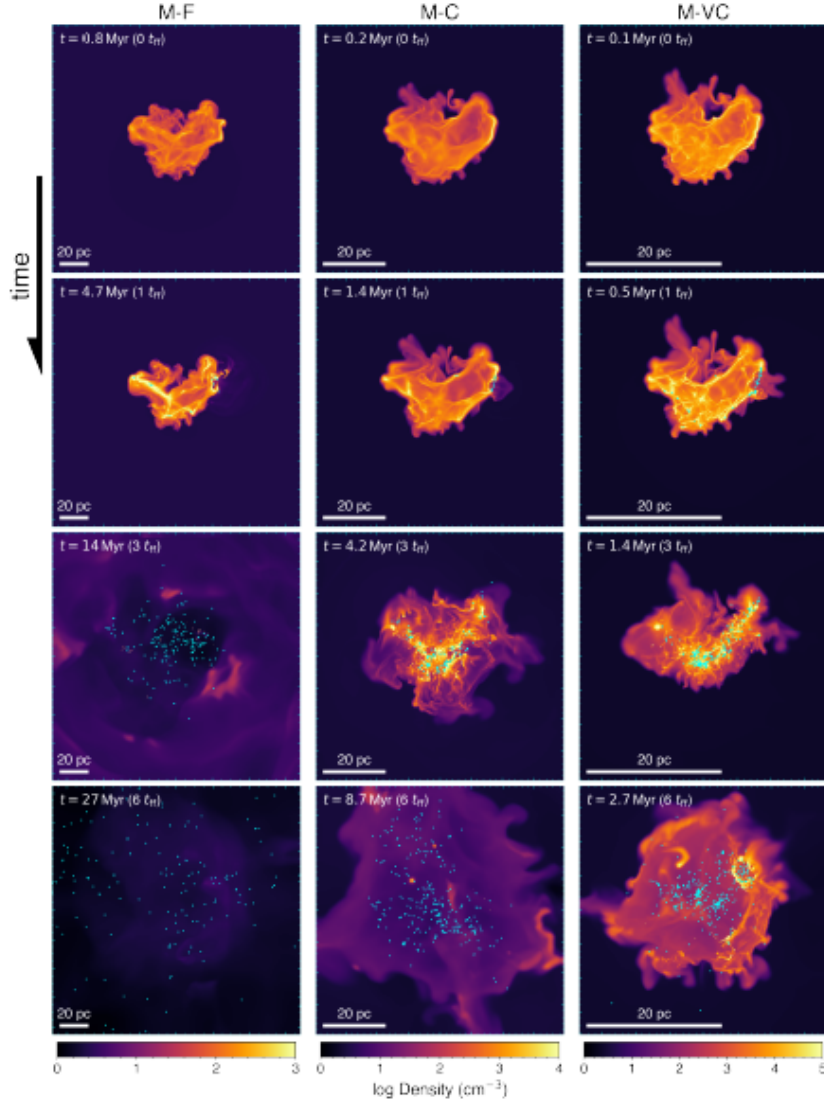


Figure 8: Line-of-sight projections of the gas density for three distinct simulations with varying mean number density. The snapshots of the upper row show the initial conditions of the cloud dominated by gas. On the other hand, the snapshots in the lower row show the phase in which most of the gas has been expelled due to the feedback of massive stars [He, Ricotti & Geen 2019].

In a recent paper Krumholz & McKee [2019] investigated several candidate scenarios for the formation of bound star clusters. The goal was to look into how mass is assembled, how it evolves and how it turns into stars. By using the spectroscopically estimated ages of stars and a large sample of star-forming gas clumps they were able to construct models and compare them to the observational data. What they showed was that for the model in which the acceleration of star formation is due to large-scale collapse the increased star formation efficiency is not able to match the observational constraints. On the other hand, "conveyor belt" models

in which gas accretion and star formation happen simultaneously but the free-fall time is low were able to match the observed data. A Bayesian forward-modelling of the observational data was performed as to reduce the uncertainties and biases. They were able to conclude that gas accretes at an increased rate meanwhile the central cluster-forming region is not in a state of global collapse resulting in a star formation efficiency per unit mass both low and constant in time.

The era of state-of-the-art space telescopes like Spitzer and Herschel have helped astronomers understand the star formation processes in Galactic forming sites [Churchwell et al. 2006; Andre et al. 2010, 2014 as cited in Dewangan, 2019]. The topic of how filaments are involved in the formation of dense massive star forming clumps and young stellar clusters continues to be an active area of research. Specifically, the zone where interaction/collision of filaments take place have been designated as suitable candidates for the formation of massive OB stars ($M_{\odot} \geq 8$). In a paper by Dewangan [2019] the author performed an investigation of the star formation process happening in AFGL 5157 (area 13.5 pc x 13.5 pc) utilizing a range of multiwavelength datasets. Using the Herschel sub-mm continuum images and molecular line data it was found that in the observed site three embedded filament are identified using column density maps. Furthermore, by making an analysis of Spitzer images of Photon Dominated Regions (PDRs) are identified in AFGL 5157, indicating the presence and impact of massive stars. In conclusion, the cloud-cloud collision that occurred in the past might have triggered star formation in this site.

1.4 Stellar Encounters

The next logical step is to discuss how protoplanetary disks are affected by stellar encounters within the cluster they are immersed in. Specifically, how the gravitational interactions between stars affect the evolution of the disks. One source of motivation for the study of these interactions is the observation of the relative alignment or misalignment between the orbital momentum vector of an exoplanet and the rotation axis of the stellar host. Spin-orbit misalignment has been measured in at least 100 different exoplanets [Fabrycky & Winn, 2009; Johnson et al., 2009; Triaud et al., 2010; Moutou et al., 2011; Albrecht et al., 2012; Mancini et al., 2015 as cited in Breslau and Pfalzner, 2018] It is possible to imagine that this misalignment occurs either in the planet formation phase, afterwards or in both cases. In this particular paper [Breslau and Pfalzner, 2018] the authors looks into the production of retrograde planetary orbits that are initially and finally bounded to the host star by the fly-by of a perturber star. They performed a three dimensional, purely gravitational, numerical three-body simulation using between tracer particles. The results from this investigation led to the conclusion that generating a retrograde orbit is very unlikely for low-mass encounters regardless of their orientation. In contrast, it was found that it is equal-mass prograde co-planar encounters and not their retrograde counterparts that produce the highest proportion of retrograde objects at 13%.

Relevant to this topic are the tidal disruption effects on such disks. One of the first studies looking into star-disk encounters was performed by Hall, Clarke & Pringle [1995]. In particular

they looked into the response of a circumstellar accretion disk to the fly-by of a perturbing mass on a parabolic orbit. They utilized the three-body restricted method to calculate how the test particles would transfer energy and momentum with the incoming star. Particles become either unbound, captured, or remain bounded. After presenting their results they concluded that non-linear treatment of the problem was paramount, especially for the close encounter cases. In a study by Kremer et al. [2019] the authors studied how the dynamical interactions were able to unbind a large proportion of planets from their host stars. Using the cluster Monte Carlo code CMC to explore the evolution of such planetary systems it was found that between 10% and 50% of primordial planetary systems are broken through the a cluster's full lifetime. This entails that a significant proportion of planets will become "free-floating objects". Furthermore, in this paper it was explored how it is possible to constraint the model of planet and black hole formation and evolution by looking at the observational trace signals resulting from a Planet-BH encounter. The reason this research is relevant is that it shows that in cluster environments dynamical interactions eject the bodies orbiting the host star. It is possible to imagine that planetesimals can be ejected from the cluster at it is suggested by the authors that between 30% and 80% of primordial planets are ejected from their host cluster. Scally and Clarke [2000] investigated the process of disk destruction from both stellar encounters and UV radiation from massive stars. By using an N-body simulation replicating the condition of the Orion Nebula Cluster (ONC) they modelled the evolution and dynamics of 4000 stars with their disks. In their findings the minimum stellar encounter separation peaked at 1000 au meaning that less than 10 percent of the members had an encounter closer than 100 au after 10^7 years. Their results suggest that significant destruction of the disks are rare and that planetary systems such as ours are likely to be common in ONC-like environments. On the other hand, in Olczak et al. [2006] it was found that considerable mass loss in the disk during the lifetime of the cluster was more pronounced in the inner most dense regions. Between 10 and 15 percent of disks located at the densest regions of the ONC are destroyed due to stellar encounters. The implication of this study is that the production of potential ISOs are not homogeneously produced through the cluster but that it is mostly relegated to the innermost regions of it. Then, one would expect that given the average separation of members of the an open cluster they effortlessly escape from it and become free to travel through interstellar space.

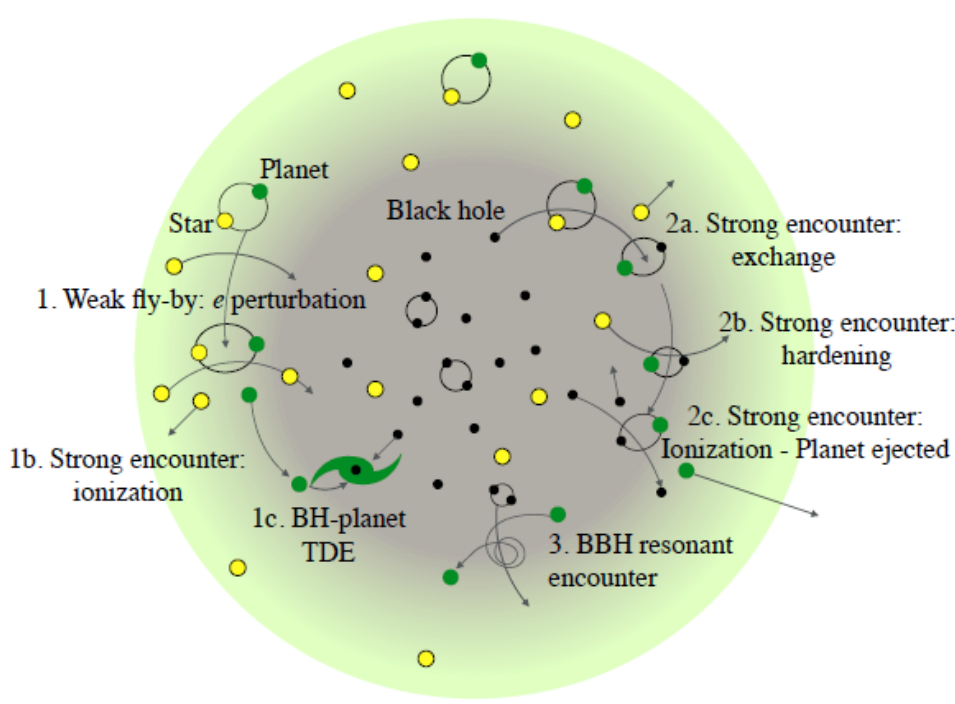


Figure 9: Summary of different dynamical encounters occurring in a cluster environment [Kremer et al., 2019]

A very relevant paper for this thesis work is a study of the restricted three-body problem for star-disk encounters. In actuality, the code enabling these simulations was the one used for this thesis work, albeit the pertinent modifications. In this particular case, the authors looked into a subset of this problem. More specifically, they took into consideration only parabolic encounters between disks of non-interactive low-mass particles and perturber stars of different masses for the co-planar prograde cases [Breslau et al. 2016]. Their goal was to see how the properties of the planetesimals numerically depend on the encounter characteristics. By setting up the disks and simulating the encounters they were able to depict the final properties of the particles mapped onto their original disk location. One of the conclusions that came out from this study is that the closer the perturber orbit, the higher the final eccentricities and the larger the semi-major axes of the particles that remain bound to the host. The following figure shows exactly that.

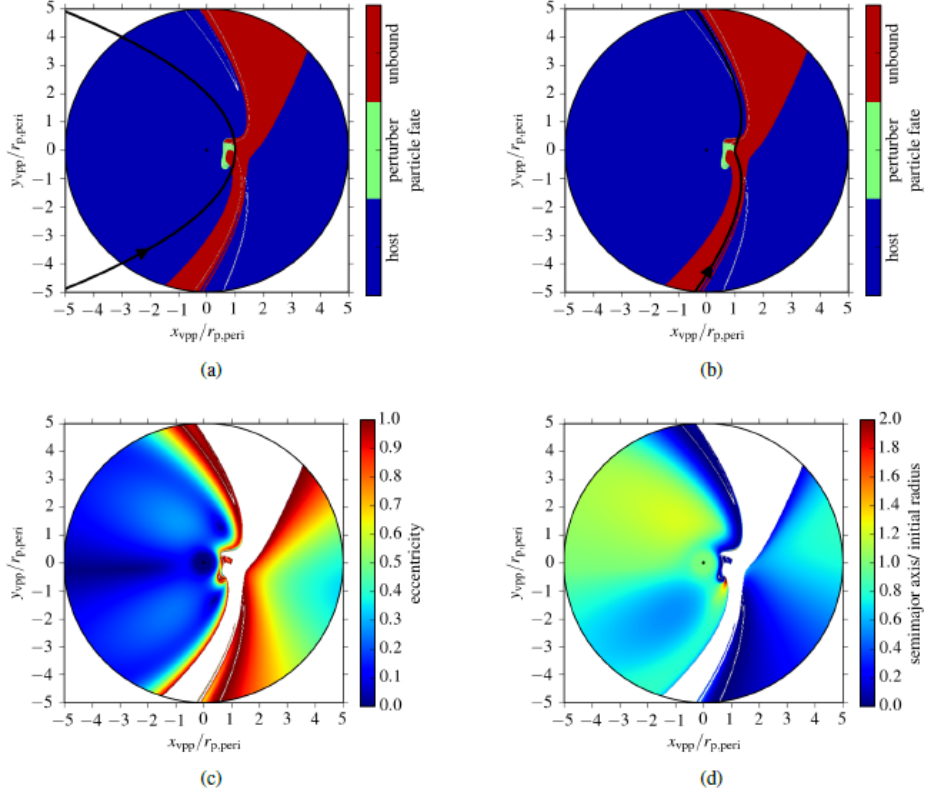


Figure 10: Particles mapped to initial disk location showing different properties: a) and b) shows whether particles become unbound, bound to host and bound to perturber, c) shows the final eccentricity of particles and d) shows the final semi-major axis relative to the radii of initial orbit [Breslau et al., 2016]

The transfer of energy and momentum from these star-disk encounters have been a subject of interest for the community for a long time [Larwood & Kalas, 2000; Thies et al., 2005]. Most research has been performed with the help of computational tools that in one way or another describe different aspects of this phenomena. Ida & Kobayashi [2001] investigated the evolution and formation of our own solar system using numerical simulations. In contrast, a study published by Ostriker [1994] presented an analytical approach on the study of compressional and transverse disturbances using linear perturbation theory. A binary companion, for instance, can exert a considerable influence on a nebular disk due to the gravitational torque it exerts. For the cases where the companion star is sufficiently distant to the disk that the influence will be treated as a perturbation [Goldreich & Tremaine, 1979 as cited in Ostriker, 1994]. These interactions are associated with certain resonances; 1) corotation resonance and 2) Lindblad resonances. The former corresponds to the positions in the disk where forcing frequency from the perturber in the frame rotating with the disk is zero, while the latter where the Doppler-shifted perturbing frequency is the same as the local epicyclic. The author de-

rived the expressions for the energy E and angular momentum L transferred to a differentially rotating disk during a star-disk encounter, valid to the first order in the disturbance. Several conclusions came up from this study. First, that a disk will give up its angular momentum to an unbound perturber leading to a reduction in the disk's own momentum. It was found that the strength of the gravitational torques plummets with increasing periastron distance relative to disk radius first as an exponential and then at larger ratios as a power law. Second, that the capture of perturber stars cannot be responsible for most wide binaries in spite of the disk being quite susceptible to external disturbances.

Most of the investigations on the effect of stellar encounter on disk properties have been focused solely on the parabolic, co-planar case. This is because it is the most destructive configuration of all. In a paper by Bhandare et al. [2018], the authors performed a comprehensive study that took into account the effect of the more common inclined encounters on the disk size of protoplanetary disks. The parameter space covered a whole range of mass ratios, periastron distances and orbital inclinations. This parameter space represented the conditions that can be found in young stellar clusters. They found that, as expected, the co-planar prograde encounters had a stronger effect on the disk size as compared to their inclined counterparts. Nonetheless, the inclined encounters still had a noticeable effect that could not be ignored. The differences between the prograde and the retrograde encounters were more noticeable for a small mass ratio and a big periastron distance. This changed as mass ratio increased and periastron distance decreased. The implication of this finding is that retrograde encounters are indeed very relevant and worth studying for a large fraction of the possible cases. Furthermore, it was found that the more massive and closer the perturber the more destructive it becomes.

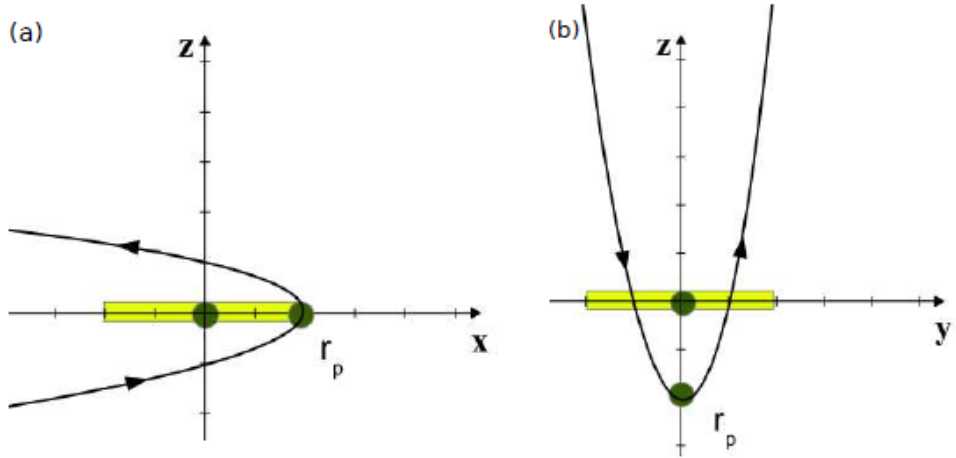


Figure 11: Sketch of disk and perturber star orbit; a) in the disk $w=0$ and b) below disk plane $w=90$ [Xiang-Gruess, 2016 as cited in Bhandare et al., 2018]

Breslau et al. [2014] further explored the themes discussed in the previous paragraph. The goal of this paper was to derive a quantitative relationship between the parameters and the disk size. By analyzing the whole parameter space for different mass ratios and different periastron distances it was found that the final radius followed the following trend:

$$r_{final} = 0.28r_{perim}m_{12}^{-0.32}$$

One of the things that is worth making an emphasis on is the fact that when dealing with disks the boundaries are not solid. There exists a continuum that stretches well beyond the initial disk size. For this reason, there needs to be a way in which to systematically determine the size of a disk. By looking at the particle and mass surface densities of the disk and locating the point of the steepest descent the outer boundary was determined. In Fig. 12 this is visually illustrated.

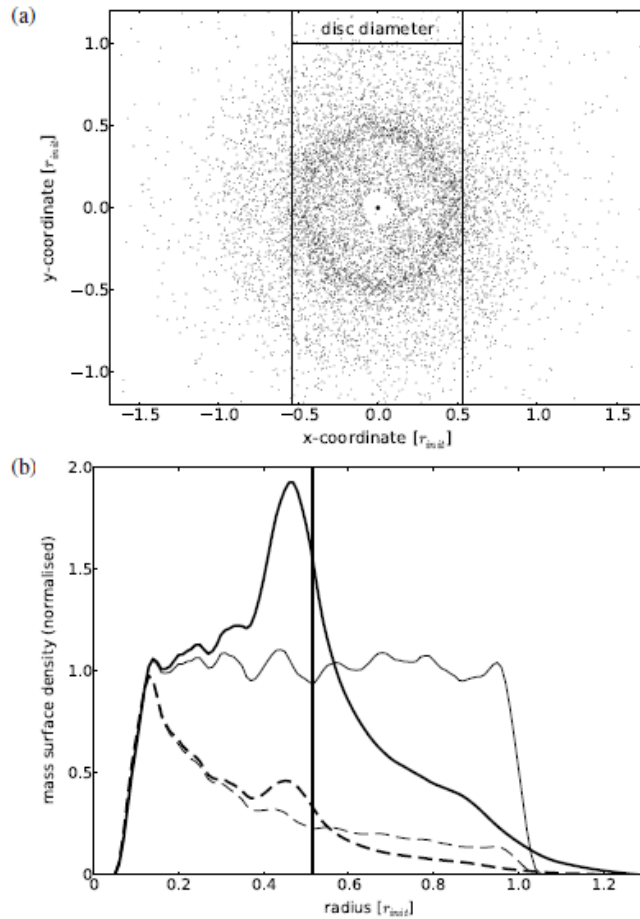


Figure 12: Disk size after stellar encounter: a) shows the face on view of the disk after a $M=1M_\odot$ encounter and periastron distance $p=2R_{int}$ b) Surface densities of particles and mass of the disk after encounter [Breslau et al., 2018]

Expanding on the aforementioned studies Bhandare et al.[2018] looked at how the inclination of the encounters affected the final disk size. What they found was that the prograde encounters had the strongest effect on diminishing the disk size with a steady increase as a function of inclination angle up until $i=140^\circ$. For the interval between $i=140^\circ$ and $i=160^\circ$ there was a spike in the size of the disk. According to the authors understanding why fly-bys within this range have the smallest effect on the disk size is not straightforward. One possible reason is that in this case particles are on highly eccentric orbits and thus it is very difficult to define the disk size given that it is not possible to observe a sharp truncation in the disk.

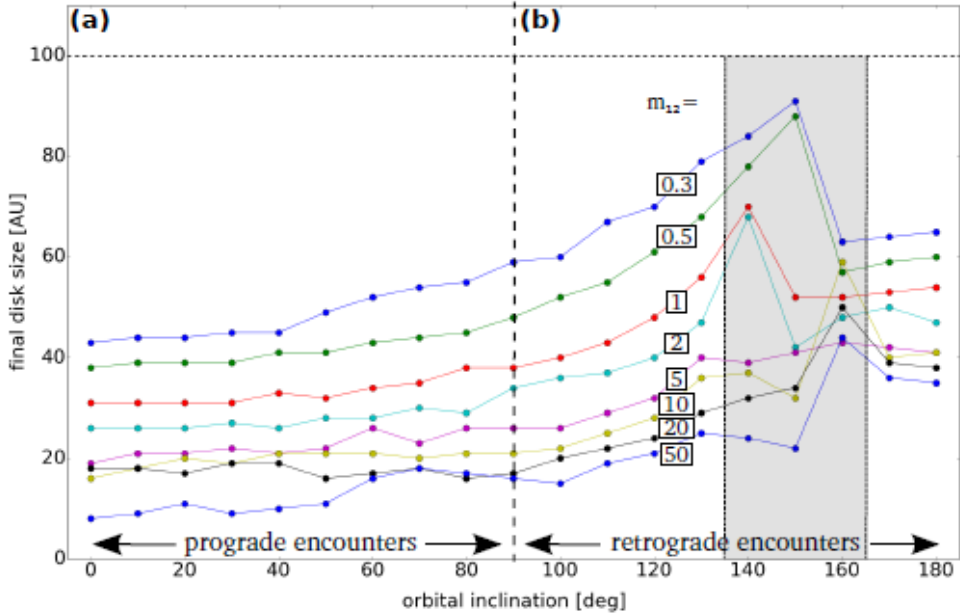


Figure 13: Final disk sizes as a function of inclination for different mass ratios [Bhandare et al., 2018]

1.5 Aim and Motivation

So far investigations of the effect of fly-bys concentrate mostly on the matter that stays bounded and to a lesser degree on the matter that becomes captured by the perturber star. Only the discovery of the first two ISOs triggered interest in the matter that becomes unbound. The proposed goal for this master thesis project is to study the physical properties of the ejected material resulting from star-disk encounters. In particular the effect different encounter parameters have on the velocities of such unbound particles. The first part of this analysis will focus on how different perturber masses and periastron distances affect the particle velocities. The second part will explore how the inclination of the encounter affects those same velocities. Thirdly, the mass distribution of the unbounded particles will be studied for both part one and two of the analysis. The overall objective is to figure out a systematic to distinguish between gravitational star-disk encounters and the other theoretical mechanism described in the “Origin of ISO” subsection.

2 Method

In this section I will present the methodology used to study these interacting disk-stellar systems. For this, it is very useful to conceptualize the simulation as being composed of three distinct modules. I will attempt to explicitly describe the specific details for each of them. But before that, some remarks about the general features and limitations of the simulation. For instance, in contrast to other N-body codes that take into account the interactions amongst all involved particles this simulation comprises only of the restricted 3-body interaction. Namely, the interaction between the host star, the perturber star and the tracer particle initially located in the disk of the host star. It is assumed that there is no viscosity mechanism acting amongst the disk particles and that there is no disk orbiting the perturber star. We do not include viscosity or self-gravity because it probably plays a minor role in the disk we are investigating. Self-gravity is only important in relatively massive disks ($M_{disk} > 0.1M_{\odot}$). In this case viscosity also plays a role, because most of the disk mass comes from gas. In these young disks the dust particles are generally small ($\mu\text{m} - \text{mm}$), ISOs by contrast are tens to hundreds of meters in size. Building such objects requires time (Myr) and thus by the time ISOs form the total mass of the disk is $M_{disk} << 0.01M_{\odot}$ and self-gravity does not play a role here. The initial orbital velocities of the tracer particles around the host star were set up to be Keplerian. The mass of the disk is assumed to be $0.01M_{\odot}$ for all the simulations. The initial disk size was also assumed to be constant for all the simulations and was set to be 100 au. These disk properties along with the parameter space described below correspond to the conditions present in young stellar clusters [Breslau, 2017]. We perform the numerical simulations of thin disks using 63,000 low-mass tracer particles. This level of resolution has been shown to be sufficient for the study of disk evolution [Kobayashi & Ida, 2001].

For the first part of the analysis the following parameter space was utilized:

- 1) Mass ratio (0.3, 0.5, 0.75, 1.0, 1.5, 2.0, 5.0, 10.0, 20.0, 50.0)
- 2) Periastron Distance (80 – 350 au)
- 3) Inclination between disk and perturber star (0°)
- 4) Orbital Orientation (0°)
- 5) Initial Disk Radius (100 au)

For the second part of the analysis the following parameter space was utilized:

- 1) Mass ratio (1.0, 10.0)
- 2) Periastron Distance (120 au)
- 3) Inclination between disk and perturber star ($0^{\circ} - 180^{\circ}$)
- 4) Orbital Orientation (0°)
- 5) Initial Disk Radius (100 au)

2.1 Numerical Method for Gravitational Stellar Encounters

In this work the gravitational interaction between the two stars and each of the individual dust particles was calculated. In order to achieve this goal, numerical integration methods were employed as to solve the differential equations describing the encounters. In particular, by using the explicit variable order Runge-Kutta (RK) method one is able to solve numerical integration in a more efficient manner. To be more precise, this modified version the Runge-Kutta Cash-Karp method (RKCK) is able to deal with sharp fronts or discontinuous derivatives by computing solutions at several different orders in order to either accept a lower order solution or abort the step. [Cash & Karp, 1990]

RK methods are one of the most popular and widely used formulas for numerical integration for the non-stiff initial value problem. On the downside, one of the most quoted disadvantages is that they require more function evaluations per step than other linear methods. The way RK methods work is by propagating a solution over an interval by combining information from several Euler method steps to then use the obtained information to match a Taylor series expansion to a higher order. [Press et al. as cited in Bhandare, 2015]

$$\frac{dy}{dx} = f(x, y), \quad y(x_0) = y_0$$

One of the features of the RKCK method is the adaptive stepsize control that enables for a more efficient use of the computational resources. In other words, the time steps are more spaced out for circumstances where not a lot of resolution is required while the opposite is true when high resolution is needed. This can be directly translated to when the perturbing star is far away from the host star-disk system and thus the adaptive timestep is larger than when the perturber star is heavily interacting with the system.

The general form of a fifth-order Runge-Kutta formula is the following:

$$k_1 = hf(x_n, y_n)$$

$$k_2 = hf(x_n + c_2 h, y_n + a_{21} k_1)$$

...

$$k_6 = hf(x_n + c_6 h, y_n + a_{61} k_1 + \dots + a_{65} k_5)$$

$$y_{n+1} = y_n + b_1 k_1 + b_2 k_2 + b_3 k_3 + b_4 k_4 + b_5 k_5 + b_6 k_6 + O(h^6)$$

$$y_{n+1}^* = y_n + b_1^*k_1 + b_2^*k_2 + b_3^*k_3 + b_4^*k_4 + b_5^*k_5 + b_6^*k_6 + O(h^6)$$

Therefore the error estimate is:

$$\Delta = y_{n+1} - y_{n+1}^* = \sum_{i=1}^6 (b_i - b_i^*)k_i$$

The RK method treats every step in the sequence of steps in an identical manner, resulting in a more computationally expensive endeavour but that leads to more stable orbits for the particles. The adaptive time step control is used to achieve a predetermined level of accuracy in the solution. The RKCK uses six function evaluations to calculate the fourth and fifth order solutions. In case the error exceeds the level of accuracy previously defined the integration is repeated with a smaller time step. The reduction in the timestep unfortunately leads to accumulation of errors due to the large number of integration steps [Press et al., 2007].

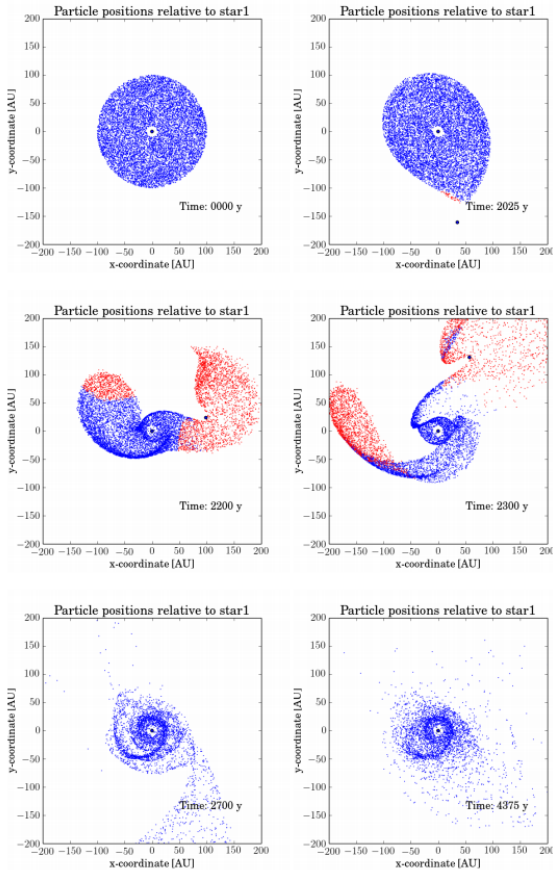


Figure 14: Visualization of time evolution of star-disk interactions $M=1M_\odot$ $r_p=100$ au. In blue are the particles bounded to host star; in red the particles becoming unbounded [Bhandare, 2015]

2.2 Initial Conditions

In this module of the simulation the initial conditions of the disk-star system are first defined. In particular, there are four parameters that are clearly established: 1) Mass of perturber star, 2) Inclination angle for the encounter, 3) Angle of periastron for the encounter and 4) Periastron distance. This procedure generates 7 concentric rings containing each a subset of the total number of particles. This enables the user to sub-divide the problem and make it more manageable. For the purposes of this thesis, the parameter space that was explored consisted of 104 simulations given the different perturber masses, periastron distances and inclinations. From reviewing the available literature, this seems to be the most comprehensive study of the velocities of interstellar objects resulting from disk-star interactions.

The tracer particles have circular Keplerian orbits in the counter-clockwise direction. The initial angular velocity w given the radius r and host mass M is:

$$w = \sqrt{\frac{GM}{r^3}}$$

Using the RKCK method the trajectories of the particles are calculated. An inner hole of 1 au is taken into account as to consider the material that is accreted to the host star and to avoid small time steps. An initial particle constant surface density is assumed, meaning that the number of tracer particles are equally distributed throughout the disk. In a later section, an ad-hoc assumption of the mass surface density of $\Sigma \propto r^{-1}$ is considered as to make an analysis regarding the cumulative mass of the unbounded particles (See Fig. 27). The mass ratio is defined as $M_{21} = \frac{M_2}{M_1}$, where M_1 is the $1M_\odot$ host star while M_2 has a mass between 0.3 and 50. Given that this simulation is trying to replicate the conditions of young clusters, such as the Orion Nebula these values are reasonable. In this scenario massive stars have not gone through their advanced phases of stellar evolution and thus have not lost the majority of their original mass [Pols, 2011]. Scally and Clarke [2000] showed that the separation of stars in a N-body simulated cluster peaked at about 1000 au with a significant proportion of the separations ranging between 100 and 500 au. These distances are consistent with the parameter space proposed in this simulation and with the results. For the low-mass encounters, it was clear that periastron distances of more than 200 au had little to no effect on the disk. On the other hand, high-mass encounters still had a significant influence on the disk even at big periastron distances (See Fig. 19).

2.3 Dynamics

A Fortran executable, which is part of the DESTINY (Database for the Effects of STellar en- counters on dIsks and PlaNetary sYstems) simulation first developed by Breslau et al. [2014] was used to simulate the dynamics amongst the particles. Such executable was independently applied to each of the seven concentric rings for each of the corresponding simulations. Given the computationally expensive procedure of calculating the trajectories for each of the particles it takes a standard machine of 24 cores and 16 GigaBytes of RAM a couple of days to

complete the computation. In contrast, using the resources of the JURECA supercomputer at Forschungszentrum Jülich the computation takes less than 2 hours. This enabled the exploration of the whole parameter space in a way that is both feasible and efficient. In this work the computational resources from both the MPIfR and the Forschungszentrum Jülich were utilized to run the simulations. In all the cases the initial position of the perturber was determined individually for each of the particles. In order to satisfy the condition that the initial influence of the perturber is negligible, the initial distance of the perturber star was chosen so that the force of the perturber star onto the particle was very small relative to the force from the host [Breslau et al., 2017].

$$\frac{F_p}{F_h} < \epsilon = 10^{-4}$$

The maximum initial influence of the perturber star follows:

$$d = r \sqrt{\frac{M_2}{\epsilon}}$$

$$r = \sqrt{x^2 + y^2}$$

It follows that the simulation starts and ends when the epsilon condition of the relative forces is satisfied. At this point the particles are sufficiently unperturbed and the effect on the disk properties is negligible. A condition to stop calculating the trajectory of particles was by deciding if they had settled into a stable orbit. It was decided that they had either remained bounded or unbounded to the host star when the orbital element properties (eccentricity, semi-major axis, argument of periaxis, etc.) did not change more than one percent between two consecutive tests [Breslau et al., 2017]. As described in section 2.1, the numerical integration method utilized in the simulation was the RKCK method. The orbital element properties were calculated using this method. The built-in default maximum relative error of the integrated values of approximately $1.5 \cdot 10^{-8}$ was used.

The basic equation of motion of a planetesimal in a coplanar circular orbit around a host star in the heliocentric reference frame is [Kobayashi & Ida, 2001]:

$$\frac{d^2 r_j}{dt^2} = -\frac{GM_1}{|r_j|^3} r_j + \frac{GM_2}{|R - r_j|^3} (R - r_j) - \frac{GM_2}{|R|^3} R$$

where M_1 and M_2 are the masses of the host and the perturber star, respectively, while r_j and R are the position vectors of the planetesimal j .

2.4 Diagnostics

This last module of the simulation combines the seven disks and generates a folder containing information on different orbital properties defining each of the particles of the simulation. From there, information about the final state (bound or unbound), velocities, eccentricities is

generated. From this final folder all the relevant results are extracted and used for further analysis. It was in this part of the simulation that most of the modifications for this thesis work were done. In previous studies of star-disk encounters only the properties of the bounded particles were studied and the unbounded one were simply disregarded [see Bhandare, 2015]. In contrast, in this case modifications to the code were made as to calculate and save the information of the ejected particles.

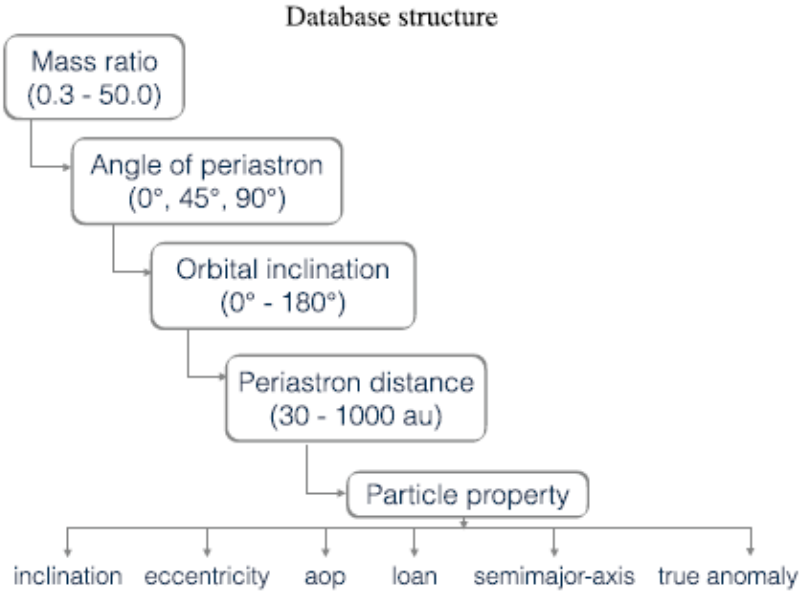


Figure 15: DESTINY database structure tree [Bhandare & Pfalzner, 2019]

After obtaining the final datasets from the simulation it was necessary to clean the data for its final presentation. For instance, in order to calculate the the velocity distribution of the particles becoming unbounded to the host star the velocity magnitude had to be computed from the Cartesian components originally obtained. Also, there was a lot of decision making on how to present the different properties of the particles. For example, the bars (See Fig. 17 and 18) show exactly this kind of decision. In this case, different colors were utilized to represent the different fates of the particles and on the y-axis the normalized value for the percentage of particles corresponding to each of them were shown. To further elaborate this point lets take a look at Fig. 20. The information that is obtained from these series of figures is based on the selection of that parameter space, in particular, on the fraction of particles for each different state as a function of the pertuber mass. These relations are not obvious at first sight but they reveal important information about the particle properties. For the case of the velocity distributions the most important aspect that had to be selected was the bin size. In order to generate meaningful figures there had to be a balance of the ideal bin size that was not big enough to capture all of the data points and not small enough that barely captured individual data points.

3 Results

In this section the results from the parameter study of star-disk gravitational encounters will be presented. The three main diagnostics for the results are 1) the fate (unbounded/bound/accreted) as a function of the different parameters, 2) the dependence of the velocities of the unbounded particles as a function of the different parameters and 3) the cumulative mass of the ejected particles assuming an initial disk mass distribution. The first part of this section investigates exclusively prograde, co-planar encounters and their dependence on a changing perturber mass and periastron distance. The second part illustrates the dependence of the fate and the velocities when the flyby path is inclined relative to the plane of the disc. All the simulations performed in this thesis were greatly based on the DESTINY project, albeit with all the necessary modifications in order to study the fate and velocities of the unbounded particles.

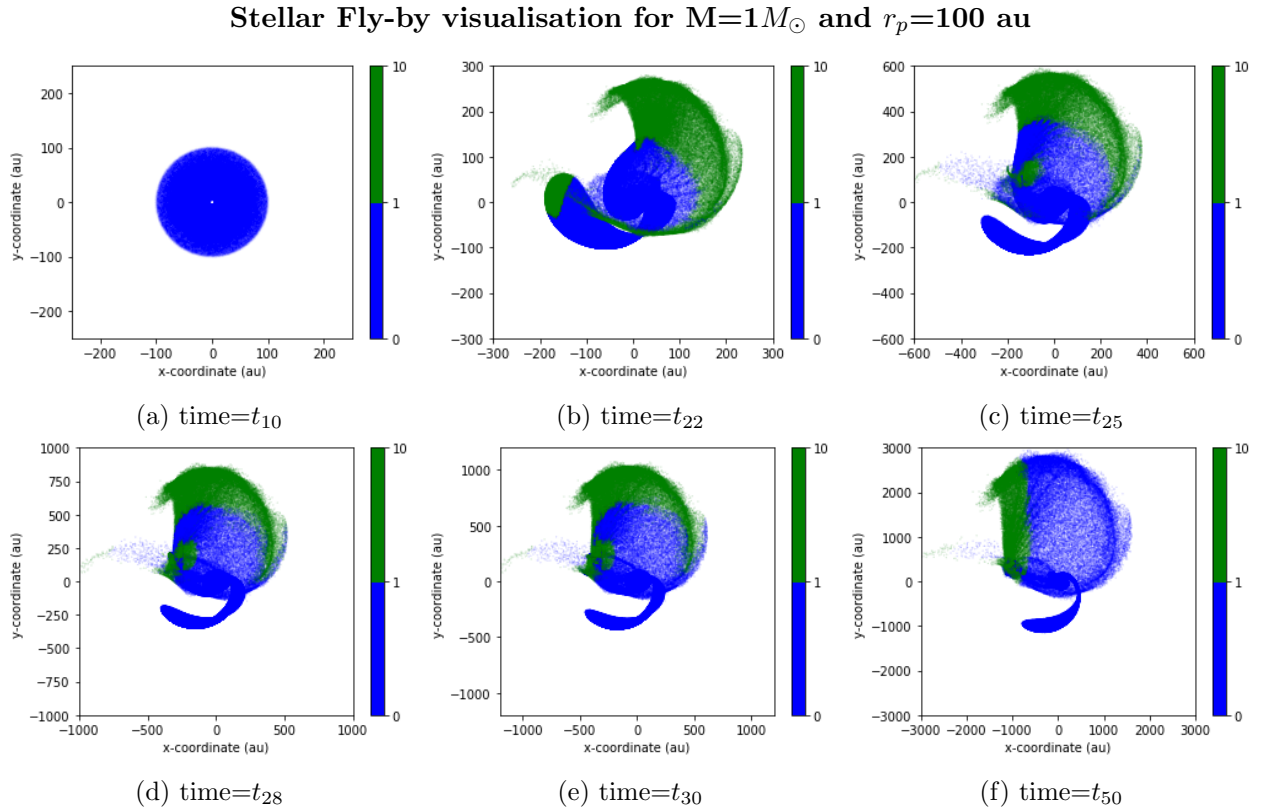


Figure 16: Fly-by visualization for the case of $M=1M_{\odot}$ and $r_p=100$ au for different instances in time during the encounter. In blue the particles with eccentricity less than 1 and thus bounded and in green the particles with eccentricity more than 1 and thus unbounded. Note: The coordinate range is not constant.

A useful guide to understand this process is a visualization of the stellar fly-by and its effect on the disk. In Fig. 16 what is shown is the time evolution of the encounter. From the simulations

an output file with all the relevant properties was generated for every timestep that in this case is approximately 100 years. Also, with the intention of making this figure more intuitive the particles were color coded according to their orbital eccentricity at that moment in time. In this particular example, the particles staying bounded to the host star were set to be blue while the particles becoming unbounded were set to be green. The spiral structures that are produced during the encounter consistent with previous works [e.g. Bhandare, 2015] and with the current understanding of disks either in a protoplanetary scale or a galactic scale.

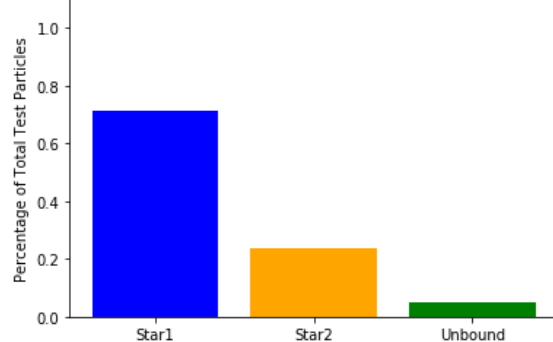
3.1 Varying Mass and Periastron Distance

The final fate of the test particles has a dependence on the pertuber mass and periastron distance of the encounter. The particles were categorized in three distinct groupings: 1) bounded/accreted to the host star, 2) bounded/accreted to the pertuber star and 3) unbounded. They were labeled in the plots as star1, star2 and unbound, respectively. Taking a look at Figures (17 and 18), two patterns emerge that define the ratios of these three categories. First, the initial mass of the perturber star strongly determines the amount of unbounded particles. As one, would expect, with bigger masses the percentage of unbounded test particles increases considerable. For the lower mass case the ratios between star1 and unbound are bigger than one. The opposite case is true for high mass perturbers, this same ratio is less than 0.5 for all the different periastron distance scenarios. Figure. 17 shows the proportion of test particles remaining bound (blue), being captured (yellow) and becoming unbound (green) for the case of the perturber star having a mass $M_p = 1M_\odot$, which means the flyby where the perturber mass equals that of the host star. The case of a periastron distance of $r_p = 160$ au, 120 au, 100 au and 80 au is shown, covering the parameter space from twice the disk size to over grazing the disk to penetrating encounters. Figure. 17 illustrates the general trend that the distant encounters lead to a relatively low portion of test particles becoming unbound, with only 0-5 % becoming unbound whereas closer flybys lead to increasingly more particles becoming unbound. For the example here, 5% of test particles become unbound for the flyby at 160 au compared to 50% at 80 AU. Perhaps surprisingly, for the more distant encounters more test particles become actually captured by the perturber star than become unbound. Only for encounters closer than 120 au this trend is reversed. This trend can be appreciated in the Appendix for Figures (38, 39, 40, 41, 42, 43, 44, 45). One of the limitations of this diagnostic is that it does not indicate the mass and initial position of the particle in the disk for each of the three categories. The series of figures located in the appendix expand on the information about this physical process. For example, for the case $M=0.3M_\odot$ and $M=0.5M_\odot$ no matter how close the encounter, the total fraction of particles remaining bounded to the host star was always bigger than their counterparts. This trend changed for all the cases with mass bigger than $M=0.75M_\odot$, with most of the particles becoming unbound for masses bigger than $M=5M_\odot$.

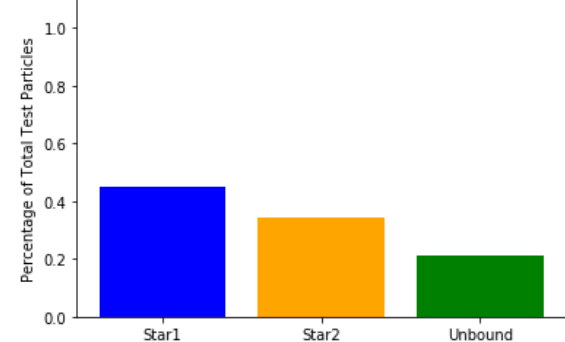
One important property of the aforementioned figures that needs to be addressed is the error inherent in them. The ideal way to calculate this would have been to utilize different random seeds for a statistically significant set of simulations. From there, the error of the percentages of particles could have been accurately (See Fig. 19). Instead what was done, was to assume a

three percent standard deviation for each of the measurements. In the future, any diagnostics presenting information in a barred format must include error bars.

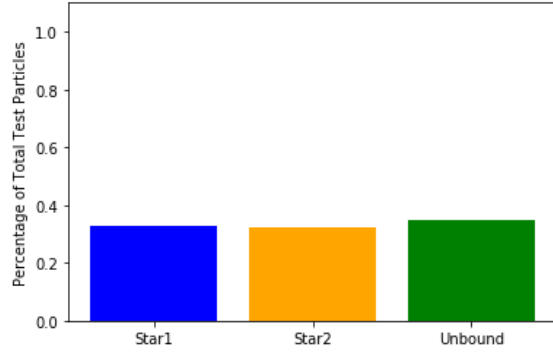
Percentage of Particles by Type for $M=1M_{\odot}$ for Different Periastron Distances



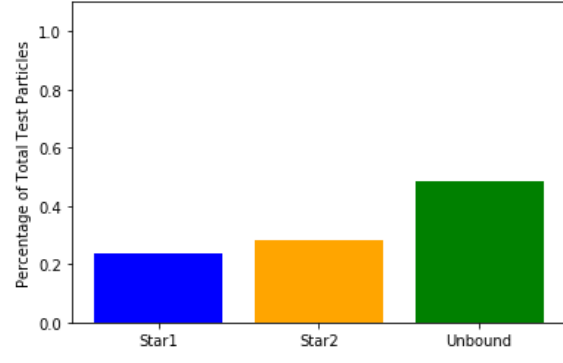
(a) $r_p = 160au$



(b) $r_p = 120au$



(c) $r_p = 100au$



(d) $r_p = 80au$

Figure 17: Percentage of test particles remaining bounded to the host star, captured by the perturber star or becoming unbounded from the disk for $M=1M_{\odot}$ with changing periastron distance.

Percentage of Particles by Type for $M=10M_{\odot}$ for Different Periastron Distances

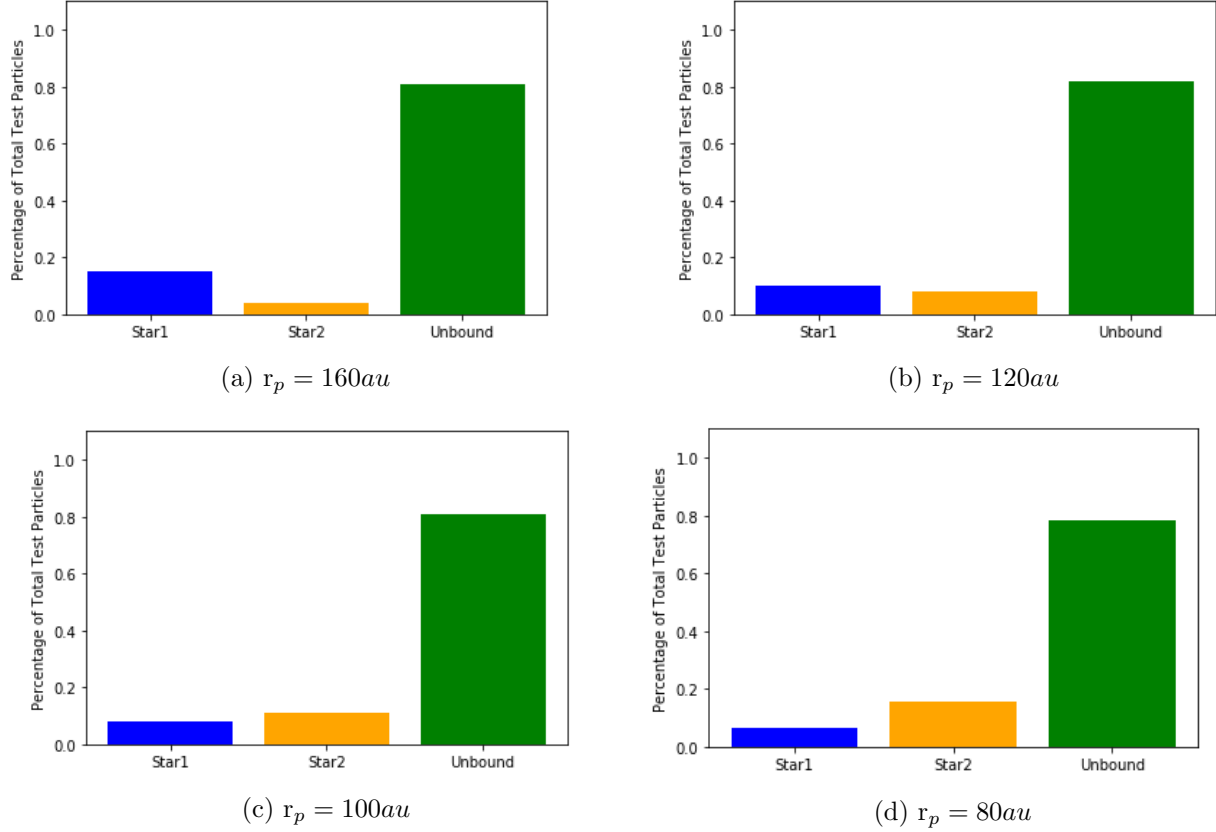


Figure 18: Percentage of test particles remaining bounded to the host star, captured by the perturber star or becoming unbounded from the disk for $M=10M_{\odot}$ with changing periastron distance.

The other property that is worth commenting on is the dependence of the percentage of unbound particles as a function of the periastron distances. This can be clearly appreciated in Figure 19. The fitting for the selected cases are included in the figure. The analytical description of such curves are also presented just below. For the higher mass curves of $M=50M_{\odot}$, $10M_{\odot}$ and even $5M_{\odot}$ have a negative curvature. This is the contrary for the $M=0.5M_{\odot}$, $1M_{\odot}$ and $2M_{\odot}$ cases. This figure indicates two things. First, that the maximum number of unbounded particles are always the result of the closest encounter. Meanwhile for the distant encounters they smoothly decreases up until they reach a minimum value. Second, the curvature of the fitting lines showcase how the higher mass encounters producing unbounded planetesimals have a more destructive effect. A useful way to visualize this would be to imagine that the curvature of the $M=10M_{\odot}$ fitting was positive. In that case the effect on the disk would be of less destruction and more planetesimals remaining bounded as a function of periastron distance.

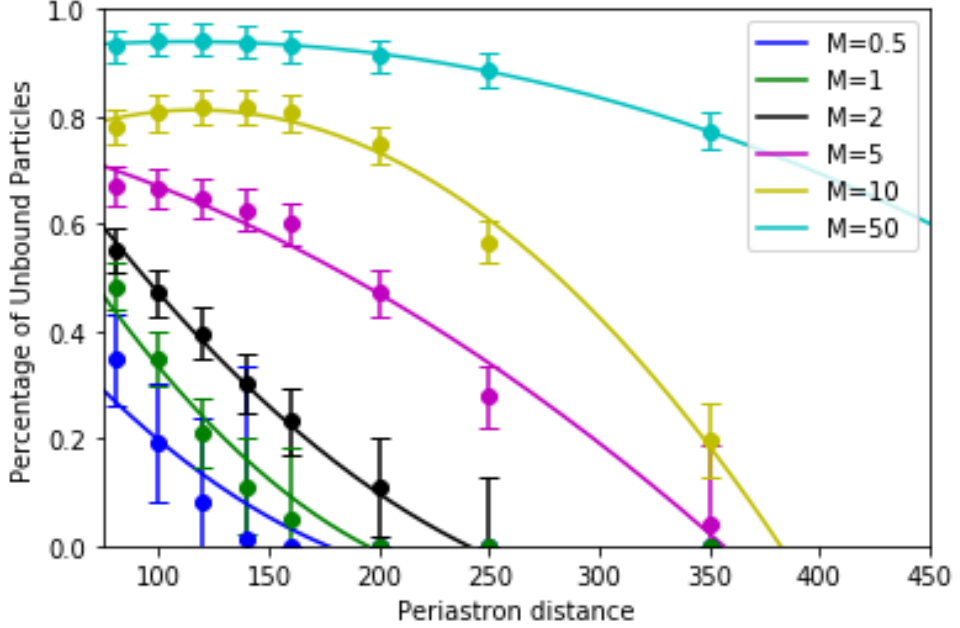


Figure 19: Percentage of unbounded particles for the co-planar prograde case as a function of periastron distance for different masses.

$$\begin{aligned}
 & 1.095 * 10^{-5}x^2 - 0.005x + 0.647, & M = 0.5 \\
 & 1.474 * 10^{-5}x^2 - 0.007x + 0.972, & M = 1 \\
 & 9.443 * 10^{-5}x^2 - 0.006x + 1.033, & M = 2 \\
 & -3.916 * 10^{-6}x^2 - 0.001x + 0.792, & M = 5 \\
 & -1.152 * 10^{-5}x^2 + 0.002x + 0.655, & M = 10 \\
 & -2.986 * 10^{-6}x^2 + 0.001x + 0.901, & M = 50
 \end{aligned}$$

The next set of results, show the dependence of the final fate of test particles as a function of the mass. What is shown in Fig. 20 are the different snapshots for the distinct periastron distances. It can be seen that the curve for the unbounded particles in this parameter space becomes steeper with increasing periastron distances. This can be summarized more precisely in Fig. 22 where the curves are all presented together. It is worth noting that the curvature of the line corresponding to periastron of 80 au is different than the rest of the lines. It seems to be due to the fact that the encounter goes through the disk and therefore has a more destructive effect than their distant counterparts.

Percentage of Particles by Type vs Perturber Mass

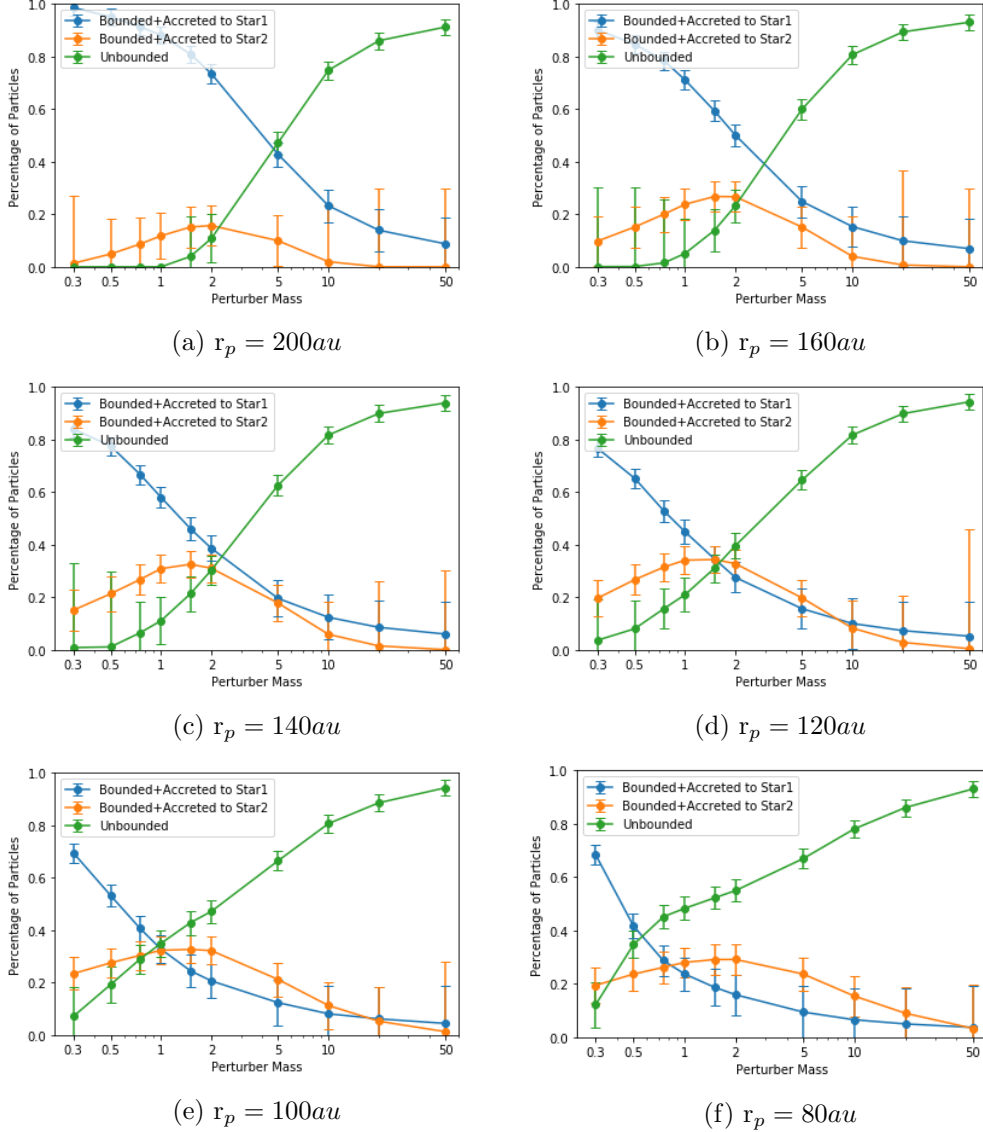
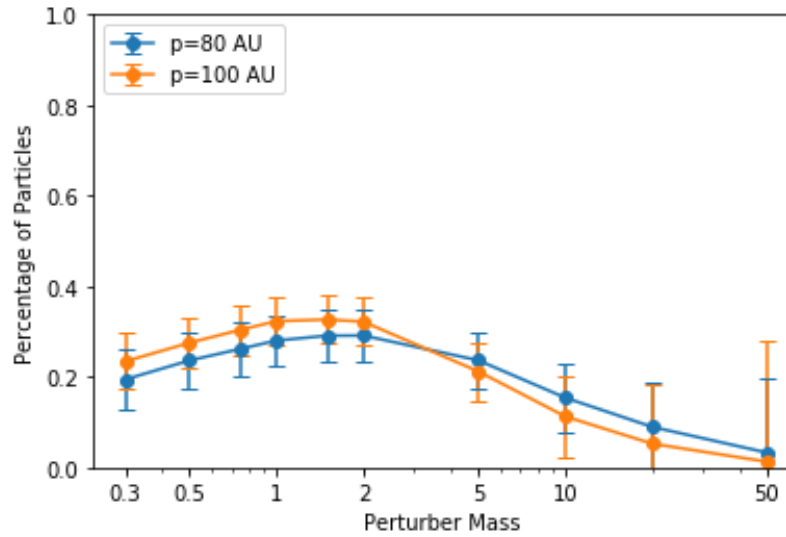


Figure 20: Percentage of test particles remaining bounded to the host star, captured by the perturber star or becoming unbounded from the disk as a function of perturber mass for different periastron distances.

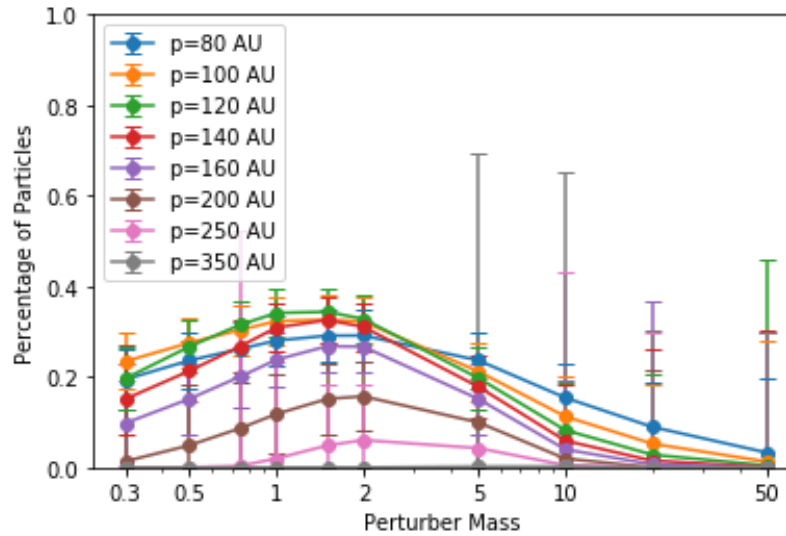
Furthermore, Figure 21 shows the summarized curves for the particles that end up being bounded or accreted to the perturber star. The way the error was calculated for these set of plots follow the same logic as described before. Namely, the standard deviation divided by the square root of the number of particles. A standard deviation of 0.03 was assumed for all the data points. This was done as a substitute for repeating the simulations multiple times using different random seeds. Given the amount of computational resources needed to run each

simulation, performing them a large number of times for the purposes to precisely calculate the standard deviation of the percentage of particles was not feasible.

Percentage of Test Particles Bounded/Accreted to Perturber Star



(a) Close Encounters



(b) All Encounters

Figure 21: Percentage of test particles becoming bounded/accreted to the perturber star as a function of mass for different periastron distances.

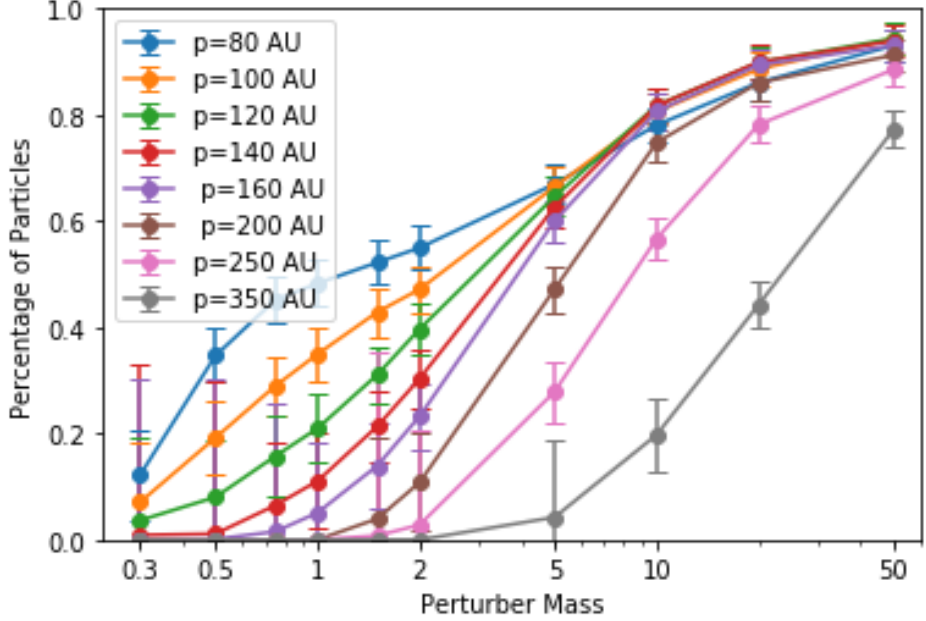


Figure 22: Percentage of test particles becoming unbounded from the disk as a function of mass for different periastron distances.

Figures 23 and 24 show the different velocity distributions for the cases of $M=1M_{\odot}$ and $M=10M_{\odot}$ for the different periastron distances. They show two things: first, the range of possible velocities for the different conditions as well as the percentage of particles becoming unbounded from each encounter. Both properties reveal a full picture of how these systems behave. Now, let's dive into a more detailed description of these particular figures. If one looks carefully at the velocity magnitude range for the lower masses the values fall between 0.2 km/s and 1.0 km/s. This is true up to $M=1M_{\odot}$ but changes as the perturber mass is increased. For instance, the figures from $M=1.5M_{\odot}$ and onwards (See Appendix) the velocity magnitude range evolves progressively to values between 0.2 km/s and 3.0 km/s. As one could expect, as the perturber mass increases and the periastron distances decreases the total number of unbounded particles increases. The overall shapes of the distributions also change with changing masses and periastron distances. One particular feature that emerges at $M=5M_{\odot}$ and beyond is that of a double peak. This interesting characteristic probably emerges because of the orbital resonances in the system. Similar to what happens in the asteroid belt in the solar system, in which there are Kirkwood gaps where orbits are destabilized by resonances and small bodies cannot orbit at that specific orbital location. Planetesimals in our simulations behave similarly, such that these objects cannot have specific velocities and thus an apparent gap appears in the velocity distribution.

Velocity Distribution of Unbounded Particles for $M=1M_{\odot}$ and Different Periastron Distances

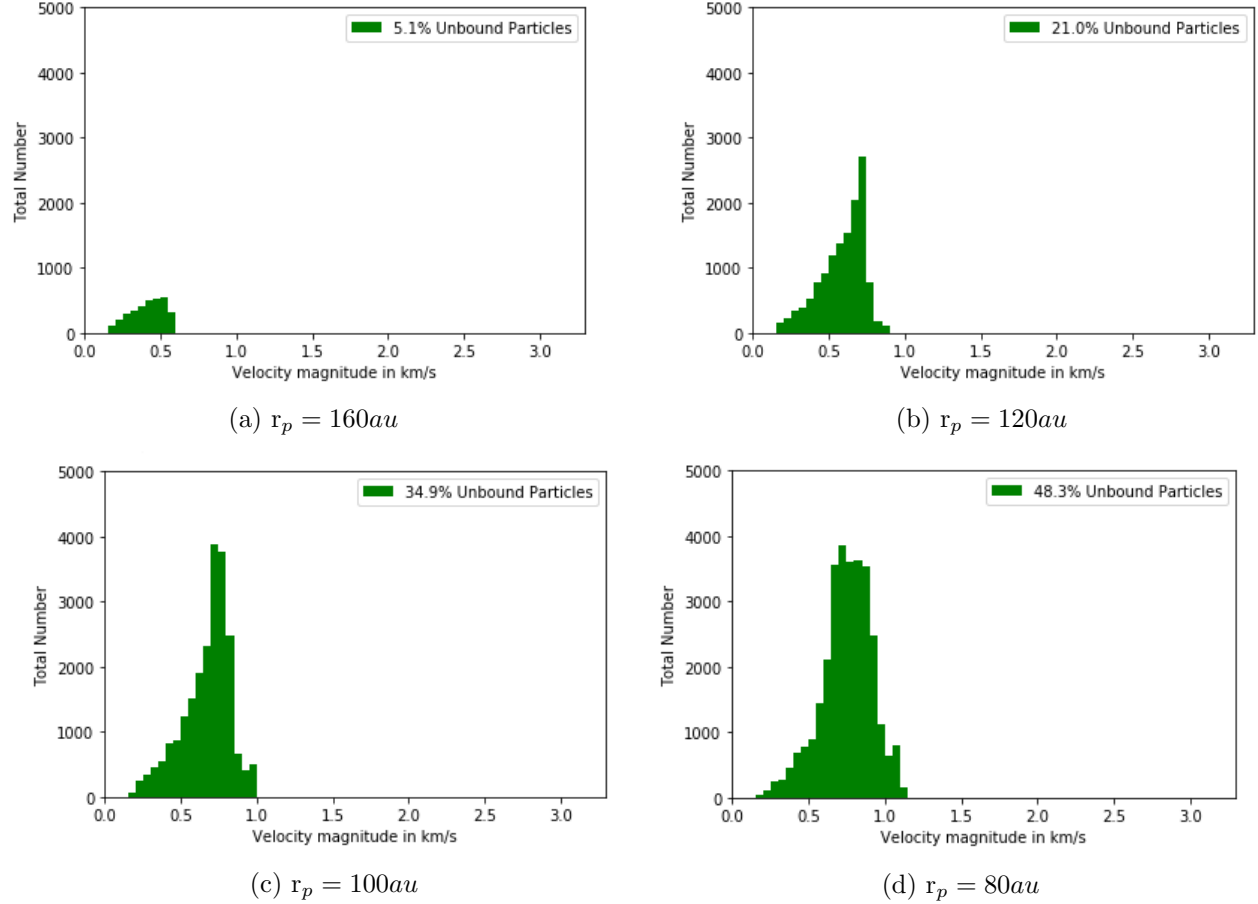


Figure 23: Velocity distribution of unbounded test particles for $M=1M_{\odot}$ and different periastron distances.

Velocity Distribution of Unbounded Particles for $M=10M_{\odot}$ and Different Periastron Distances

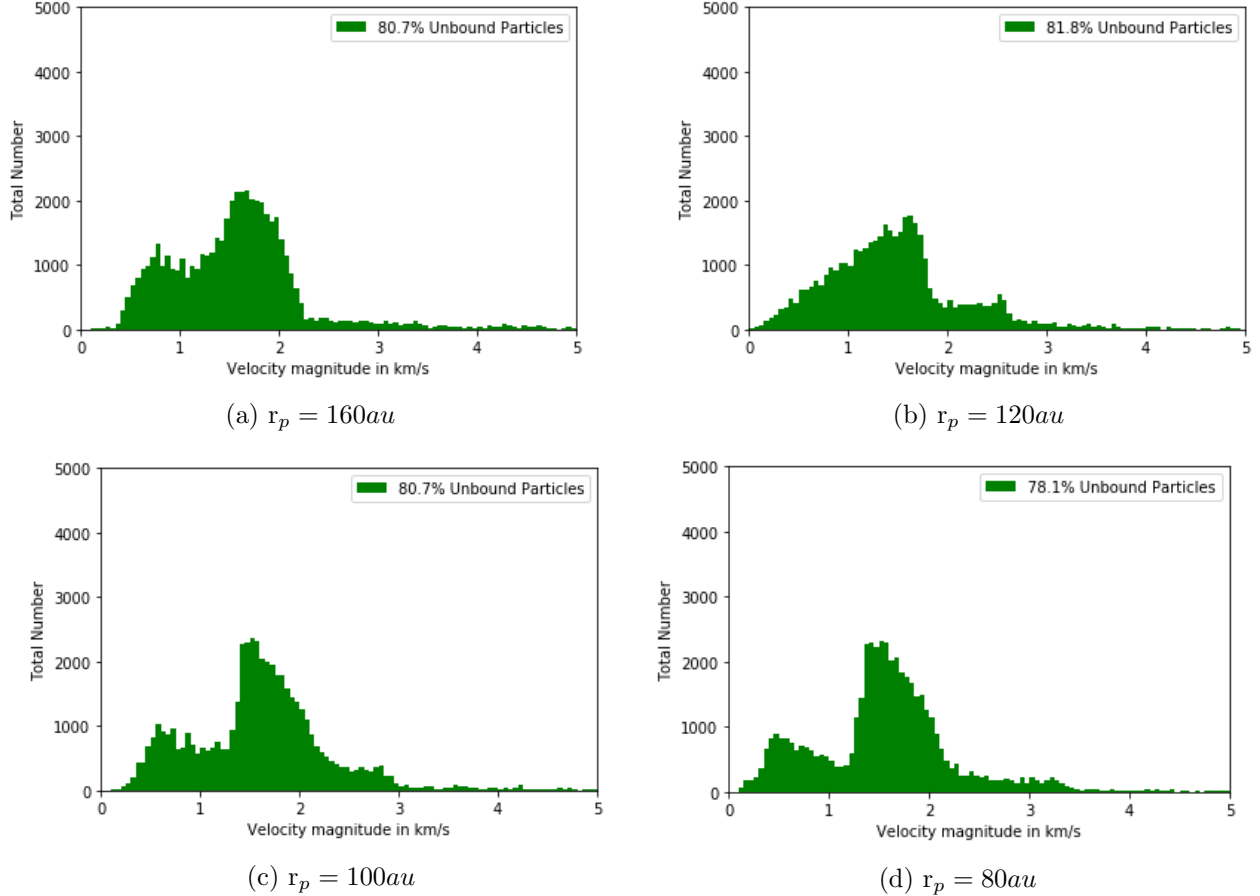


Figure 24: Velocity distribution of unbounded test particles for $M=10M_{\odot}$ and different periastron distances.

Furthermore, Figures 25 and 26 show the mean velocity for the distribution as a function of the periastron distance and the mass, respectively. For Figure 25, a subset of the the mass was considered for the purposes of a clear illustration of the general trend that is occurring. Namely, the mean velocity of the unbounded particles is not a function of the periastron distance but it is of the perturber mass. For this reason the curves in 25 are almost flat. Likewise the mean velocity is higher for bigger masses. Figure 26 shows the mean velocity of the unbounded particles as a function of mass. It appears to be a proportional relationship between these two quantities except for the range between $0.3M_{\odot}$ and $1M_{\odot}$. The error bars included in these plots correspond to the definition of the standard error, where σ is the standard deviation of the velocity distribution and N the number of test particles.

$$\delta = \frac{\sigma}{\sqrt{N}}$$

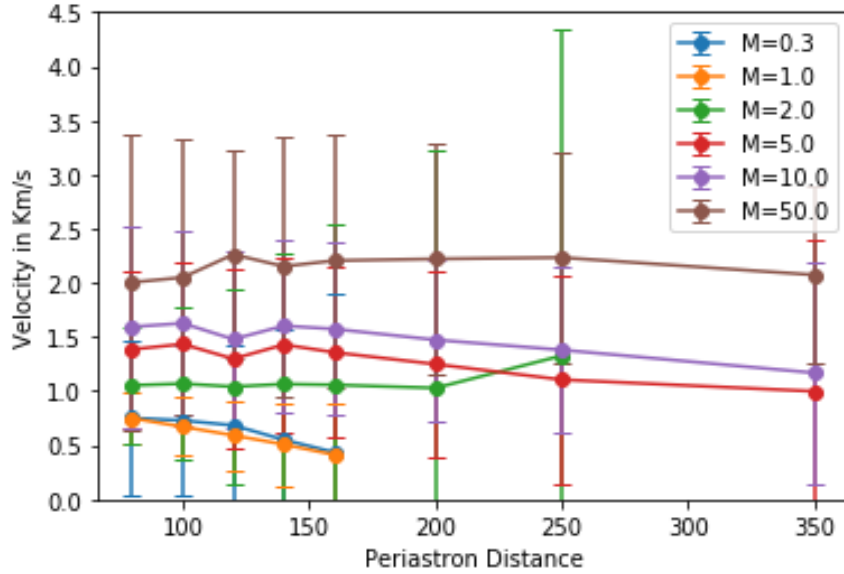


Figure 25: Mean velocity of unbounded test particles as a function of periastron distances for a subset of perturber masses

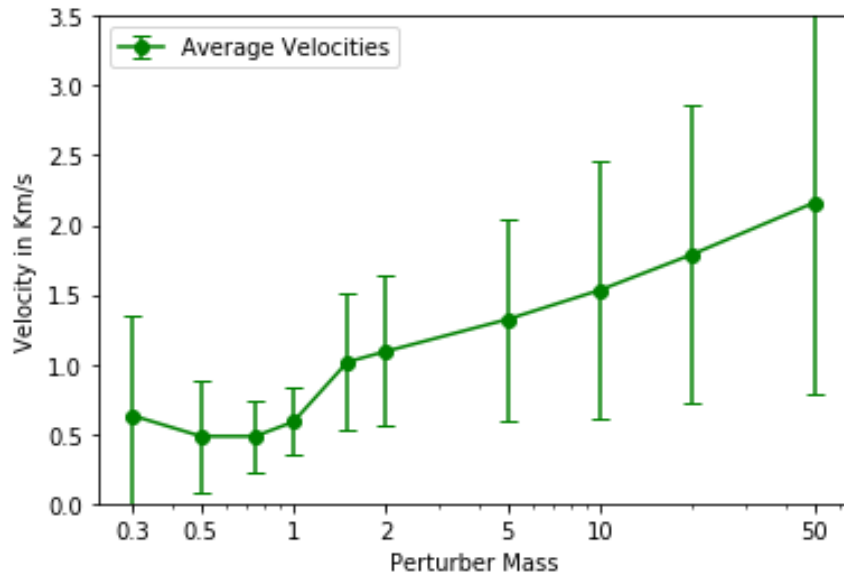


Figure 26: Average Velocity of Unbounded Particles vs Perturber Mass

Next in the results, what is shown is the mass distribution of the disk. This was based on the assumption that the mass of within the disk follows a $1/R$ distribution. In other words, there

is considerably more mass in the closest regions of the disk than at the outskirts. Figure 27 was constructed based on three assumptions: 1) there are 50 concentric rings conforming the disk, 2) the mass distribution follows $1/R$ and 3) the total mass of the disk corresponds to 0.01 solar masses. The equations that follow correspond to the analytical description of the disk. For this it was important to consider the correct dimensionality of the density as to achieve the desired mass distribution. The goal of all of this is to measure how the cumulative mass of the unbounded particles evolve as a function of the simulation parameters. The way this is performed is through the following reasoning. First, after running the simulations one is able to obtain a huge list with the different final fates of the particles. From the distribution one already knows the mass of each of the 50 slices of the disk. Knowing the initial radius of such particles we can associate them to a specific mass obtained from such slices. For the purposes of this analysis, a scaled mass distribution was performed. This means that it is assumed that particles that are located near the center of the disk are more abundant than the particles in the outskirts. So you have a combination of two different effects, near the center of the disks particles are both more abundant and more massive. Figure 28 and 29 show how the cumulative mass of the scaled unbounded particles change as a function of periastron distance and perturber mass.

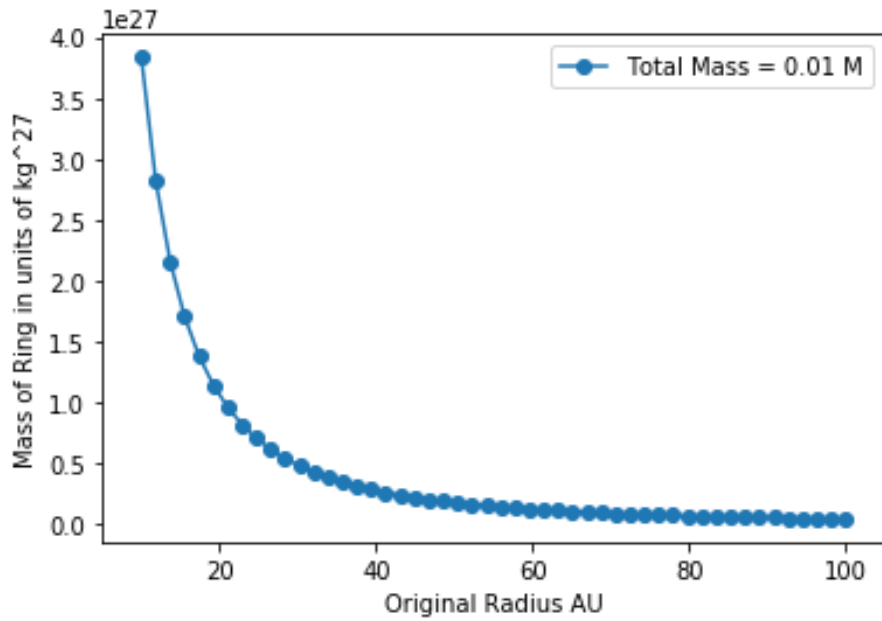


Figure 27: Initial mass distribution of concentric rings making up the disk.

$$M = 2\pi \int_{R_{High}}^{R_{Low}} r\sigma(r)dr \quad (1)$$

$$\sigma(r) = \sigma_0 \frac{1}{r^3} \quad (2)$$

Substituting (2) in (1)

$$\begin{aligned}
M &= 2\pi \int_{R_{High}}^{R_{Low}} \frac{\sigma_0}{r^2} dr \\
M &= \frac{-2\pi\sigma_0}{r} \Big|_{R_{High}}^{R_{Low}} \\
M &= -2\pi\sigma_0 \left[\frac{1}{r_{High}} - \frac{1}{r_{Low}} \right] \\
M_{total} &= -2\pi\sigma_0 \left[\frac{1}{r_{50}} - \frac{1}{r_1} \right] \\
\sigma_0 &= \frac{M_{total}}{-2\pi \left[\frac{1}{r_{50}} - \frac{1}{r_1} \right]} \\
S_i &= -2\pi\sigma_0 \left[\frac{1}{r_{i+1}} - \frac{1}{r_i} \right]
\end{aligned}$$

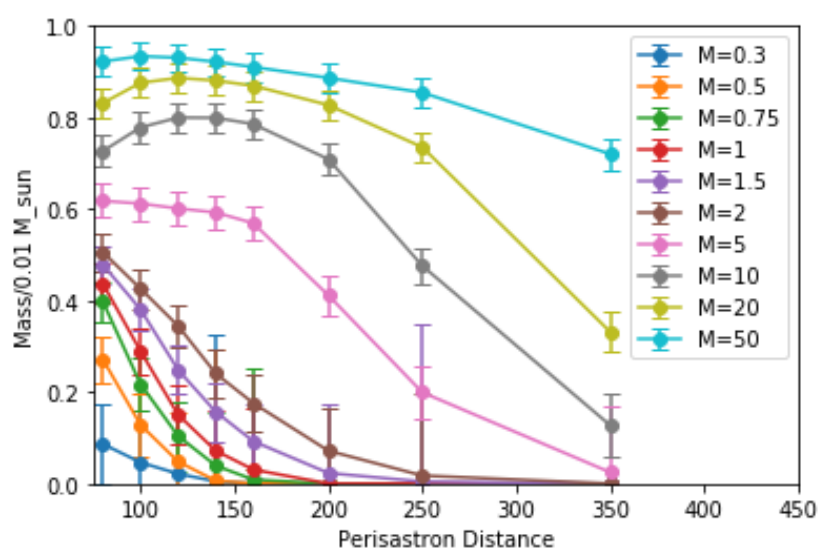


Figure 28: Cumulative mass of unbounded test particles as a function of periastron distance for different values of perturber mass.

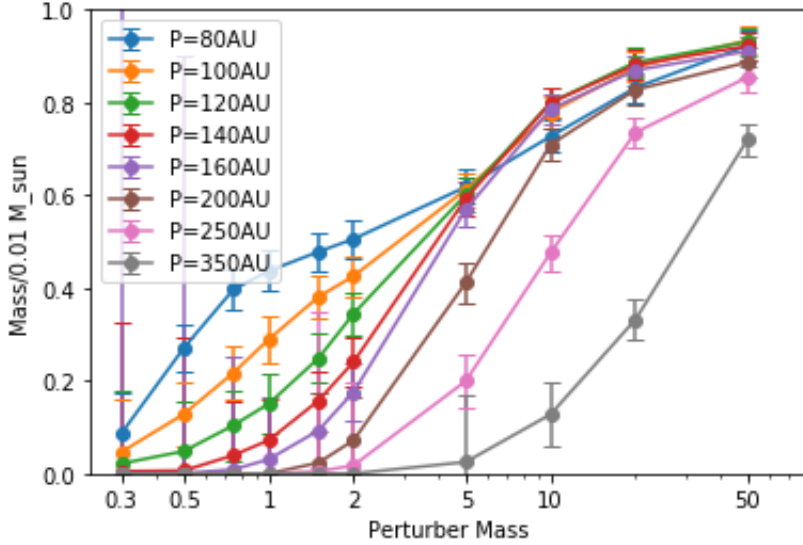


Figure 29: Cumulative mass of unbounded test particles as a function of pertuber mass for different periastron distances.

3.2 Varying Inclination

Turning now to the second part of the results, whose goal is to look at how the properties of the encounters depend on the inclination, we repeat some of the diagnostics previously presented. First, there are the percentage bars for the first case of $M=1M_{\odot}$ (see Fig. 30), the percentage of particles remaining bounded to the host star increases as a function of the inclination. For the second case of $M=10M_{\odot}$, the same pattern is present with a very sharp decrease in the number of particles bounded/accreted by the perturber star (See Fig. 54). A particular feature that is present in these two figures is considerable decrease of the particles accreted to the perturber star for inclinations above 85° .

The second part corresponds to the velocity distributions of the unbounded particles. The first thing to notice in Figure. 31 is that the velocity range moves leftward (decreasing) with increasing inclination. The velocity range of the co-planar case lies between 0.2 and 0.9 km/s, with a peak at around 0.7 km/s. Not only, the peak moves to a lower velocity but also the total number of particles decrease as a function of inclination. This is more noticeable, in Figure. 55 where the transition between $i=90^{\circ}$ and $i=120^{\circ}$ shows a dramatic drop in the total number of unbounded particles as well as a narrower range of velocities. Figure. 33 shows how the mean velocity of the distribution evolves as a function of inclination. Two things can be appreciated from this plot: 1) the error bar for $i=120^{\circ}$ is significantly bigger due to the small number of test particles becoming unbound at this inclination and 2) the symmetric properties of disk-star encounter. It is easy to see how the inclination would complete a full rotation after 360° . There would therefore be a minimum value for the mean velocity at 150° and 210° .

Percentage of Particles by Type for $M=1M_{\odot}$ for Different Inclinations

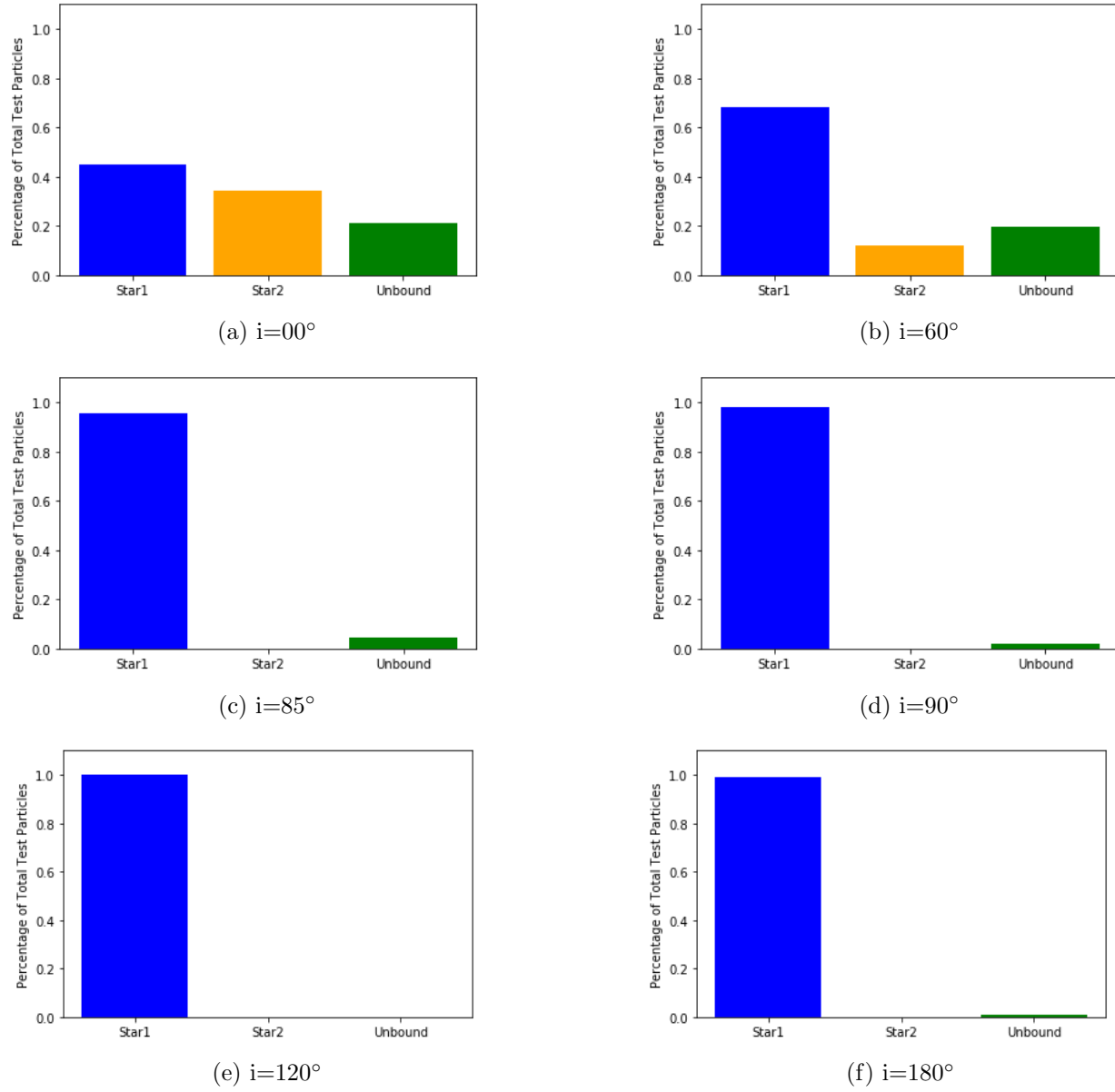


Figure 30: Percentage of test particles remaining bounded to the host star, captured by the perturber star or becoming unbounded from the disk for $M=1M_{\odot}$ with changing inclination.

Velocity Distribution of Unbounded Particles for $M=1M_{\odot}$ and Different Inclinations

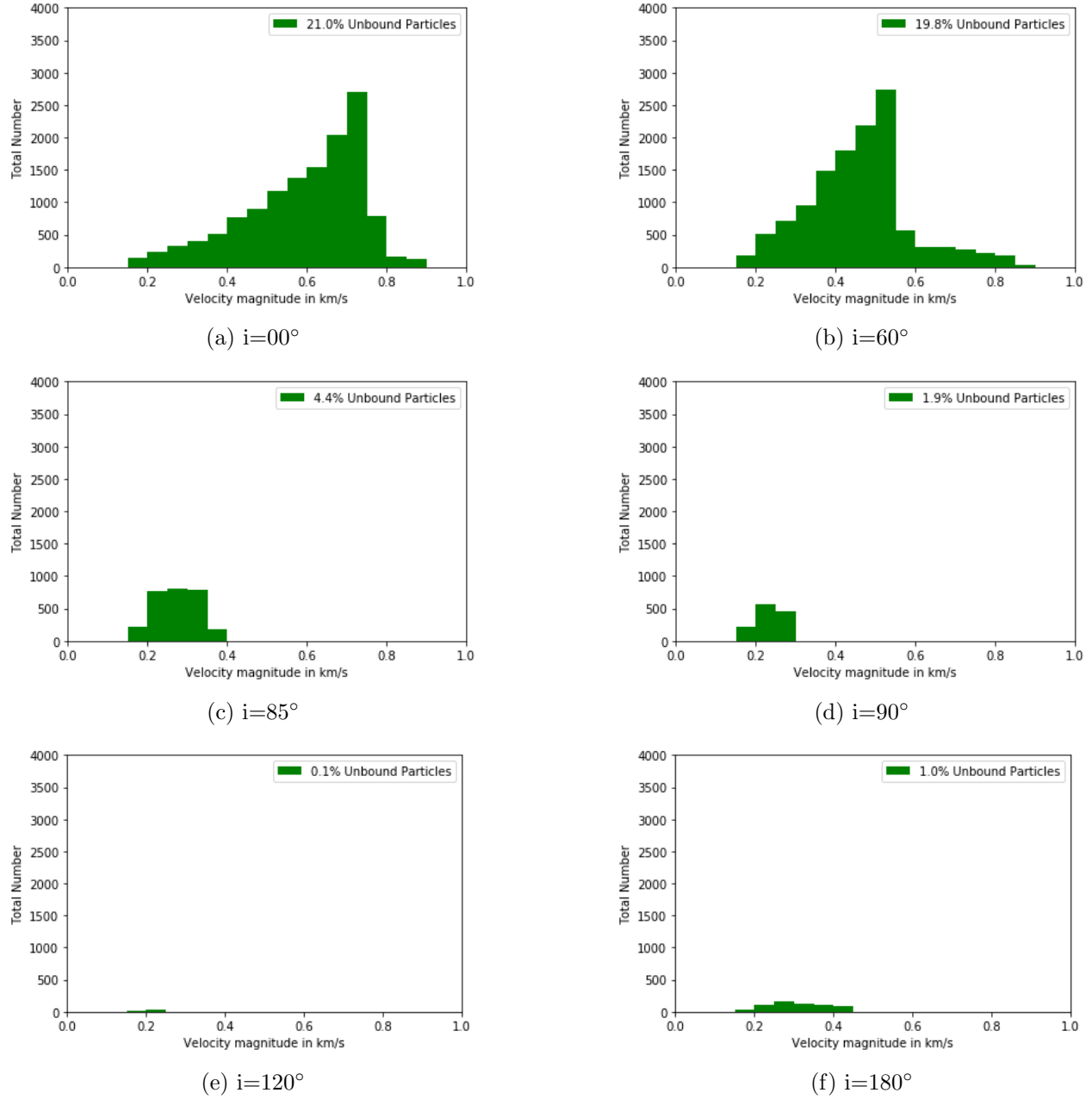


Figure 31: Velocity distribution of test particles for the case of $M=1M_{\odot}$ and changing inclinations

Also, following the same assumptions for the mass distribution described in the first part of the results, the cumulative mass of the unbounded particles as a function of inclination was calculated for the two different perturber masses. From Figure. 57 it can be observed that there is a sharp decrease in the mass at exactly the range of $i=90^{\circ}$ and $i=120^{\circ}$. This follows from

the percentage of unbounded particles as a function of the inclination (Figure. 32). It is not a coincidence that there is a very tight correlation between these two figures given that it follows that the cumulative mass of the ejected particles is almost proportional to the total number of unbounded objects.

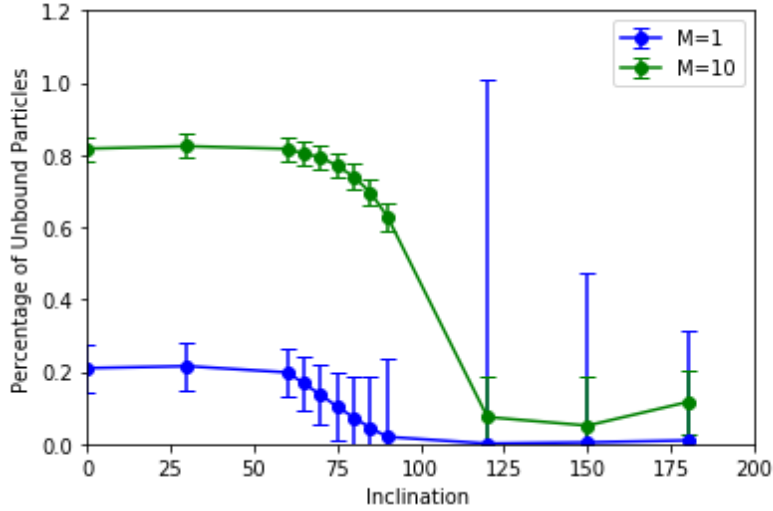


Figure 32: Percentage of Unbounded Particles for $1M_{\odot}$ and $10M_{\odot}$ as a function of encounter inclination.

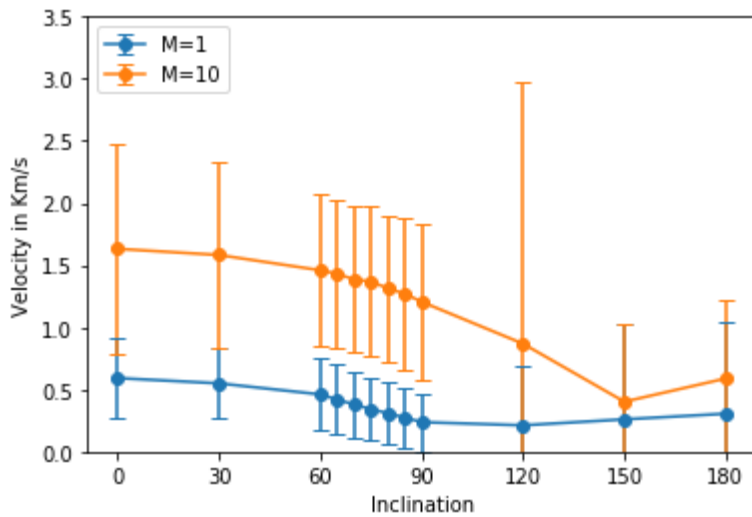


Figure 33: Mean Velocities for different encounter inclinations for perturber masses $M=1M_{\odot}$ and $M=10M_{\odot}$.

For the case of varying angle of periastron the mean velocity of the unbounded particles didn't change (Figure. 34). This is because the symmetrical properties of a circular disk. It is worth considering that a combination of a non-zero inclination and a varying angle of periastron might result in changing mean velocities.

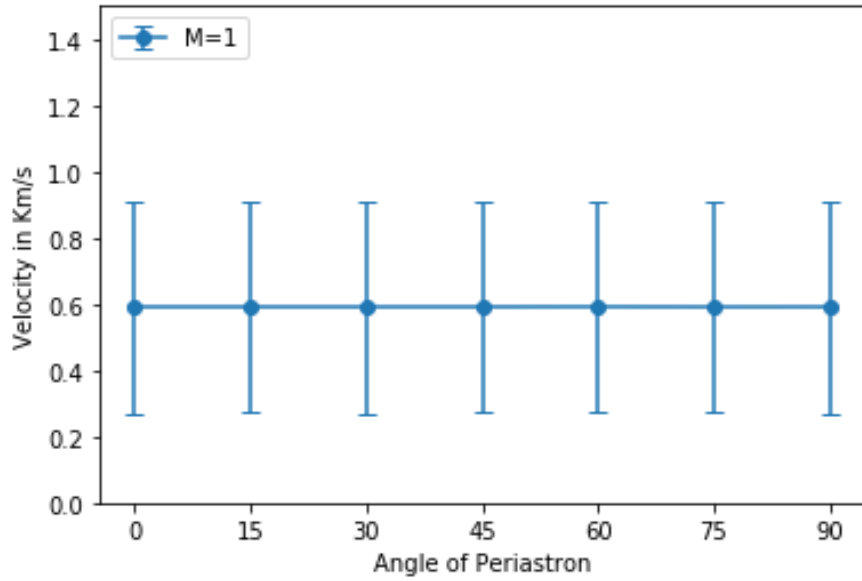


Figure 34: Mean Velocities for different w ; $M=1 M_{\odot}$ $p=120$ au $i=0^\circ$

4 Discussion

4.1 Limitations of our Model

In order to study the properties of star-disk interactions several assumptions had to be made. The first one is that the simulation does not take into account the viscosity within the disk. This was due to two factors: 1) we are dealing with low mass disks and 2) they are virtually gas-free. The range of masses for protoplanetary disks is between $0.02M_{\odot}$ and $0.1M_{\odot}$ [Williams & Cieza, 2011]. Here we are interested in relatively large planetesimals, these need to grow. Therefore, we are concerned with the stages where gas content is low or even completely absent. Given the fact that the total mass of the disk is quite minuscule, it can be justified that the viscosity is neglected. This entails that the calculations becomes significantly more simple as it turns the problem from an N-body problem to a restricted three-body problem. In the case of more massive disks ($M_d > 0.1M_{\odot}$) the effects of self-gravity and viscosity become non-negligible.

Second, it was assumed that only one of the stars had an orbiting disk around it while the other one did not. In reality, as one might expect, it would be quite common that both of the stars had orbiting material around them. This would open up more questions about the ultimate fate of the particles of the perturber star. Assuming that the particles of the two discs rarely influence each other, the results presented here can also be used to determine the number of particles released in the perturber disk. The reason is that the results can be used not only for the case of the central star being of one solar mass but the entire simulation scales as the ratio of the mass of the central star to that of the perturber star. This means that the scaling could in principle enable us to study how different encounters behave when the mass ratio does not assume the host star's mass to be equal to unity.

Third, another limitation of our results is the fact that the errors corresponding to the different percentages for the three distinct categories (star1, star2, unbounded) were not calculated in detail. The correct way to proceed would be to perform the simulation many times using different random seeds as to estimate the standard error of each of the cases. In this work what was assumed was a default three percent value for the standard deviation for all of the cases that dealt with these categories. This number was comparable to the typical error of three percent found in Olczak et.al [2006] for the encounter triggered mass loss in protoplanetary disks. This is justified, because in principle it is the same type of simulation, so that the errors can be expected to be the same. Another limitation, that has more to do with the process rather than the program itself is the lack of scalability. The way the modules are built requires the user to run the executable file for each of the concentric rings, making the process quite lengthy. In a future improved version of the code it would be ideal if this process is automated. This would allow the user to explore a wider parameter space within the same amount of time. Another idealization that was considered for our simulations was the assumption that all the disks start as a flat thin disk and not a flared ones. This means that all the particles are initially distributed in a tight manner along the radius of the disk. We also did not consider planetesimal growth through dust coagulation happening at different snowlines. The growth of

particles when agglomerating with other particles could help to understand how ISO's such as Oumuamua and Borisov might have acquired their mass.

4.2 Comparison with Previous Work

As it has been mentioned before, a lot of what has been investigated in this work is a natural extension on what Bresalu et al. [2017] and Bhandare [2015] have studied. These studies in turn were built upon earlier research such as Larwood & Kalas [2000], in which they studied dynamics of stellar encounters on a symmetrical planetesimal disk. Their goal was to understand and replicate the substructures and asymmetries observed in the Beta Pic disk. The code used to perform the simulation was greatly based on the one used by Bresalu et al. [2017] and Bhandare [2015]. However, what is fundamentally different is the focus on the matter that becomes unbound and thereafter floats as ISOs through interstellar space. The results obtained in the work, and in particular, the particle fate and velocities of the unbounded particles can be compared to previous work done in this field. The main goal of all of this is to understand the underlying mechanisms that give rise to ISOs. Several papers have been published containing information on the velocities of the unbounded planetesimals originating from different mechanisms. A brief summary of those findings will be presented here as well as a discussion on the implications of such findings.

First, the velocity distributions that were obtained from our simulations reveal a very interesting similarity with the results published by Hands et al. [2019]. In this study they looked into the velocity distribution for unbound particles ejected from specific cluster environments. In other words, these values reflect the velocities of the ISOs with respect to the Local Standard of Rest of the Milky Way rather than from the host star. Is for this reason that the distributions presented in this thesis work present a more reliable way to analyze disk-star encounters due to the fact that they don't depend on external circumstances such as the nature of the motion of the cluster itself. Furthermore, the methodology Hands et al. relied on was an N-body simulation of the early phases of open cluster evolution rather than a restricted 3-body gravitational simulation. Compared to the results from this thesis work, the velocity range for the unbounded planetesimals overlapped very tightly with Hands' results. Namely, most particles are located in the range of velocities between 0 and 5 km/s. The only exception to this was the *IC348₁* model which, as the authors suggested, was an anomalous distribution and not a norm amongst the vast majority of the other cases. Furthermore, the "double peak" feature that can be observed in Fig. 35 is also present in Fig. 24 and in Fig. 51- 53 (See Appendix).

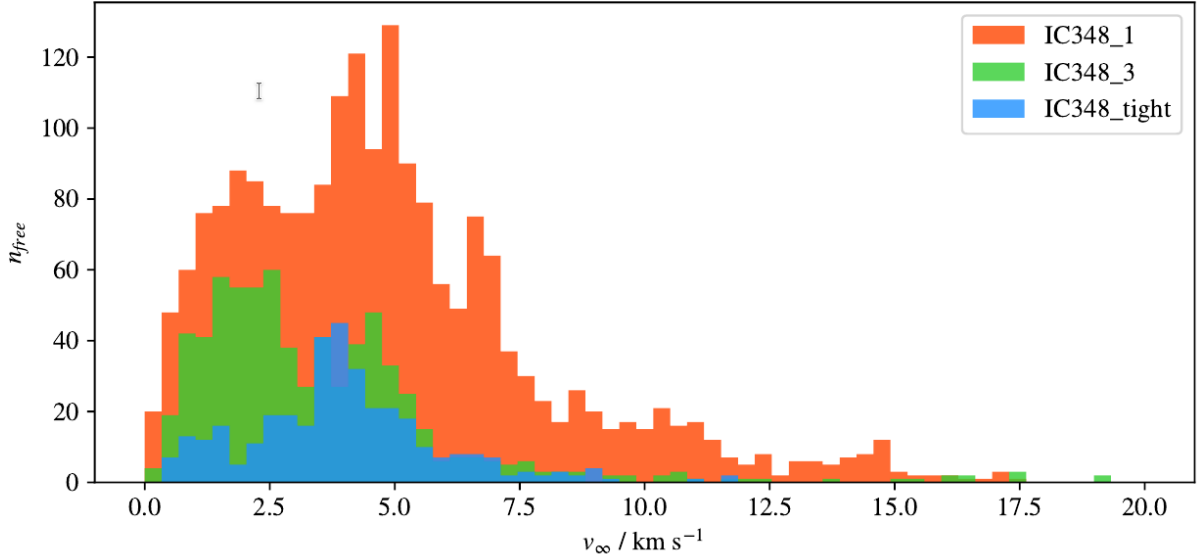


Figure 35: Distribution of hyperbolic excess velocities for planetesimals ejected from IC348 models after 10 Myr for the N-body cluster evolution simulations [Hands et al., 2019]

Second, the gravitational interaction between the disk and giant planets stands as an independent mechanism for the production of ISOs. In a wide study of lithopanspermia, the idea that biological material is spread from one solar system to another in star forming groups, Adams and Spergel [2005] dedicated a small subsection of their study to see how giant planets scatter planetesimals. The velocities of planetesimals removed from their host planetary system due to their gravitational interaction are shown in Fig. 36. It can be appreciated that the velocity range for these objects lie between 5 and 10 km/s, indistinguishably bigger than the protoplanetary disk-star encounter cases. It can be appreciated in this figure that there are different types of curves each representing a different distribution of particle velocities. In this case the solid curve represents the particle distribution due to the ejection of planetesimals on a Jupiter-crossing orbits. Second, the dashed curve shows the ejection speeds on Neptune-crossing orbits. Thirdly, the dotted curve shows the distribution of ejection speeds when there is a stellar companion with a mass of $0.1M_{\odot}$ and a semi-major axis of 42 au. This semi-major axis is taken from the peak of the distribution of stellar separations for binary systems in clusters. In all these three cases the distributions have been normalized.

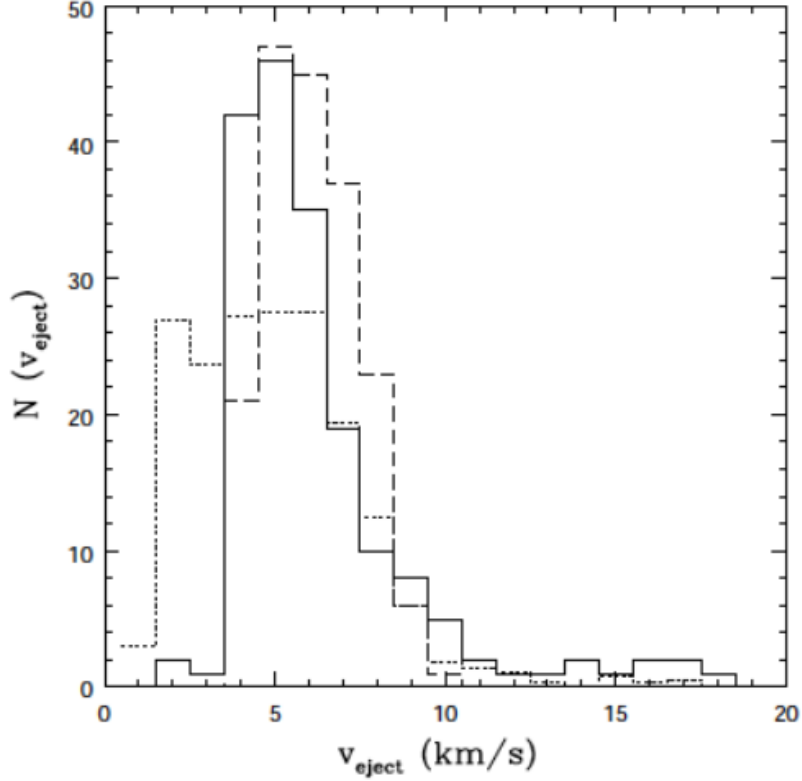


Figure 36: Velocity histogram of planetesimals removed from a planetary system due to Giant Planet-crossing orbits [Adams & Spergel, 2005]

Third, the velocities for the unbounded particles due to stellar winds during the Asymptotic Giant Branch (AGB) phase were found to be between 0 and 1 km/s by Veras [2020]. These velocities are distinctively smaller than the ones produced by star-disk encounters and giant planet scattering. The transfer of momentum from the free-travelling photons and hadrons to the planetesimals is deemed sufficient to make them become unbound. This particular analysis has not been published before. This figure was obtained through private communication with the author. Fig. 1 visually shows how this mechanism transfers momentum from the outer shells of the star to the planetesimals. Taking a closer look at the Fig. 37 one can see that the peak of the distribution is at around 0.2 km/s and decreases in an exponential fashion for increasing velocities. This was the case for a $5M_{\odot}$ star, but one could assume that the rate of momentum transfer would be bigger with increasing mass. This would entail that there would be a different distribution for the higher-mass cases that might result in values that might overlap with velocities from the other mechanisms.

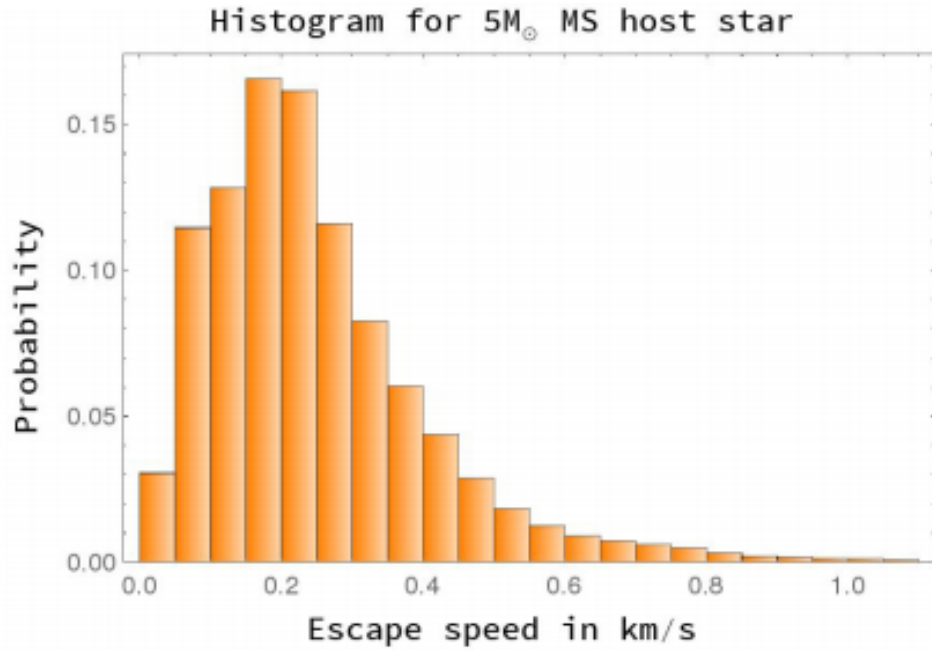


Figure 37: Velocity histogram of planetesimals removed from planetary system due to stellar winds during the 5 solar mass asymptotic giant branch (AGB) phase [Veras, 2020]

From the results found in this thesis work and Fig. 35- 37 the assertion that it is possible to determine the source of an ISO based on its velocity remains, at least in theory, feasible. For that, one would need the to figure out the relative velocity of the system it originates from with respect to the Galactic Standard of Rest (GSR). By doing so, the actual escape velocities of the planetesimals can be derived and from there a valid comparison can be performed. To date, no other published study has explored this idea. For this reason, the novelty of this thesis work relies on the fact that it provides a framework that aggregates different results as to address the origin of ISOs.

5 Summary and Conclusions

In this thesis the production of interstellar objects due to close stellar fly-bys to stars surrounded by disks was investigated. The effect of gravitational stellar encounters on protoplanetary disks as shown by the simulations depends on the mass, periastron distance and inclination and can be quite strong. The different parameters that were explored in this thesis portray the different scenarios in which these encounters might take place in young clusters and the resulting production of candidate ISOs. The different probabilities of occurrence for the specific encounters within the cluster is not addressed here. The results of this study can be summarized as follows:

- The more massive and closer the encounter the more destruction on the disk.
- The percentage of unbounded particles after the completion of the encounter is determined primarily by the perturber mass and it decreases as a function of the periastron distance of the encounter and increases for higher masses. (See Fig. 19)
- Not all particles that become unbound from the parent star turn into ISOs, some are captured or even accreted by the perturber. The number of particles that become bounded/accreted by the perturber star peaks when the pertuber mass is $1.5 M_{\odot}$ independent of the periastron distance (See Fig. 20).
- The percentage of particles that become unbounded from the host star increase as a function of pertuber mass for all the different periastron distances (See Fig. 22).
- The velocity distribution of unbounded planetesimals for low-mass encounters ($M < 1.5 M_{\odot}$) range between 0.2 and 1.5 km/s while for the high-mass encounters they range from 0.2 and 3.0 km/s. For masses bigger than $5 M_{\odot}$ there is a distinguishable "double peak" feature in the distribution. We find that even for very high-mass close encounters the ISO velocity rarely exceeds 3 km/s
- The mean velocity of the distribution increases as a function of the mass but remains constant as a function of periastron distance (See Fig. 25 and 26)
- When assuming a mass distribution proportional to $1/R$ we found that the cumulative mass of the unbounded particles heavily depends on the mass of the pertuber star and decreases as a function of perisastron distance (See Fig. 28).
- The number of unbound particles also depends strongly on the inclination of the orbit of the perturber to that of the disk. Most particles become unbound for a co-planar prograde encounter. It was found that amount of unbounded planetesimals decreases dramatically between the range of 90° and 120° . This implies that retrograde encounters (eg. $i > 90^{\circ}$) the encounter are significantly less destructive (See Fig. 32)
- The velocity distributions for the different inclinations follow the same pattern discussed in the previous point. The histogram rapidly shrinks when the angle of inclination becomes retrograde.

- The mean velocity of the distribution decreases as a function of inclination between the values of 0° and 180° .
- The cumulative mass of the unbounded particles decreases rapidly as a function of inclination once it enters into retrograde territory (See Fig. 57).
- The velocities obtained in this study are smaller than those obtained in the work by Hands [2019]. The reason is that Hands et al. give values that include the relative velocity of the individual star's velocity compared to the cluster. Taking the velocity dispersion of the cluster into account both results agree. The advantage of our method is that it can be applied to any type of cluster in a post-processing step. On the other hand, they are different from the other two possible sources for ISO production : 1) AGB winds (0-1 km/s) and 2) Giant planet scattering (5-10 km/s).
- ISOs produced by different mechanisms lead to distinctly different ISO ejection velocities.

Several questions remain open that need to be addressed in future studies. First, using any of the standard IMF functions and the results in this study one could be able to implement a simulation able to more accurately recreate the different probabilities for the production of ISOs. Open young clusters such as the ONC remain viable candidates to base these models on due to their age and size. This would entail a vastly more comprehensive study given the huge range of possible combinations between the different masses and the parameters studied in this work. This would possibly answer the question of how a stellar cluster/association produce ISOs. Second, a natural expansion on this kind of work would be the determination of the particle density of ISOs in different regions of the galaxy. For comparison, the number density of unbounded planetesimals in our galactic neighborhood is estimated to be of 10^{15} per cubic parsec. By performing simulations on both open and globular clusters we could calculate how many total ISOs end up free-roaming through space per unit volume. Third, it would be interesting to better determine the growth timescales in the outer disk to see at what time in disk development ISOs of the size of Oumuamua or Borisov can be produced. Fourth, another extension for this study would be the investigation of the effect of binary populations in an N-body cluster simulation. Previous work such as the one by Marks & Kroupa [2012] have demonstrated that binary populations in young stellar clusters dynamically evolve with time. This would entail that the production of unbounded planetesimals would not be constant in time but rather would be produced in short bursts.

In conclusion, in this work a comprehensive study of star-disk interactions was presented. A special focus was put on the planetesimals becoming unbounded to the system after the encounter. By considering the different combinations of perturber mass, proximity of the encounter, inclination and angle of periastron the properties of the encounters were determined. This work can be thought of as an extension of what Breslau et al. [2018] and Bhandare [2015] explored. It is also a valuable complement to the available literature on the study of the source of ISOs. This work might serve as a stepping stone for future studies on star-disk encounters as likely sources for ISOs such as Oumuamua and Borisov.

6 Appendices

6.1 Numerical Tables

Table 1: Percentage of Unbounded Particles vs Periastron Distance for co-planar prograde case

Mass	P=80au	P=100au	P=120au	P=140au	P=160au	P=200au	P=250au	P=350au
M=0.3	0.122	0.071	0.036	0.008	0.008	0.000	0.000	0.000
M=0.5	0.346	0.192	0.080	0.011	0.001	0.000	0.000	0.000
M=0.75	0.451	0.289	0.157	0.064	0.015	0.000	0.000	0.000
M=1	0.482	0.349	0.209	0.111	0.051	0.000	0.000	0.000
M=1.5	0.522	0.429	0.311	0.213	0.139	0.039	0.007	0.000
M=2	0.549	0.471	0.396	0.303	0.232	0.107	0.000	0.000
M=5	0.669	0.664	0.646	0.626	0.600	0.472	0.279	0.042
M=10	0.781	0.806	0.817	0.817	0.807	0.747	0.567	0.197
M=20	0.861	0.886	0.898	0.899	0.893	0.860	0.781	0.442
M=50	0.931	0.943	0.944	0.939	0.931	0.913	0.886	0.772

Table 2: Percentage of Unbounded Particles vs Perturber Mass for co-planar prograde case

Periastron	M=0.3	M=0.5	M=0.75	M=1	M=1.5	M=2	M=5	M=10	M=20	M=50
P=80 au	0.122	0.346	0.451	0.482	0.522	0.549	0.669	0.780	0.860	0.930
P=100 au	0.071	0.192	0.289	0.349	0.428	0.471	0.664	0.806	0.886	0.943
P=120 au	0.036	0.080	0.157	0.209	0.310	0.396	0.646	0.817	0.898	0.943
P=140 au	0.008	0.011	0.064	0.110	0.213	0.303	0.626	0.817	0.899	0.939
P=160 au	0.001	0.001	0.015	0.050	0.139	0.232	0.600	0.807	0.893	0.930
P=200 au	0.000	0.000	0.000	0.000	0.039	0.107	0.471	0.747	0.860	0.912
P=250 au	0.000	0.000	0.000	0.000	0.007	0.028	0.278	0.567	0.781	0.885
P=350 au	0.000	0.000	0.000	0.000	0.000	0.000	0.042	0.197	0.442	0.772

Table 3: Percentage of Particles Bounded to Star 2 vs Perturber Mass for co-planar prograde case

Periastron	M=0.3	M=0.5	M=0.75	M=1	M=1.5	M=2	M=5	M=10	M=20	M=50
P=80 au	0.194	0.236	0.261	0.280	0.290	0.291	0.236	0.154	0.089	0.032
P=100 au	0.234	0.275	0.303	0.323	0.326	0.321	0.212	0.112	0.052	0.012
P=120 au	0.196	0.266	0.315	0.341	0.343	0.327	0.197	0.082	0.028	0.004
P=140 au	0.151	0.213	0.267	0.308	0.325	0.310	0.178	0.059	0.014	0.001
P=160 au	0.097	0.151	0.200	0.237	0.267	0.266	0.151	0.039	0.007	0.000
P=200 au	0.0135	0.048	0.086	0.118	0.151	0.157	0.099	0.019	0.001	0.000
P=250 au	0.000	0.000	0.003	0.019	0.048	0.060	0.042	0.004	0.001	0.000
P=350 au	0.000	0.000	0.000	0.000	0.000	0.000	0.001	0.002	0.001	0.000

Table 4: Mean Velocity of Unbounded Particles vs Periastron Distance

Mass	P=80au	P=100au	P=120au	P=140au	P=160au	P=200au	P=250au	P=350au
M=0.3	0.751	0.729	0.683	0.550	0.434	nan	nan	nan
M=1	0.749	0.670	0.591	0.507	0.411	nan	nan	nan
M=2	1.053	1.068	1.040	1.065	1.057	1.028	1.327	nan
M=5	1.385	1.434	1.298	1.429	1.357	1.248	1.105	0.998
M=10	1.594	1.626	1.479	1.603	1.573	1.473	1.380	1.168
M=50	2.004	2.049	2.261	2.152	2.205	2.220	2.233	2.073

Table 5: Cumulative Mass of Unbounded Particles vs Periastron Distance

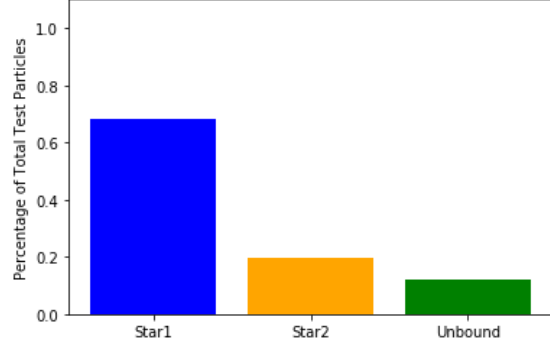
Mass	P=80au	P=100au	P=120au	P=140au	P=160au	P=200au	P=250au	P=350au
M=0.3	0.086	0.046	0.021	0.005	0.001	0.000	0.000	0.000
M=0.5	0.271	0.128	0.048	0.006	0.001	0.000	0.000	0.000
M=0.75	0.397	0.217	0.104	0.039	0.009	0.000	0.000	0.000
M=1	0.436	0.289	0.150	0.072	0.031	0.000	0.000	0.000
M=1.5	0.478	0.381	0.248	0.157	0.093	0.023	0.004	0.000
M=2	0.505	0.426	0.344	0.241	0.176	0.072	0.018	0.000
M=5	0.618	0.612	0.601	0.592	0.569	0.411	0.199	0.025
M=10	0.727	0.778	0.799	0.799	0.786	0.709	0.476	0.127
M=20	0.832	0.876	0.887	0.881	0.869	0.827	0.735	0.332
M=50	0.922	0.934	0.931	0.922	0.911	0.887	0.855	0.720

Table 6: Cumulative Mass of Unbounded Particles vs Perturber Mass

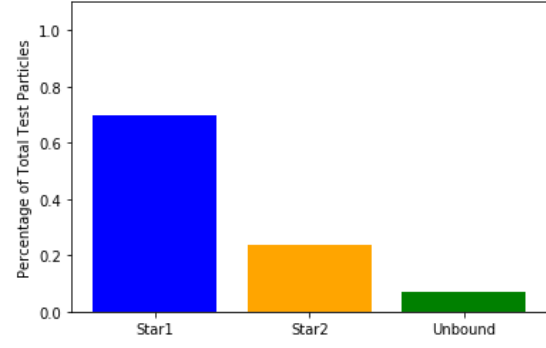
Periastron	M=0.3	M=0.5	M=0.75	M=1	M=1.5	M=2	M=5	M=10	M=20	M=50
P=80 au	0.086	0.271	0.397	0.437	0.478	0.506	0.618	0.727	0.832	0.923
P=100 au	0.046	0.128	0.217	0.289	0.381	0.429	0.612	0.779	0.876	0.934
P=120 au	0.021	0.049	0.104	0.150	0.248	0.345	0.601	0.799	0.886	0.931
P=140 au	0.005	0.006	0.039	0.072	0.157	0.241	0.593	0.799	0.889	0.921
P=160 au	0.000	0.001	0.008	0.031	0.092	0.176	0.569	0.786	0.869	0.911
P=200 au	0.000	0.000	0.000	0.000	0.023	0.072	0.411	0.709	0.827	0.887
P=250 au	0.000	0.000	0.000	0.000	0.004	0.017	0.199	0.476	0.735	0.855
P=350 au	0.000	0.000	0.000	0.000	0.000	0.000	0.024	0.128	0.332	0.720

6.2 Complementary Figures

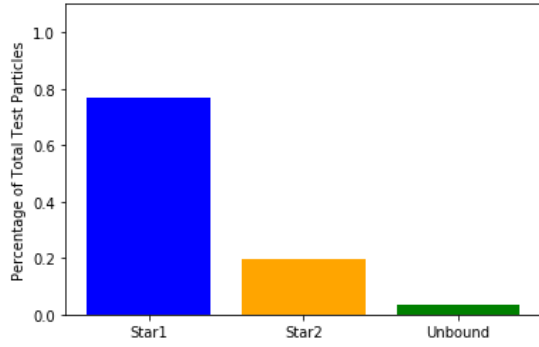
Percentage of Particles by Type for $M=0.3M_{\odot}$ for Different Periastron Distances



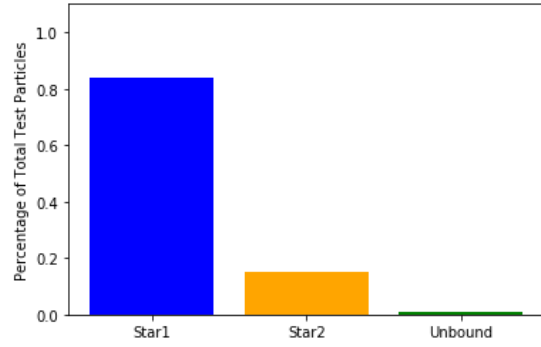
(a) $r_p = 80au$



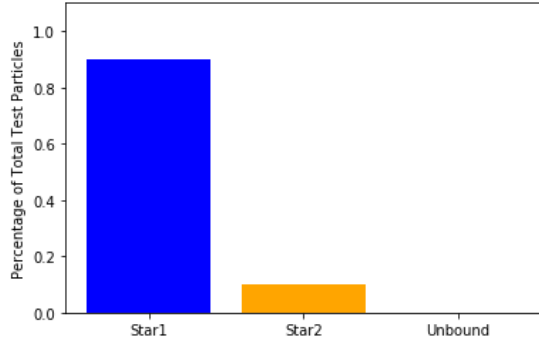
(b) $r_p = 100au$



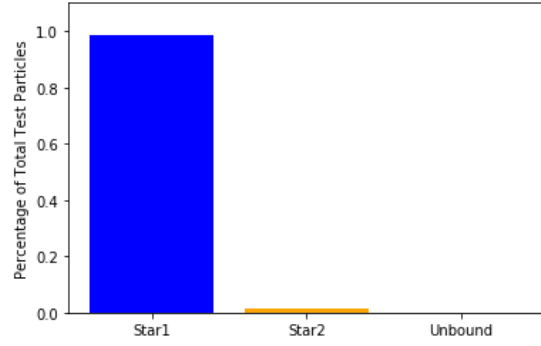
(c) $r_p = 120au$



(d) $r_p = 140au$



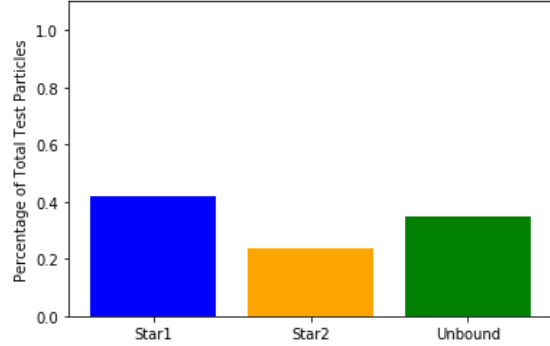
(e) $r_p = 160au$



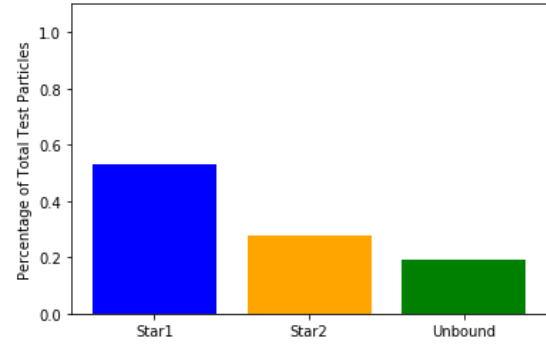
(f) $r_p = 200au$

Figure 38: Percentage of test particles remaining bounded to the host star, captured by the perturber star or becoming unbounded from the system for $M=0.3M_{\odot}$ with changing periastron distance.

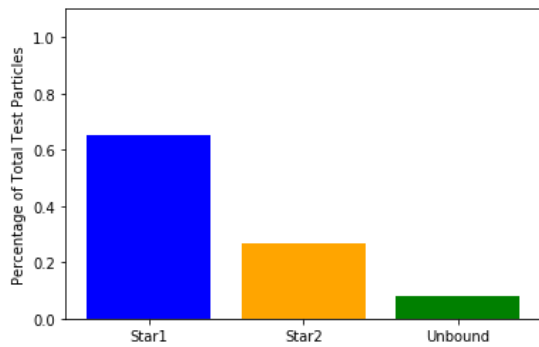
Percentage of Particles by Type for $M=0.5M_{\odot}$ for Different Periastron Distances



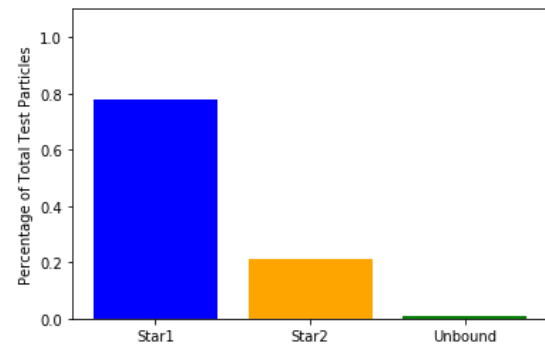
(a) $r_p = 80au$



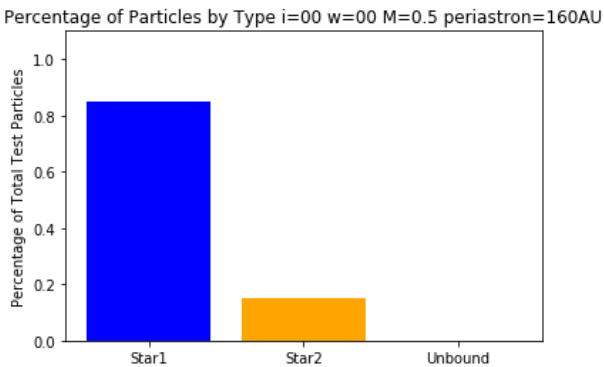
(b) $r_p = 100au$



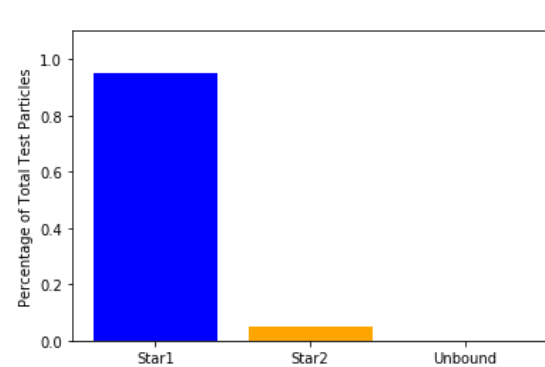
(c) $r_p = 120au$



(d) $r_p = 140au$



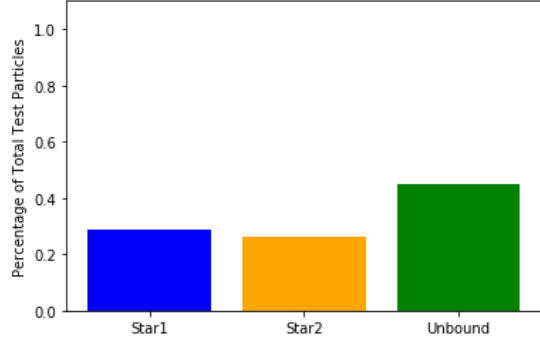
(e) $r_p = 160au$



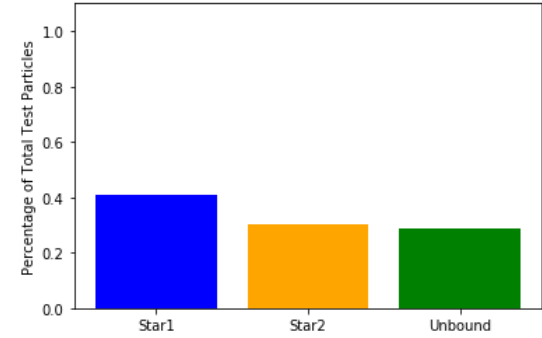
(f) $r_p = 200au$

Figure 39: Percentage of test particles remaining bounded to the host star, captured by the perturber star or becoming unbounded from the system for $M=0.5M_{\odot}$ with changing periastron distance.

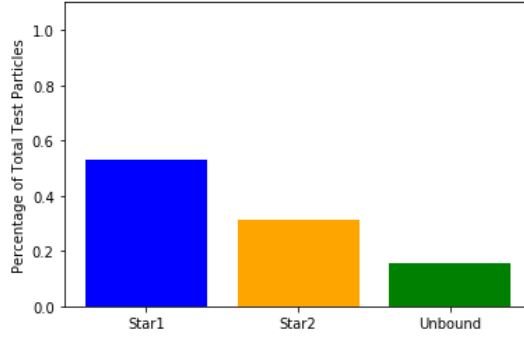
Percentage of Particles by Type for $M=0.75M_{\odot}$ for Different Periastron Distances



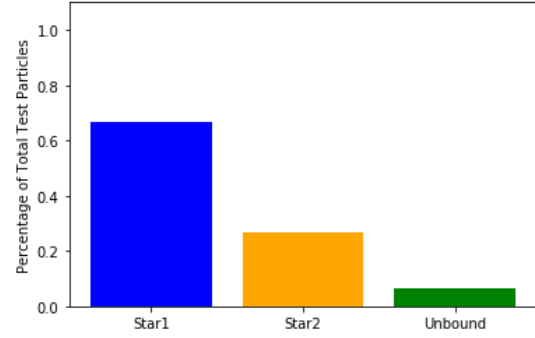
(a) $r_p = 80au$



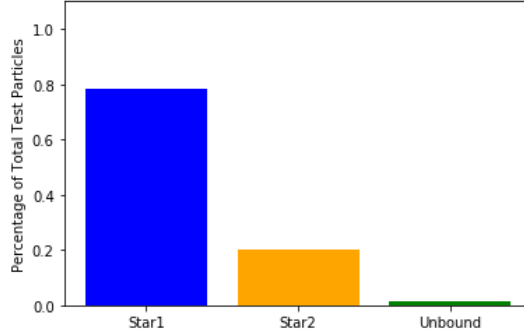
(b) $r_p = 100au$



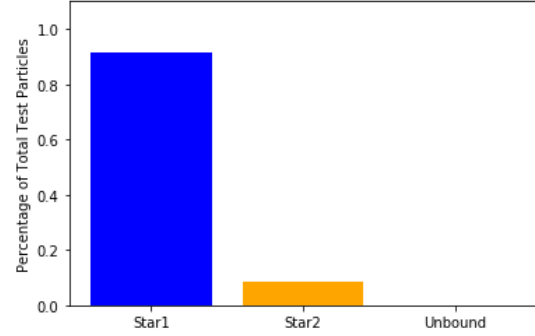
(c) $r_p = 120au$



(d) $r_p = 140au$



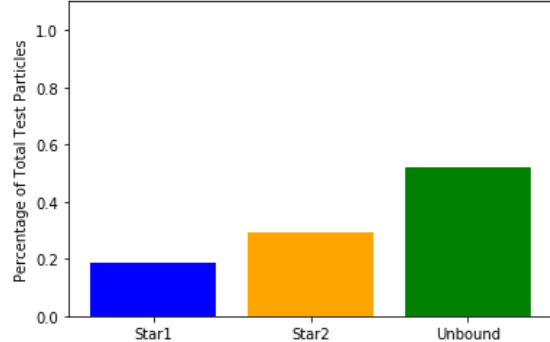
(e) $r_p = 160au$



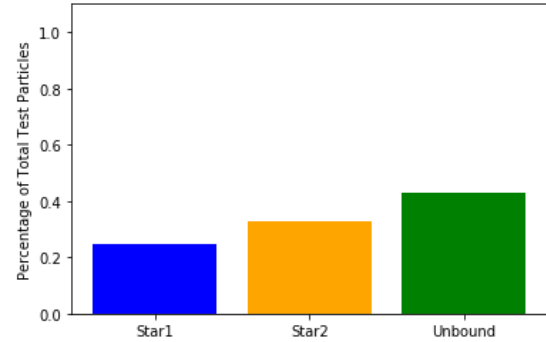
(f) $r_p = 200au$

Figure 40: Percentage of test particles remaining bounded to the host star, captured by the perturber star or becoming unbounded from the system for $M=0.75M_{\odot}$ with changing periastron distance.

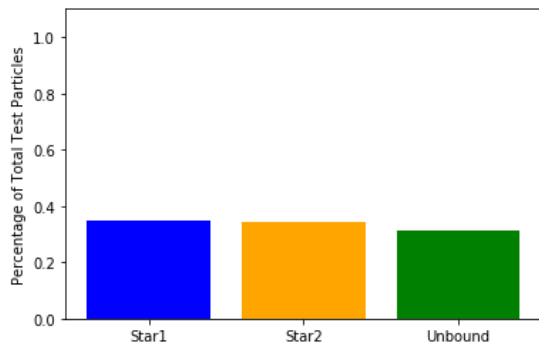
Percentage of Particles by Type for $M=1.5M_{\odot}$ for Different Periastron Distances



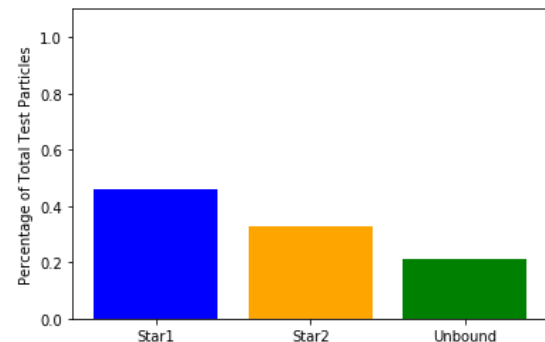
(a) $r_p = 80au$



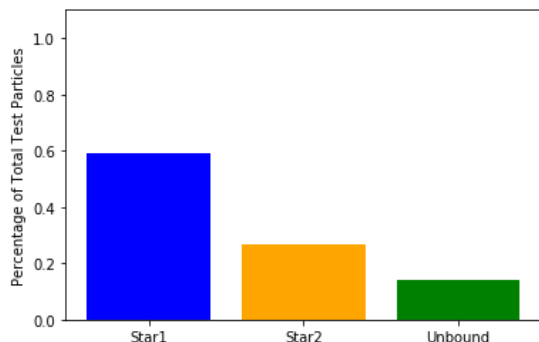
(b) $r_p = 100au$



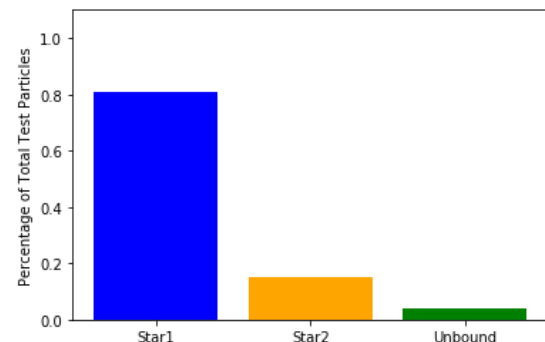
(c) $r_p = 120au$



(d) $r_p = 140au$



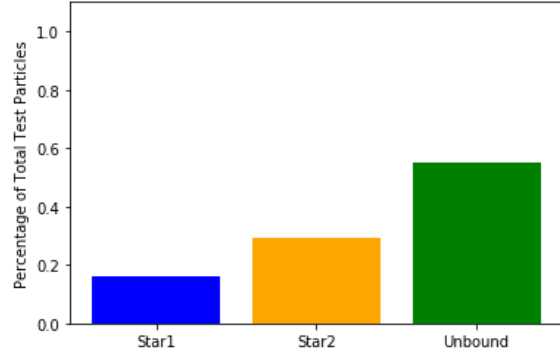
(e) $r_p = 160au$



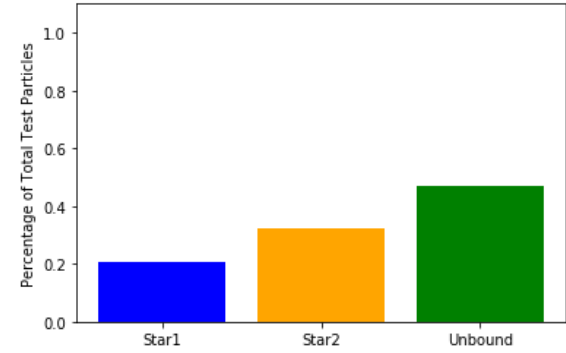
(f) $r_p = 200au$

Figure 41: Percentage of test particles remaining bounded to the host star, captured by the perturber star or becoming unbounded from the system for $M=1.5M_{\odot}$ with changing periastron distance.

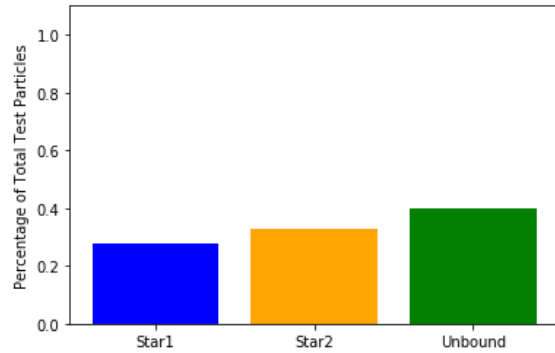
Percentage of Particles by Type for $M=2M_{\odot}$ for Different Periastron Distances



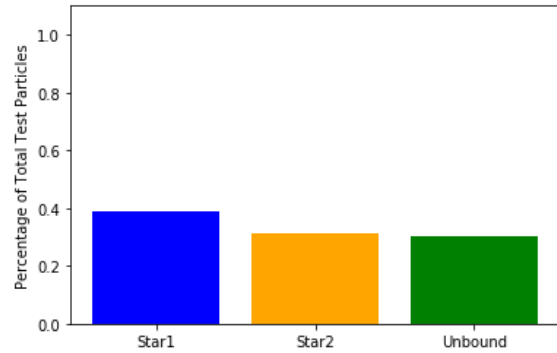
(a) $r_p = 80au$



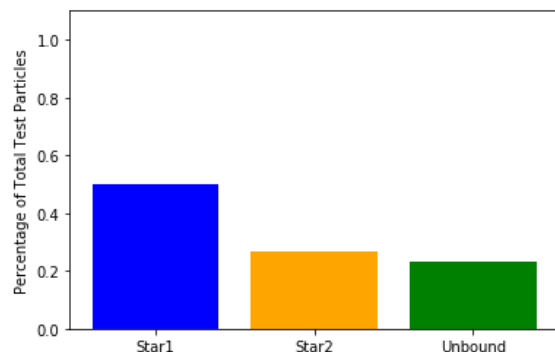
(b) $r_p = 100au$



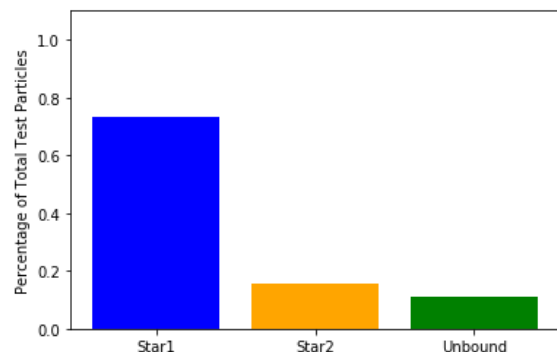
(c) $r_p = 120au$



(d) $r_p = 140au$



(e) $r_p = 160au$



(f) $r_p = 200au$

Figure 42: Percentage of test particles remaining bounded to the host star, captured by the perturber star or becoming unbounded from the system for $M=2M_{\odot}$ with changing periastron distance.

Percentage of Particles by Type for $M=5M_{\odot}$ for Different Periastron Distances

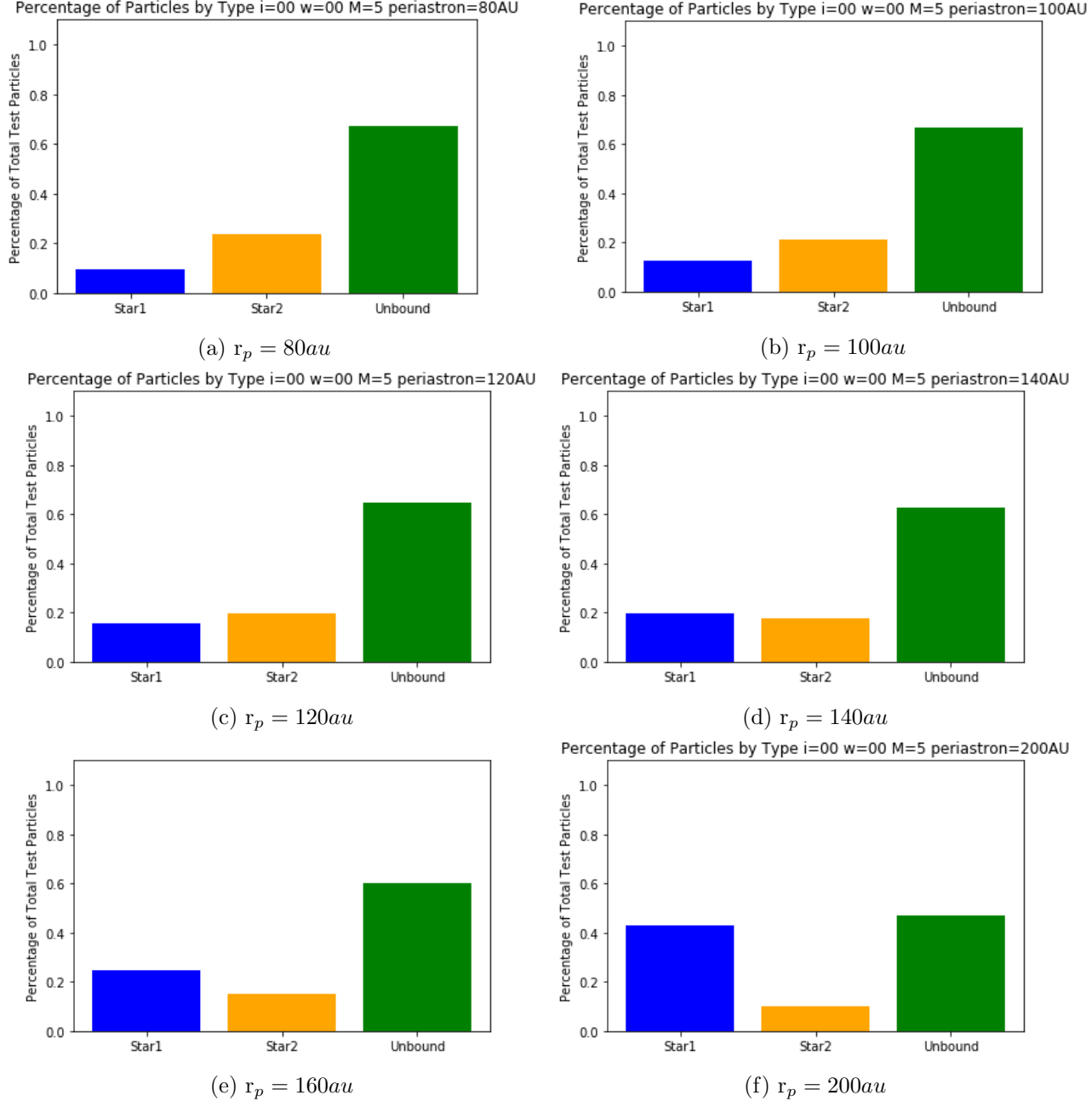
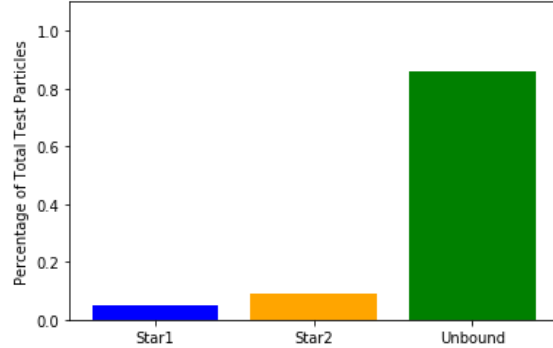
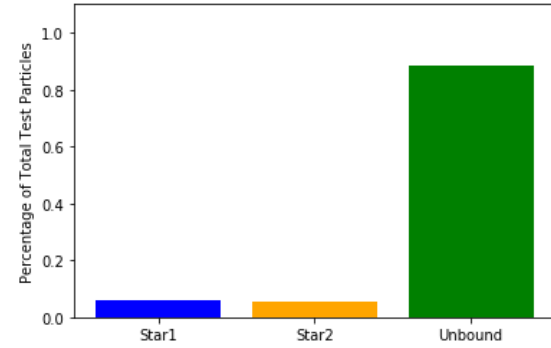


Figure 43: Percentage of test particles remaining bounded to the host star, captured by the perturber star or becoming unbounded from the system for $M=5$ with changing periastron distance.

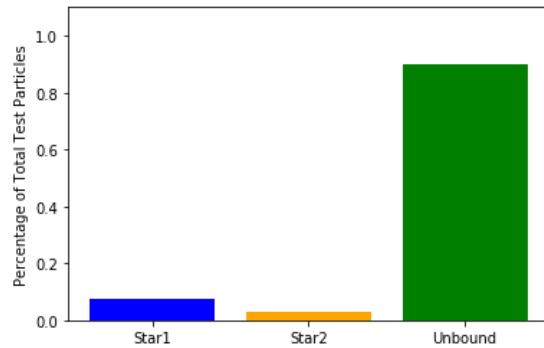
Percentage of Particles by Type for $M=20M_{\odot}$ for Different Periastron Distances



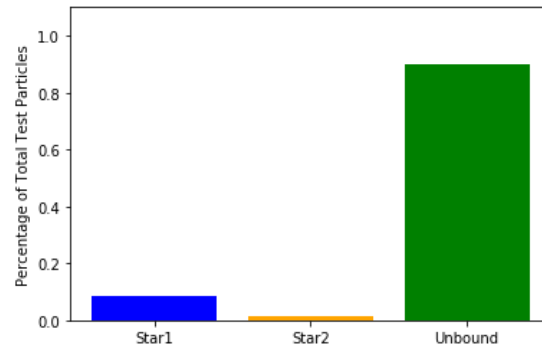
(a) $r_p = 80au$



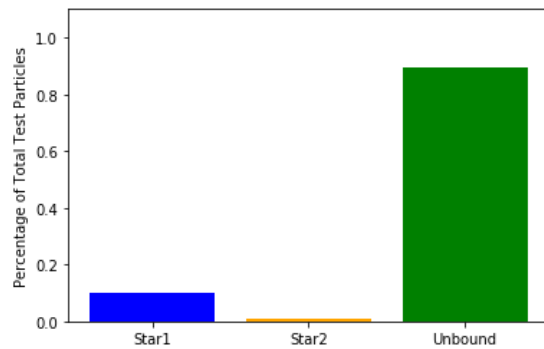
(b) $r_p = 100au$



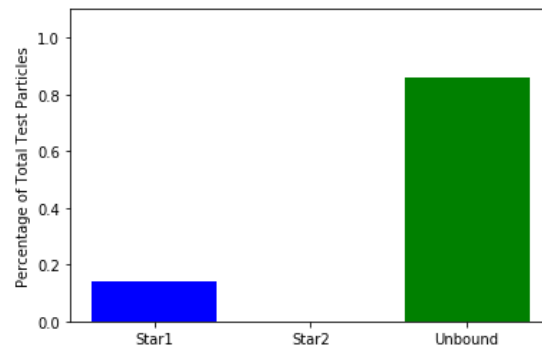
(c) $r_p = 120au$



(d) $r_p = 140au$



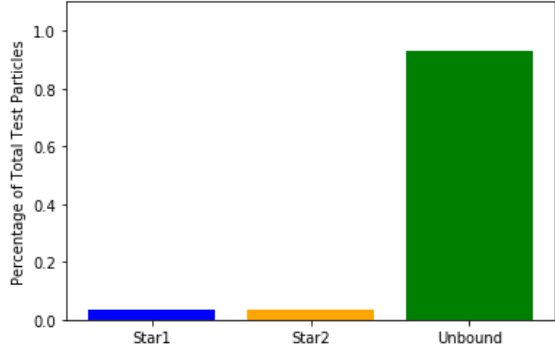
(e) $r_p = 160au$



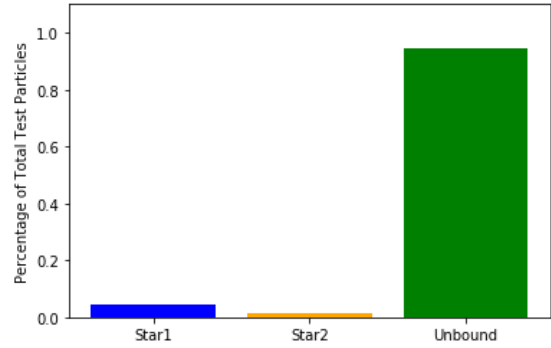
(f) $r_p = 200au$

Figure 44: Percentage of test particles remaining bounded to the host star, captured by the perturber star or becoming unbounded from the system for $M=20M_{\odot}$ with changing periastron distance.

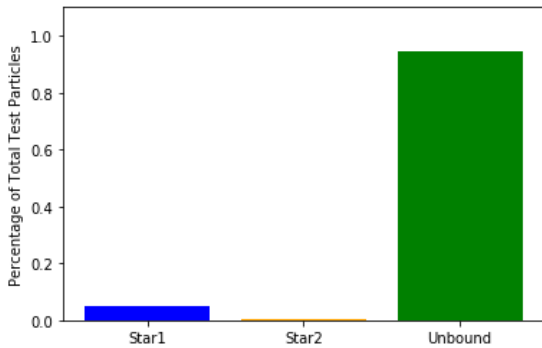
Percentage of Particles by Type for $M=50M_{\odot}$ for Different Periastron Distances



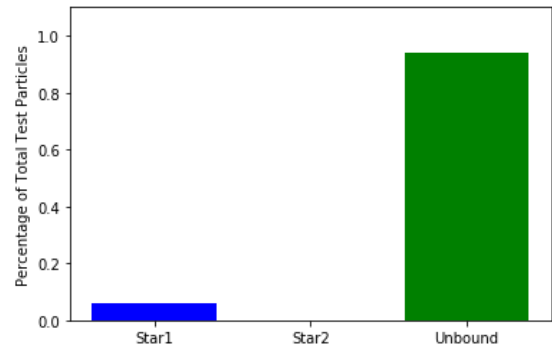
(a) $r_p = 80au$



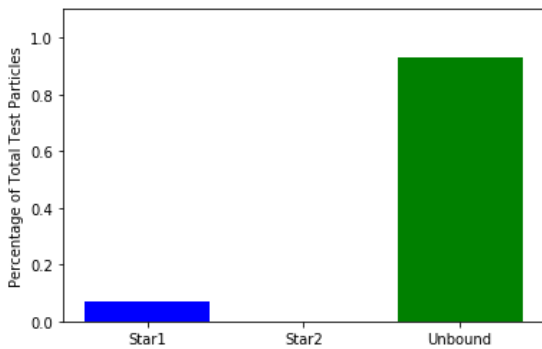
(b) $r_p = 100au$



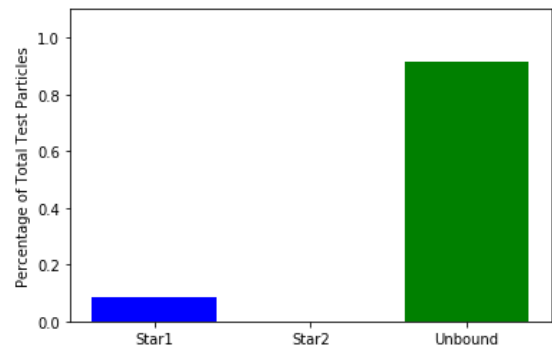
(c) $r_p = 120au$



(d) $r_p = 140au$



(e) $r_p = 160au$



(f) $r_p = 200au$

Figure 45: Percentage of test particles remaining bounded to the host star, captured by the perturber star or becoming unbounded from the system for $M=50M_{\odot}$ with changing periastron distance.

Velocity Distribution of Unbounded Particles for $M=0.3M_{\odot}$ and Different Periastron Distances

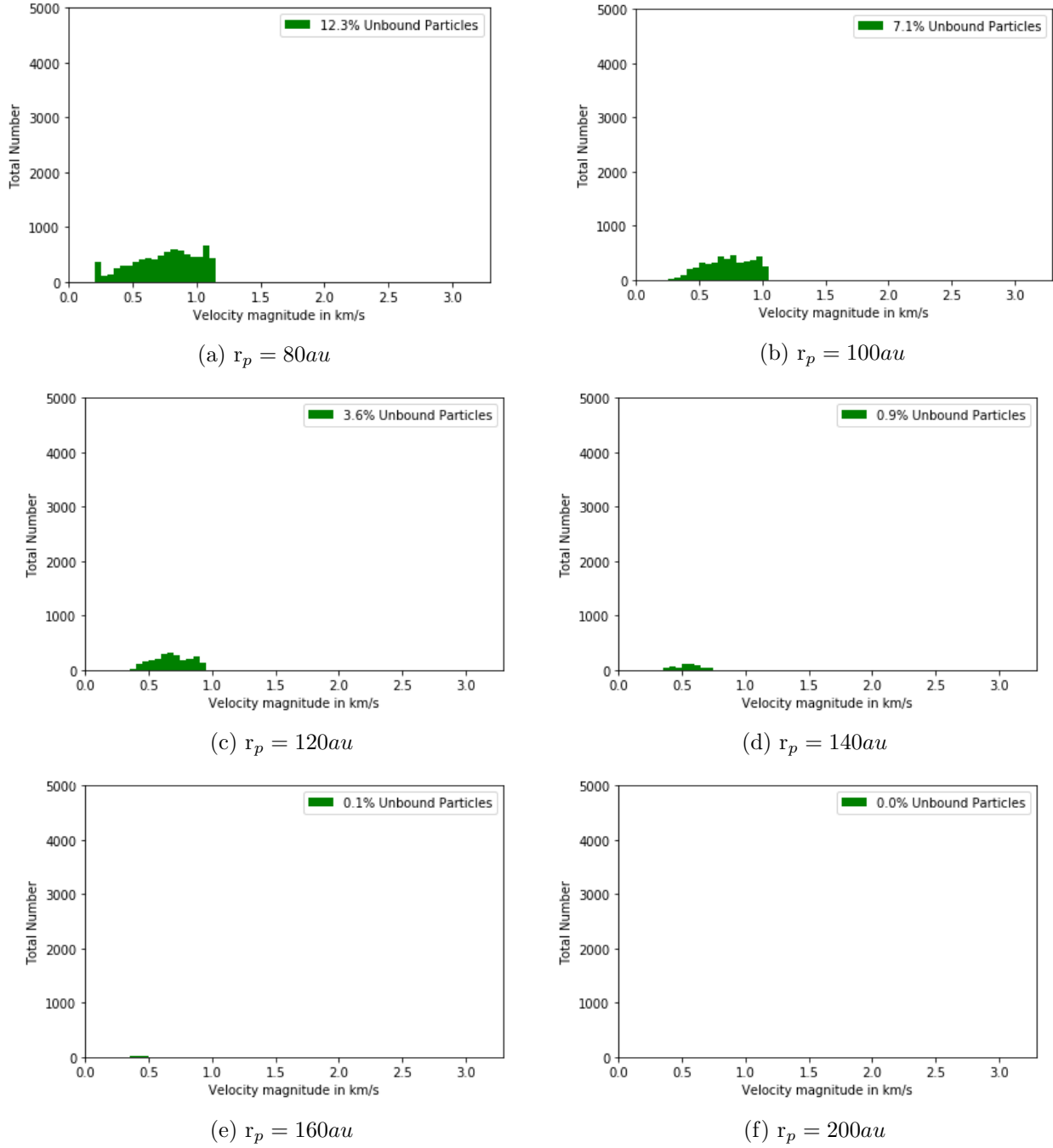


Figure 46: Velocity distribution of unbounded test particles for $M=0.3M_{\odot}$ and different periastron distances.

Velocity Distribution of Unbounded Particles for $M=0.5M_{\odot}$ and Different Periastron Distances

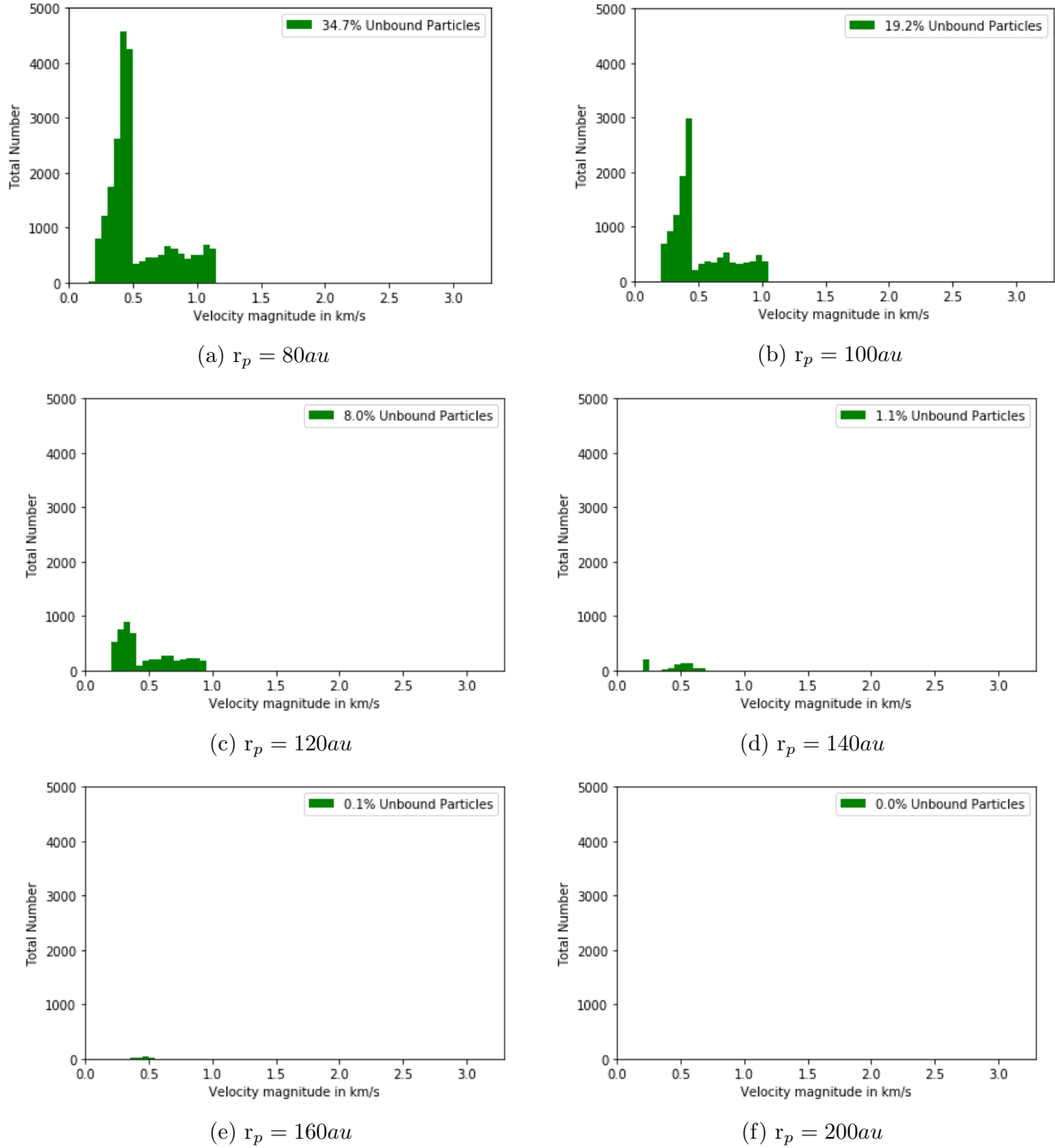


Figure 47: Velocity distribution of unbounded test particles for $M=0.5M_{\odot}$ and different periastron distances.

Velocity Distribution of Unbounded Particles for $M=0.75M_{\odot}$ and Different Periastron Distances

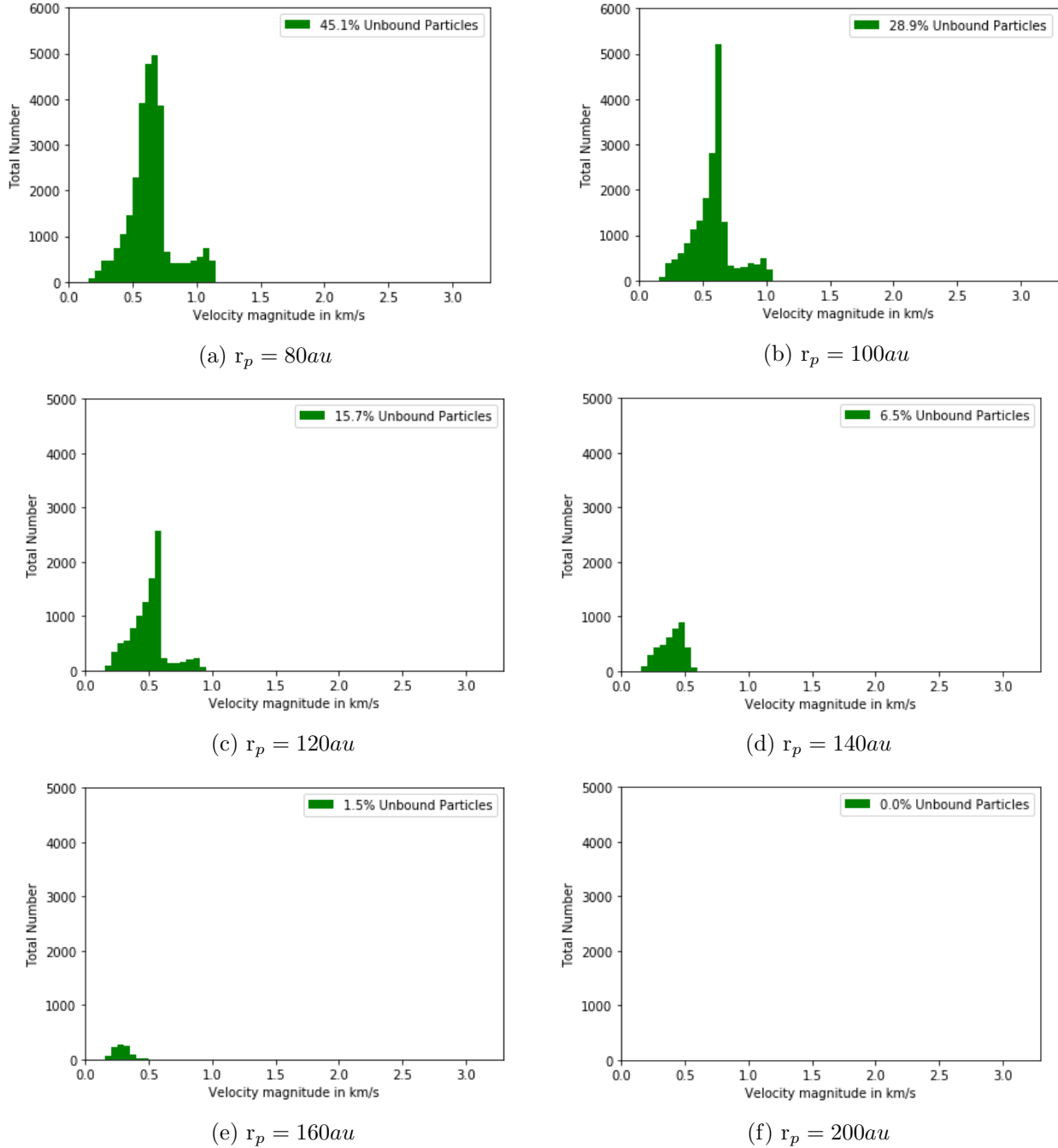


Figure 48: Velocity distribution of unbounded test particles for $M=0.75M_{\odot}$ and different periastron distances.

Velocity Distribution of Unbounded Particles for $M=1.5M_{\odot}$ and Different Periastron Distances

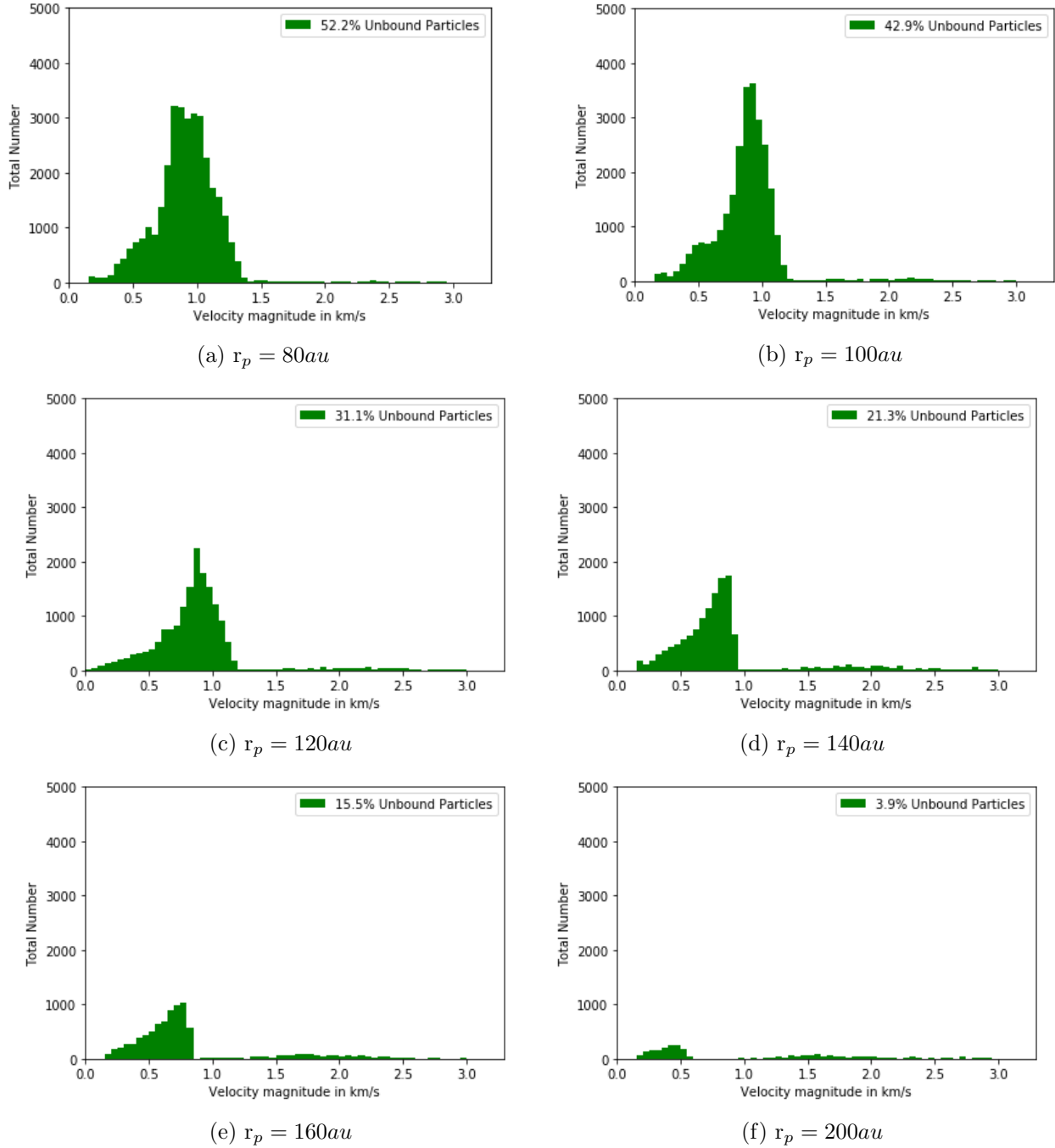


Figure 49: Velocity distribution of unbounded test particles for $M=1.5M_{\odot}$ and different periastron distances.

Velocity Distribution of Unbounded Particles for $M=2M_{\odot}$ and Different Periastron Distances

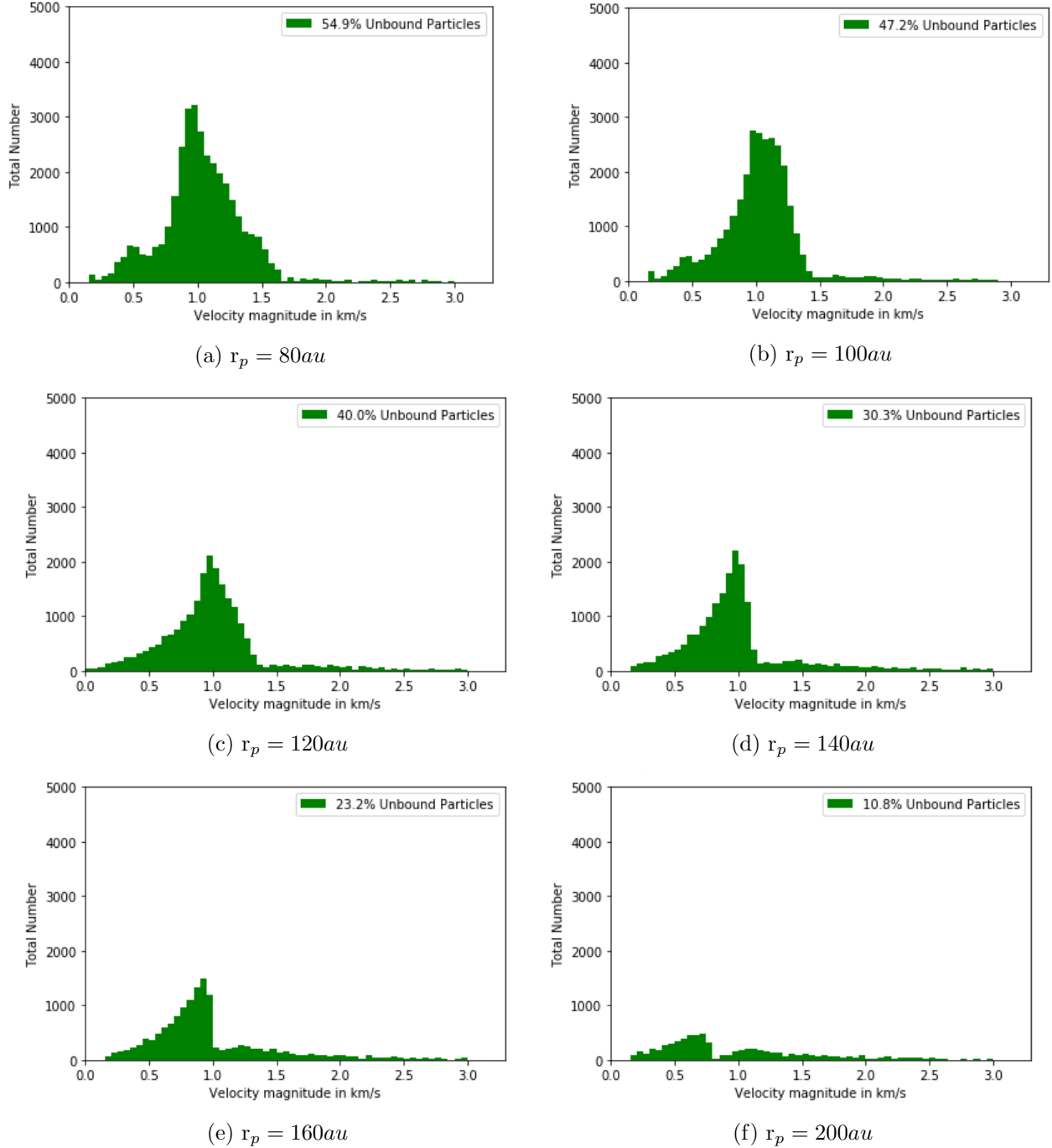


Figure 50: Velocity distribution of unbounded test particles for $M=2M_{\odot}$ and different periastron distances.

Velocity Distribution of Unbounded Particles for $M=5M_{\odot}$ and Different Periastron Distances

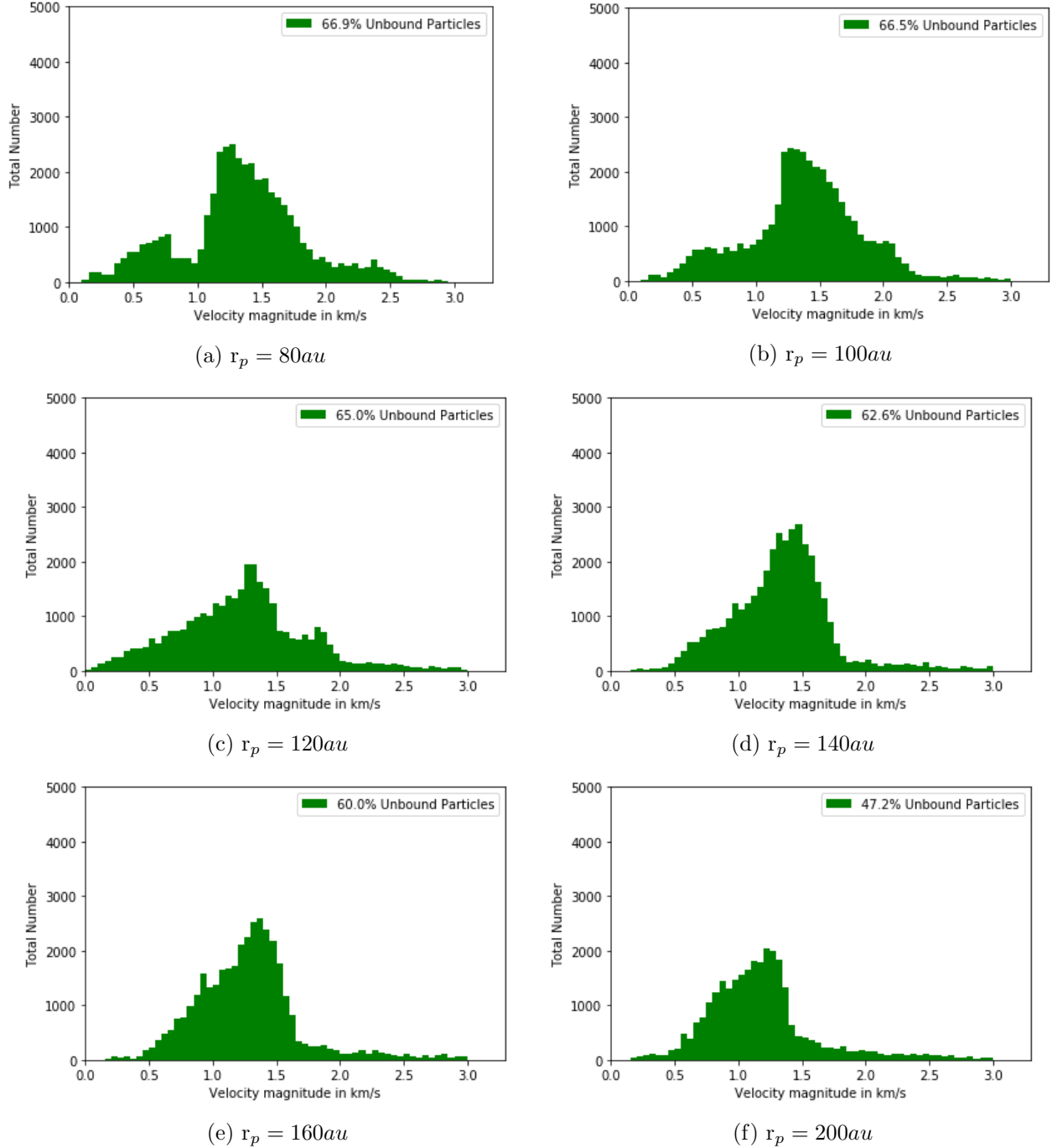


Figure 51: Velocity distribution of unbounded test particles for $M=5M_{\odot}$ and different periastron distances.

Velocity Distribution of Unbounded Particles for $M=20M_{\odot}$ and Different Periastron Distances

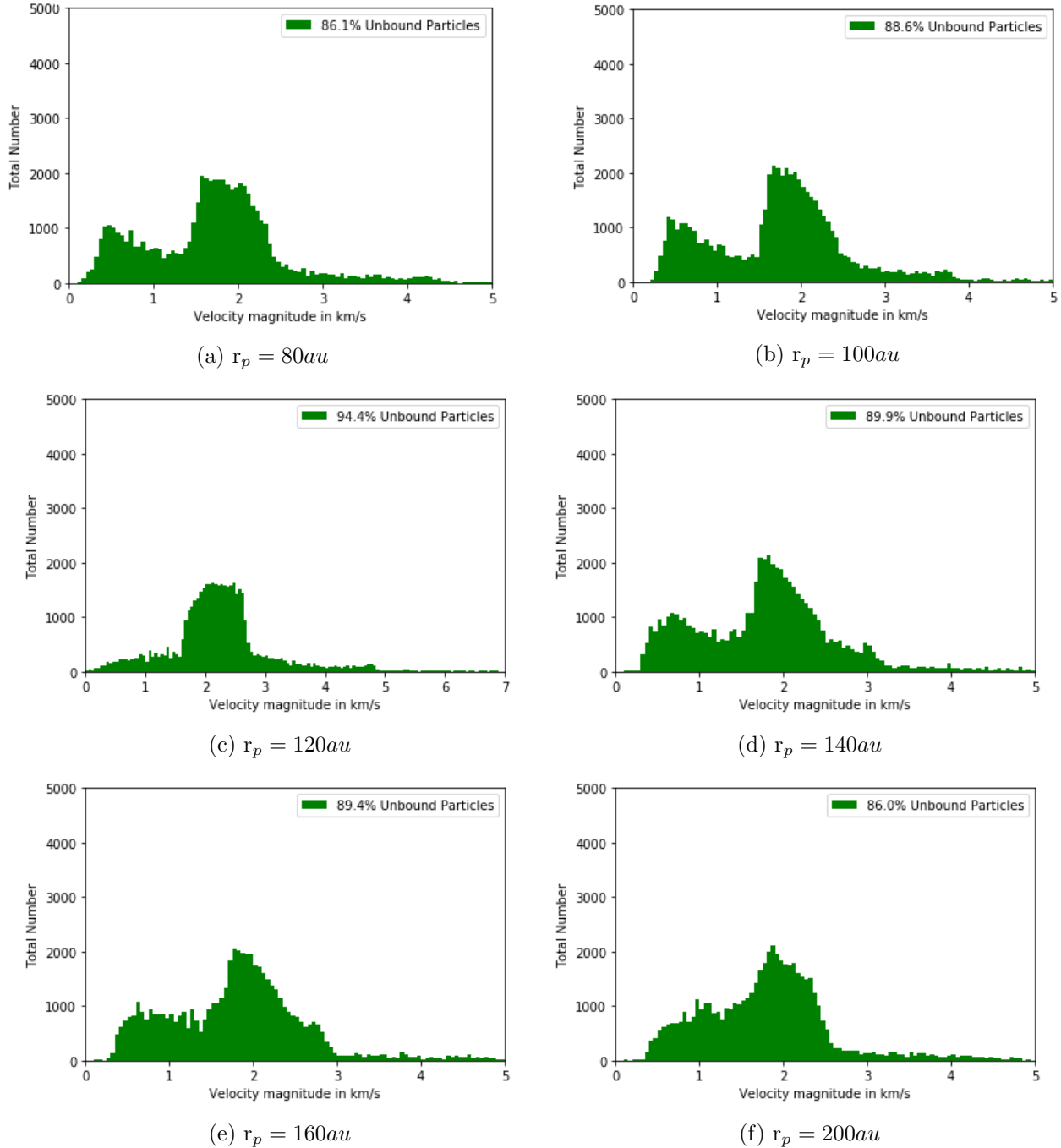


Figure 52: Velocity distribution of unbounded test particles for $M=20M_{\odot}$ and different periastron distances.

Velocity Distribution of Unbounded Particles for $M=50M_{\odot}$ and Different Periastron Distances

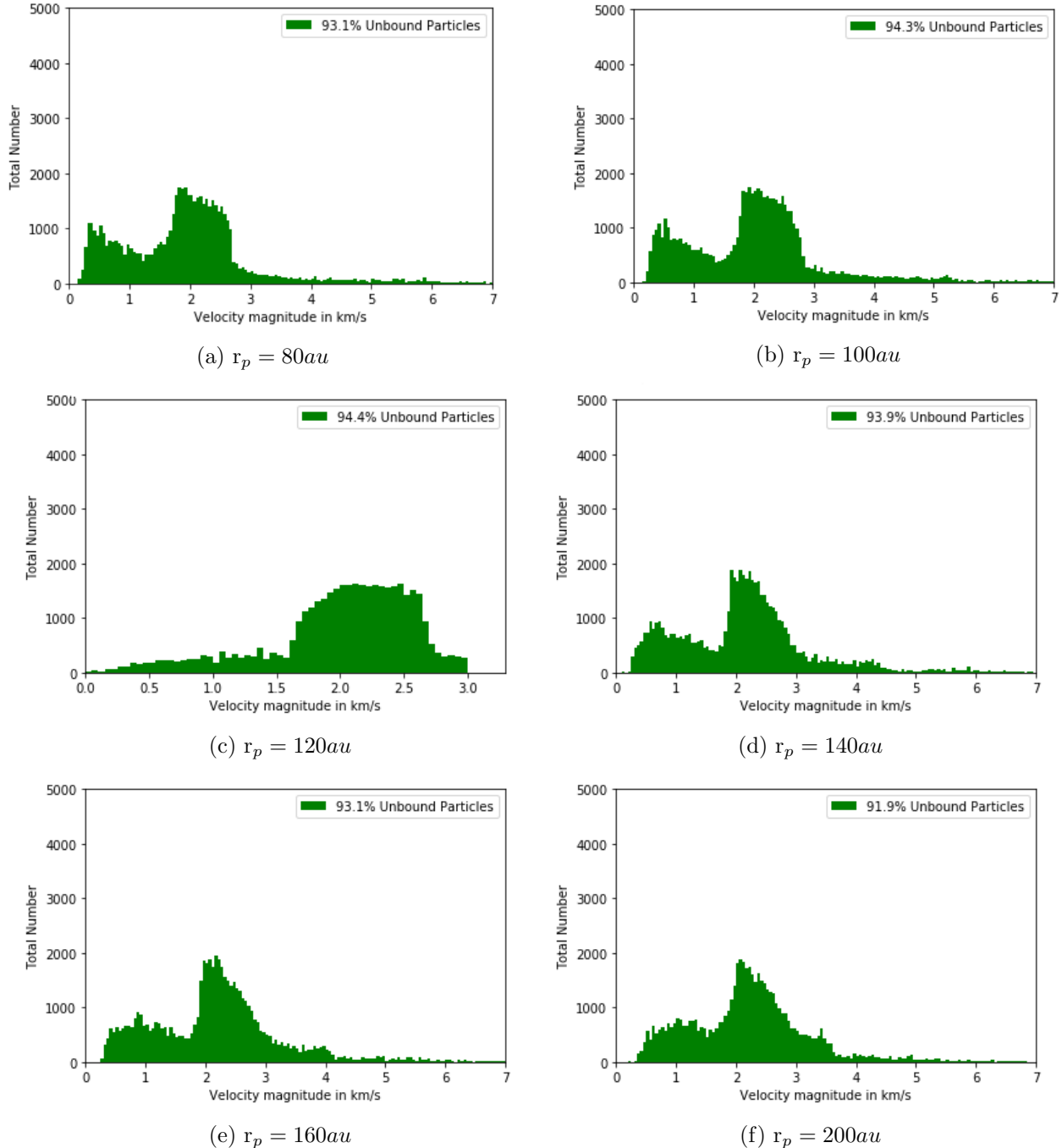
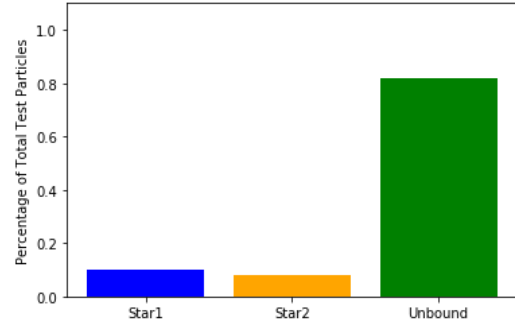
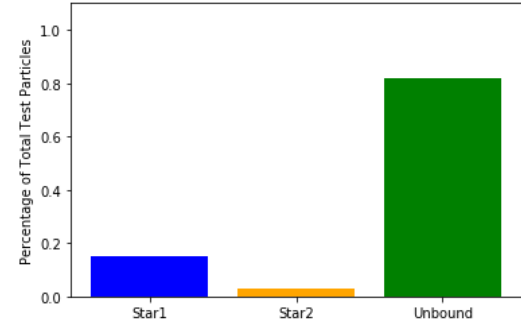


Figure 53: Velocity distribution of unbounded test particles for $M=50M_{\odot}$ and different periastron distances.

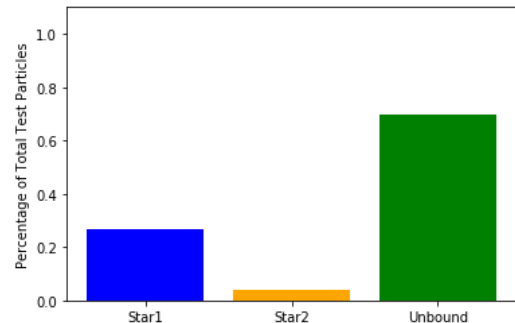
Percentage of Particles by Type for $M=10M_{\odot}$ for Different Inclinations



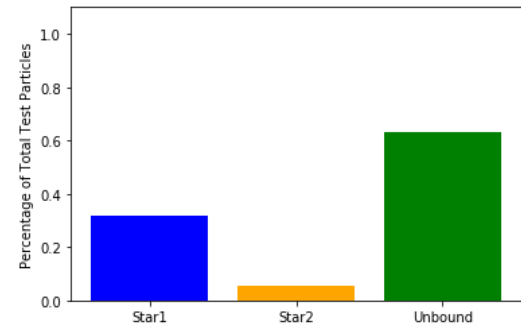
(a) $i=00^{\circ}$



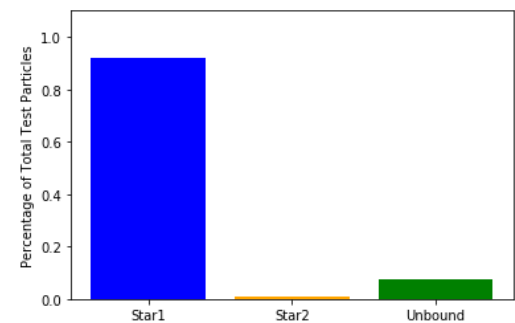
(b) $i=60^{\circ}$



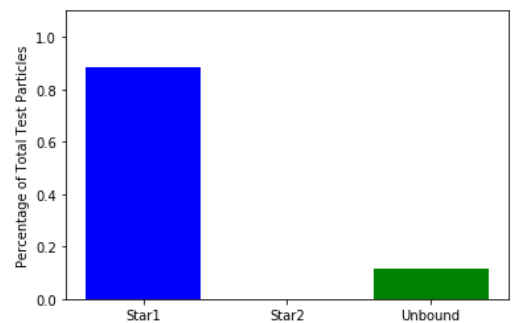
(c) $i=85^{\circ}$



(d) $i=90^{\circ}$



(e) $i=120^{\circ}$



(f) $i=180^{\circ}$

Figure 54: Percentage of test particles remaining bounded to the host star, captured by the perturber star or becoming unbounded from the disk for $M=10M_{\odot}$ with changing inclination.

Velocity Distribution of Unbounded Particles for $M=10M_{\odot}$ and Different Inclinations

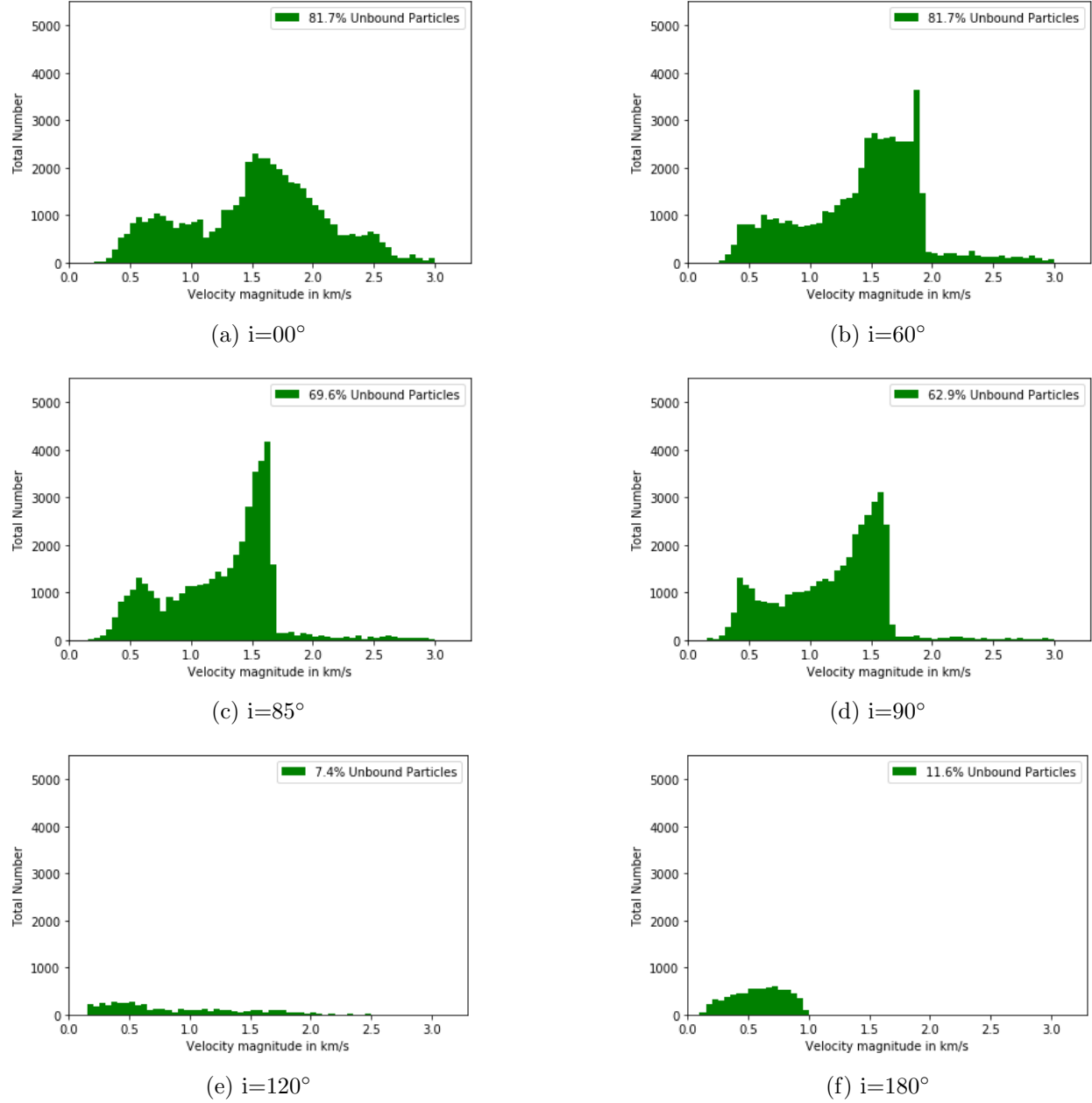
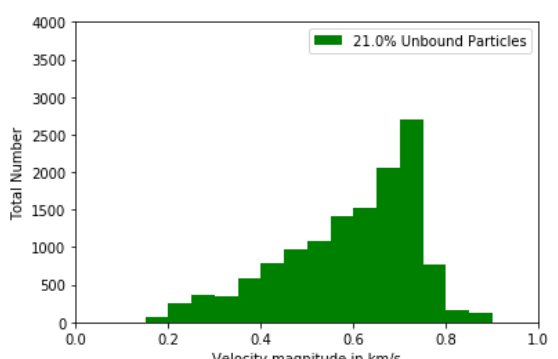
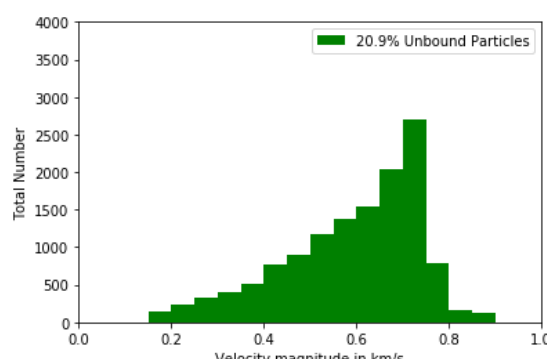
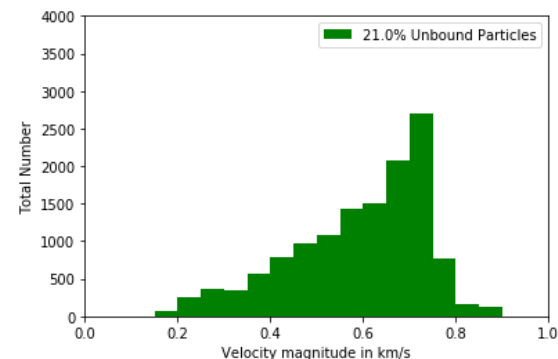
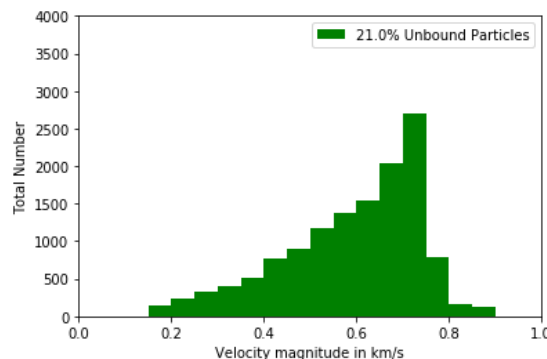
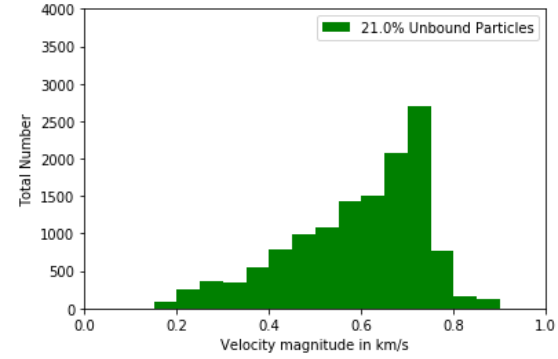
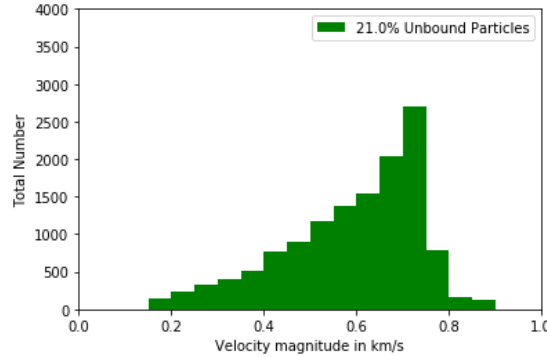


Figure 55: Velocity distribution of test particles for the case of $M=10M_{\odot}$ and changing inclinations

Velocity Distribution of Unbounded Particles for $M=1M_{\odot}$ and Different Angle of Periastron



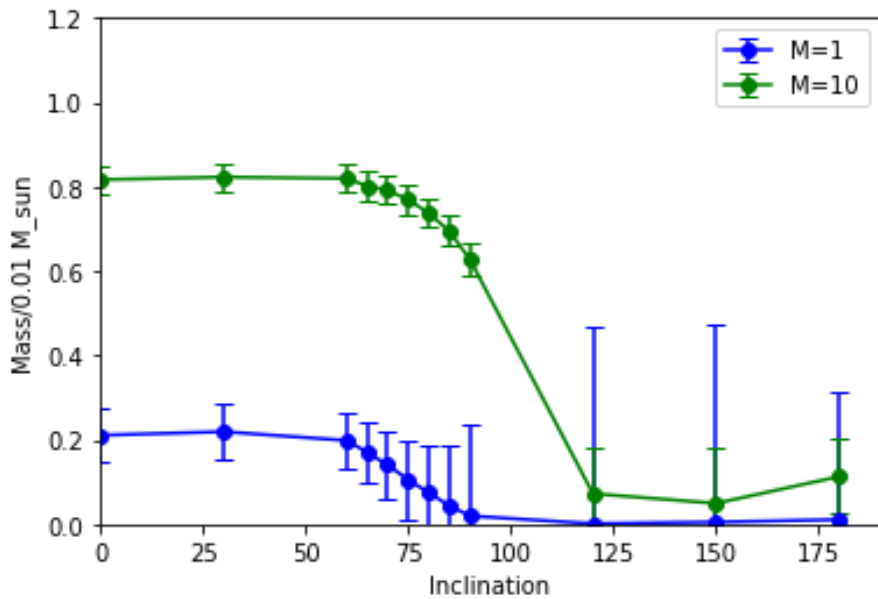


Figure 57: Cumulative mass of the unbounded test particles as a function of inclination for masses $M=1M_{\odot}$ and $M=10M_{\odot}$

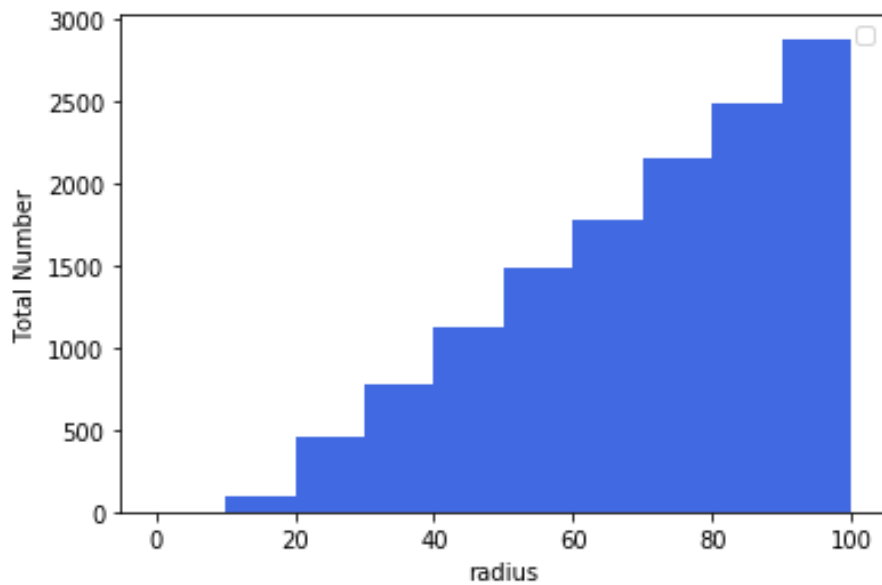


Figure 58: Distribution of unbounded particles as a function of radius

7 Bibliography

References

- [1] F.C. Adams & D.N. Spergel. *Lithopanspermia in Star Forming Clusters* Astrophysics (astro-ph), April 2005. DOI: 10.1089/ast.2005.5.497
- [2] M. Agundez, J. Cernicharo, J. R. Pardo, J. P. Fonfria Exposito, M. Guelin, E. D. Tenenbaum, L. M. Ziurys, A. J. Apponi *Understanding the Chemical Complexity in Circumstellar Envelopes of C-rich AGB Stars: the Case of IRC +10216.* Astrophysics (astro-ph), Feb 2007. DOI: 10.1007/s10509-007-9495-7
- [3] A. Bhandare. *Investigation of the effects of star-disc encounter on protoplanetary disc size.* Master Thesis Work. October, 2015
- [4] A. Bhandare, A. Breslau, S. Pfalzner. *Effects of inclined star-disk encounter on protoplanetary disk size.* A&A 594, A53 (2018), October 2018. DOI: 10.1051/0004-6361/201628086
- [5] A. Breslau & S. Pfalzner. *Creating retrogradely orbiting planets by prograde stellar fly-bys.* Astronomy & Astrophysics manuscript no. aa33729-18, December 2018. DOI: 10.1051/0004-6361/201833729
- [6] A. Bhandare & S. Pfalzner *DESTINY: Database for the Effects of STellarencounters on dIsks and plaNetary sYstems.* Computational Astrophysics and Cosmology. Jan 2019. <https://doi.org/10.1186/s40668-019-0030-3>
- [7] A. Breslau, M. Steinhausen, K. Vincke, and S. Pfalzner. *Sizes of protoplanetary discs after star-disc encounters.* Astrophysics of Galaxies (astro-ph.GA), March 2014. DOI: 10.1051/0004-6361/201323043
- [8] A. Breslau, K. Vincke & S. Pfalzner. *From star-disc encounters to numerical solutions for a subset of the restricted three-body problem.* A&A 599, A91 (2017), November 2017. DOI: 10.1051/0004-6361/201526068
- [9] J.R. Cash & A.H. Karp. *A Variable Order Runge-Kutta Method for Initial Value Problems with Rapidly Varying Right-Hand Sides.* ACM Transactions on Mathematical Software, Vol.16, No.3, September 1990.
- [10] E.A. de la Villarmois, J. K. Jørgensen, L. E. Kristensen, E. A. Bergin, D. Harsono, N. Sakai, E. F. van Dishoeck, and S. Yamamoto. *Physical and chemical fingerprint of protostellar disc formation.* A&A 626, A71 (2019) , May 2019. DOI: 10.1051/0004-6361/201834877
- [11] L.K. Dewangan. *Cluster-Forming Site AFGL 5157: Colliding filamentary clouds and star formation.* Astrophysics of Galaxies (astro-ph.GA), September 2019. DOI: 10.3847/1538-4357/ab4189

- [12] ESO/M.McCaughrean. *Outbursts from a newborn star*. ESO Official Website - <https://www.eso.org/public/images/potw1541a/>, October 2015. Accessed May 2020.
- [13] P. Guzik1, M. Drahus1, K. Rusek, W. Waniak, G. Cannizzaro & Inés Pastor-Marazuela. *Initial characterization of interstellar comet 2I/Borisov*. Earth and Planetary Astrophysics (astro-ph.EP), September 2019 .DOI: 10.1038/s41550-019-0931-8
- [14] S.M. Hall, C.J. Clarke, J.E. Pringle *Energetics of star-disc encounters in the non-linear regime*. Astrophysics (astro-ph), Oct 1995. DOI: 10.1093/mnras/278.2.303
- [15] T.O. Hands, W. Dehnen ,A. Gration, J. Stadel, B. Moore. *The fate of planetesimal discs in young open clusters: implications for 1I/'Oumuamua, the Kuiper belt, the Oort cloud and more*. Earth and Planetary Astrophysics (astro-ph.EP), April 2019. DOI: 10.1093/mnras/stz1069
- [16] C.C. He, M. Ricotti & S. Geen. *Simulating Star Clusters Across Cosmic Time: I. Initial Mass Function, Star Formation Rates and Efficiencies*. Astrophysics of Galaxies (astro-ph.GA), April 2019. DOI: 10.1093/mnras/stz2239
- [17] A.P. Jackson, D. Tamayo, N. Hammond, M. Ali-Dib, H. Rein *Ejection of rocky and icy material from binary star systems: Implications for the origin and composition of 1I/'Oumuamua* . MNRAS 000, 1–6 (2017), March 2018. DOI: 10.1093/mnrasl/sly033
- [18] T. Jerabkova, A.H. Zonoozi, P. Kroupa, G. Beccari, Z. Yan, A. Vazdekis, and Z.Y. Zhang. *The impact of the metallicity and star formation rate on the time-dependent galaxy-wide stellar initial mass function* . A&A 620, A39 (2018), September 2018. DOI: 10.1051/0004-6361/201833055
- [19] H. Kobayashi & S. Ida. *The Effects of a Stellar Encounter on a Planetesimal Disk*. Astrophysics (astro-ph), July 2001. DOI: 10.1006/icar.2001.6700
- [20] K. Kremer, D.J. D'Orazio, J.Samsing, S.Chatterjee, F.A. Rasio. *Probing the Survival of Planetary Systems in Globular Clusters with Tidal Disruption Events*. High Energy Astrophysical Phenomena (astro-ph.HE), August 2019. DOI: 10.3847/1538-4357/ab44d1
- [21] M.R. Krumholz & C.F. McKee . *How do bound star clusters form?*. Astrophysics of Galaxies (astro-ph.GA), September 2019. DOI: 10.1093/mnras/staa659
- [22] C.J Lada & E.Lada. *Embedded Clusters in Molecular Clouds*. Ann. Rev. Astron. Astrophys.41:57-115,2003, Jan 2003 .DOI: 10.1146/annurev.astro.41.011802.094844
- [23] K.H. Lam, Z.Y. Li, C.Y. Chen, K. Tomida and B. Zhao. *Disk Formation in Magnetized Dense Cores with Turbulence and Ambipolar Diffusion* . MNRAS 000, 1-24 (2019), September 2019. DOI: 10.1093/mnras/stz2436
- [24] J. Larwood, P. Kalas *A stellar fly-by simulation giving Beta Pic's disc asymmetries*. Astrophysics (astro-ph), Oct 2000.

- [25] M. Marks & P.Kroupa. *Inverse dynamical population synthesis Constraining the initial conditions of young stellar clusters by studying their binary populations*. *Astrophysics of Galaxies* (astro-ph.GA), May 2012. DOI: 10.1051/0004-6361/201118231
- [26] M. Nagasawa , K.K. Tanaka, H. Tanaka, H. Nomura , T. Nakamoto & H. Miura. *Shock-generating Planetesimals Perturbed by a Giant Planet in a Gas Disk*. *The Astrophysical Journal*, 871:110 (15pp), Janurary 2019.
- [27] S.S.R. Offner, P.C. Clark, P. Hennebelle, N. Bastian, M.R. Bate, P.F. Hopkins, E. Moraux, A.P. Whitworth *The Origin and Universality of the Stellar Initial Mass Function*. <https://www2.mpi-a-hd.mpg.de/homes/beuther/offner.pdf>, Dec 2013.
- [28] C. Olczak, S.Pfalzner, R.Spurzem *Encounter-Triggered Disc Mass Loss in the ONC*. *Astrophysics* (astro-ph), Jan 2006. DOI: 10.1086/501044
- [29] J.M. Oliveira, R.D. Jeffries, J.Th. van Loon, M.J. Kenyon *Young stars and their circumstellar disks in the Sigma Orionis cluster*. *Astrophysics* (astro-ph), May 2003. DOI: 10.1007/1-4020-2600-56
- [30] V. Ossenkopf, R.S. Klessen, and F. Heitsch. *On the structure of self-gravitating molecular clouds*. *A&A* 379, 1005-1016 (2001) September 2001 DOI: 10.1051/0004-6361:20011324
- [31] E.C. Ostriker. *Capture and Induced Disk Accretion in Young Star Encounters*. *The Astrophysical Journal* 424:292-318, March 1994. DOI: 10.1086/173890
- [32] ‘Oumuamua ISSI Team. *The Natural History of ‘Oumuamua*. *Earth and Planetary Astrophysics* (astro-ph.EP), July 2019. DOI: 10.1038/s41550-019-0816-x
- [33] O.R.Pols *Stellar Structure and Evolution*. <http://www.ucolick.org/~woosley/ay112-14/texts/pols11.pdf>, Sept 2011.
- [34] W.H. Press, S.A. Teukolsky , W.T. Vetterling & B.P. Flannery. *Numerical Recipes: The Art of Scientific Computing*. Integration of Ordinary Differential Equations. Third Edition, 2007.
- [35] A. Rao, P. Gandhi, C. Knigge; J.A. Paice, N.W.C. Leigh and D.Boubert. *Kinematic study of the association Cyg OB3 with Gaia DR2*. *MNRAS* 000, 1-14 (2018), August 2019. DOI: 10.1093/mnras/staa1217
- [36] S.N. Raymond, P.J. Armitage, and N. Gorenstein. *Planet-Planet Scattering in Planetesimal Disks*. *The Astrophysical Journal*, 699:L88–L92, July 2009. DOI: 10.1088/0004-637X/699/2/L88
- [37] A. Scally, C. Clarke *Destruction of protoplanetary disks in the Orion Nebula Cluster*. *Astrophysics* (astro-ph), Dec 2000. DOI: 10.1046/j.1365-8711.2001.04274.x
- [38] J.Schombert *Astronomy 122: Birth and Death of Stars*. <http://abyss.uoregon.edu/~js/ast122/>, Accessed: July 2020.

- [39] I.Thies, P. Kroupa, C. Theis. *Induced planet formation in stellar clusters - a parameter study of star-disk encounters.* Mon.Not.Roy.Astron.Soc.364:961-970,2005, Sept 2005. DOI: 10.1111/j.1365-2966.2005.09644.x
- [40] E. Vazquez-Semadeni, A. Palau, J. Ballesteros-Paredes G.C. Gomez, and M. Zamora-Aviles. *Global Hierarchical Collapse In Molecular Clouds. Towards a Comprehensive Scenario.* MNRAS 000, 1–36 (0000), March 2019. DOI: 10.1093/mnras/stz2736
- [41] D. Veras. *Private communication.* 2020
- [42] K. Vincke & S. Pfalzner. *Cluster Dynamics Largely Shapes Protoplanetary Disk Sizes.* The Astrophysical Journal, 828:48 (10pp), September 2016 . DOI :10.3847/0004-637X/828/1/48
- [43] J.P. Williams, L.A. Cieza *Protoplanetary Disks and their Evolution* Astrophysics of Galaxies (astro-ph.GA), March 2011. DOI: 10.1146/annurev-astro-081710-102548
- [44] S.P. Zwart, J. Makino , S.L W. McMillan , P. Hut *Star cluster ecology III: Runaway collisions in young compact star clusters.* Astrophysics (astro-ph), Dec 1998.